Design of an Optimized Acoustic Array for Aero-acoustic Research in an Open-jet Anechoic Wind Tunnel

MSc Thesis

S. Luesutthiviboon

Faculty of Aerospace Engineering
Department of Control and Operations
Section Aircraft Noise and Climate Effects

TU Delft

Design of an Optimized Acoustic Array for Aero-acoustic Research in an Open-jet Anechoic Wind Tunnel

MSc Thesis

by

S. Luesutthiviboon

to obtain the degree of Master of Science
at the Delft University of Technology,
to be defended publicly on Wednesday November 22nd, 2017 at 12:30 PM.

Student number:	4520734	
Project duration:	February 6th, 2017 – November 22nd, 2017	
Thesis committee:	Prof.dr. D.G. Simons,	TU Delft, C&O, ANCE, Committee chair
	Dr.ir. M. Snellen,	TU Delft, C&O, ANCE, Supervisor
	Ir. J.A. Melkert	TU Delft, FPP, MSc track examiner

An electronic version of this thesis is available at `http://repository.tudelft.nl/`.

TU Delft

Preface

This thesis project is a part of obtaining my MSc degree in Aerospace Engineering at the Faculty of Aerospace Engineering, Delft University of Technology. This project has been carried out in the Aircraft Noise and Climate Effects (ANCE) section in the Control and Operations (C&O) department.

Although I am originally from the Flight Performance and Propulsion (FPP) department, I was given the opportunity to perform this thesis project by Dr.ir. Mirjam Snellen, who is also my thesis supervisor and Prof.dr. Dick G. Simons as the graduation professor. I feel very grateful for this opportunity and the motivation they have given to me throughout the project including their guidances to report and present my work in a clear and concise way. Moreover, I would like to thank Dr.ir. Pieter Sijtsma, who is a very experienced supervisor and has given me a lot of useful feedback and Ir. Anwar Malgoezar who has been a very open, supportive, and helpful supervisor.

This thesis project also involves an experimental part in the V-tunnel of TU Delft. This would have been a struggle without the well-designed hardware and data acquisition systems developed by my fellow student, Christian. I also would like to thank the remaining PhD candidates in the ANCE group, Roberto, Ana, and Alejandro, including all scientific and technical staffs involving in the V-tunnel who have participated and assisted me in the experiments.

Finally, I feel very thankful for love, supports, and encouragements from my family and friends. Without them, my journey throughout the past two years would have been impossible.

S. Luesutthiviboon
Delft, November 2017

Executive Summary

The objective of this thesis is to design an optimal acoustic array for TU-Delft's 'V-tunnel' which is an open-jet anechoic wind tunnel to be used in aero-acoustic studies. The acoustic array's beamforming performance is driven by two parameters; namely, the Maximum Side lobe Level (MSL) and Main Lobe Width (MLW) which can be derived from a source map it produces. These parameters were found to be linked with the array's geometry; the array's aperture, the nearest neighbor microphone distance, and the array's redundancy. However, aiming for low MSL and MLW will lead to opposite array geometries. Therefore, the array design optimization problem has been formulated to come up with a design which gives a good trade-off between these two qualities. In this thesis project, an optimization framework has been proposed. The optimization routine consists of two optimization loops; the main and the nested loop. The main loop consists of four design variables which are used to collectively describe the array's geometry without specifications of any individual microphone location. The design variables describe the distribution of microphones density wrt. the array's radial distance and the microphone's nearest neighbor microphone distance as a function of its radial distance on the array. The nested optimization loop attempts to generate microphone arrays which satisfy the geometry descriptions given from the main loop. Then the main loop searches for the optimal combination of geometry descriptions. It has been found that the optimal arrays from one optimization case, with side lobes weighted according to their distances from the main lobe, can achieve a lower MLW than the benchmarking Underbrink array and are able to produce a source map with side lobes lower than -15 dB up to the distance of approximately four times the MLW around the main lobe. These performance characteristics have been proven to hold for the cases with multiple and line sound sources, according to beamforming simulations. The experimental validation was performed in the V-tunnel, where the optimized array was tested in the real operating condition together with the benchmarking Underbrink array and an array generated by a random selection of geometry descriptors. The results validated the performance of the optimized array, verified the optimization method, and verified the results from the beamforming simulation used in the optimization. Further investigations have led to a guideline for experimental data processing when the array is used to measure sound sources subjected to air flow. It has been found that, within the operating flow speed of the V-tunnel, deterioration of the source map's quality can hardly be seen and a simple shifting correction derived from the known flow speed can be imposed in the conventional beamforming process to obtain an accurate sound source localization.

Contents

List of Figures

List of Tables

Nomenclature

Acronyms

B&K	Brüel & Kjær
CDF	Cumulative Distribution Function
CSM	Cross Spectral Matrix
CWA	Conventional Weighted Aggregation
DE	Differential Evolution
DPD	Differential Path Distance
GA	Genetic Algorithm
GPS	Generalized Pattern Search
HJ	Hooke-Jeeves
HVAC	Heating Ventilation and Air Conditioning
LB	Lower Bound
MLW	Main Lobe Width
MPSR	Main lobe Peak to Side lobe Ratio
MSL	Maximum Side lobe Level
PDF	Probability Distribution Function
PSF	Point Spread Function
PSO	Particle Swarm Optimization
SNR	Signal to Noise Ratio
SPL	Sound Pressure Level
UB	Upper Bound

Greek Symbols

α, β	Coefficients in the Conventional Weighted Aggregation (CWA) objective function definition
Δt	Time delay
Δ	Mesh size factor
δ	Array dispersion as defined by Yu and Donohue (2012)
Δ_{mn}	Differential Path Distance (DPD) of microphones pair m and n as defined by Yu and Donohue (2012)
ϵ_x, ϵ_y	Parameters for defining the spiral's shape of the Arcondoulis spiral array
γ	Ratio of number of unique vector spacings of the array over the maximum possible number of unique vector spacings
λ	Sound wavelength
μ	Mean in the truncated normal distribution
ν	Spiral angle of the Underbrink array
Ω	Feasible design space

ϕ_n, $\phi_{m,n}$	Angular position on the array of a microphone
$\Phi_{\max}$	Maximum spiral angle of the Arcondoulis spiral array
$\psi(x)$, $\chi(x)$	Associating functions for defining the Probability Distribution Function (PDF) and the Cumulative Distribution Function (CDF) of the truncated normal distribution
σ	Standard deviation in the truncated normal distribution
τ	Objective function tolerance
θ	Steering angle of a line array
Θ, $\Theta_{\min}$	Angular location on the scan plane relative to a point source in the scan plane's center measured from the center of the acoustic array, minimum value of Θ where two sources are still resolvable by beamforming, i.e. when the sources are separated by the distance equals to the Rayleigh limit
φ_i	Rotation angle of the i^{th} circle in the concentric array definition
$\vec{\xi}$	Vector pointing from the reference point to a grid point on the scan plane

Roman Symbols

D	Search pattern matrix
d	Descendants
I	Identity matrix
M	Set of mesh point
p	Partner population
S	Cross Spectral Matrix (CSM)
u	Design vector in the nested optimization loop
X	Design vector in the main optimization loop
x, y	X and Y coordinates on the array of a microphone
$\vec{g}$	Vector off all g
$\vec{P}$	Vector of all P_n
$\vec{x}$	Vector pointing from the reference point to a microphone
$\vec{x}_0$	Array's centroid
$\vec{X}_p$	Set of all vector spacings
A	Source autopower
a, b	Parameters for defining the Arcondoulis spiral array
c	Speed of sound
D	Array's effective diameter
d	Distance between an arbitrary point on the scan plane and an arbitrary microphone on the acoustic array
$D(\theta)$	Directionailty of a line array
d_{nn}, d_{nn,r_n}	Nearest neighbor inter-microphone distance (of the n^{th} microphone at the distance r_n)
F	Crossover fraction
f	Frequency
f_H	Microphone distribution function defined by Sarradj (2016)
f_k, $f_{k,\min}$, $f_{k,\max}$	Beamforming frequency (minimum, maximum)

$f_r(r)$, $F_r(r)$	Probability Distribution Function (PDF) and Cumulative Distribution Function (CDF) of the truncated normal distribution
g	Steering vector from a grid point on the scan plane to a microphone on the array
H	Array definition parameter from Sarradj (2016)
h	Distance from the array to the scan plane
i	Complex number
I_0	Modified 0^{th} order Bessel function
j	Index of grid points on the scan plane
J, J_{MSL}, J_{MLW}	Generic objective functions (representing the Maximum Side lobe Level (MSL) and the Main Lobe Width (MLW))
J_1	Bessel function of the first kind
J_{main}, J_{nested}	Objective functions of the main and nested optimization loop
M	Mach number
m	Mesh size scaling factor
N	Number of all microphones on the array
N_a, N_m	Number of spiral arms and microphone per spiral arm in the Underbrink array, respectively
N_G	Maximum number of generation
N_P	Population size
N_{r_b}	Number of microphones in the b^{th} statistical bin centered at the distance r_b on the array
nn_{min}, nn_{max}	Minimum and maximum nearest inter microphone distance (d_{nn})
P, P_{max}	Number (and maximum number) of unique vector spacings of the array
p_0	Reference Sound Pressure Level
p_B	Beam spectrum
p_c	Crossover probability
P_n	Fourier transform of sound signal received by the n^{th} microphone
p_n	Sound signal received by the n^{th} microphone
r	Distance from a microphone on the array to a grid point on the scan plane
R_0, R_{max}	Minimum and maximum microphone radial distance on the array except the center microphone
R_1	Reference distance in beamforming
r_b	Radial distance b^{th} statistical bin's center
r_i	Radius of the i^{th} circle in the concentric array definition
r_n, $r_{m,n}$	Radial distance on the array of a microphone
RL	Rayleigh limit
S	Element in the Cross Spectral Matrix (CSM, $\mathbf{S}$)
t	Dimensionless distance on a Bezier curve
U_∞	Flow speed
V	Array definition parameter from Sarradj (2016)
$W(\Theta)$	Analytical Point Spread Function (PSF) from beamforming by a finite-aperture circular array
w_f	Distance from the sound source to the shear layer
y_{sh}	Shift of the source's apparent Y coordinate

Superscripts

$'$	Actual array geometric feature evaluated in the nested optimization loop
$*$	Complex conjugate of a vector
i	Index of the design variable in the main optimization loop
j	Index of the design variable in the nested optimization loop

Subscripts

ref	Reference value
b	Index of the statistical bins dividing the array's radial distance
c	Column number in the search pattern matrix (**D**)
j	Index of a grid point on the scan plane
l	Generation number
n, m	Index of microphones on the array
nn	Subscript representing nearest neighbor microphone distance
nr	Subscript representing number of microphone per radial distance
p	Individual index in the population
q	Iteration number

1 Introduction

1.1. Acoustic Arrays and their Usages

Acoustic arrays or *acoustic cameras* are arrays of multiple microphones arranged in certain configurations to acquire acoustic data. The recorded signals can be post-processed by performing *beamforming*, utilizing the information of the different relative microphone positions with respect to the sources (Sarradj, 2016, Sarradj et al., 2006), to construct a so-called *source map* or *acoustic image*, which visualizes, quantifies, and localizes sources of sound in a region of interest.

The acoustic arrays and the processed source maps have been employed in various applications such as speech acquisition in cars (Ayllón et al., 2014), speech acquisition in robotics (Sasaki et al., 2011), and analysis of noise from moving trains (Le Courtois et al., 2016). In aerospace and aero-acoustic applications, these tools have also been employed in a number of different aspects. This ranges from the analysis of fly-over aircraft noise by placing a microphone array close to a runway (Merino-Martínez et al., 2016, Sijtsma and Stoker, 2004, Simons et al., 2015) to indoor applications, especially in wind tunnels, in which the acoustic array can either be embedded in the closed test section surface (Ehrenfried et al., 2006, Shin et al., 2007) or placed outside the flow in case of an open-jet wind tunnel (Hurault et al., 2015, Sijtsma et al., 2001). Examples of acoustic arrays and processed source maps in aero-acoustic applications are shown in Figure 1.1 and 1.2, respectively. The insights obtained from examining the source maps can help researchers understand the noise sources characteristics and utilize the knowledge to achieve improved designs with reduced noise radiation. For example, a wind turbine with lower trailing edge noise (Oerlemans et al., 2009) or noise reduction of airfoils (Geyer et al., 2010).

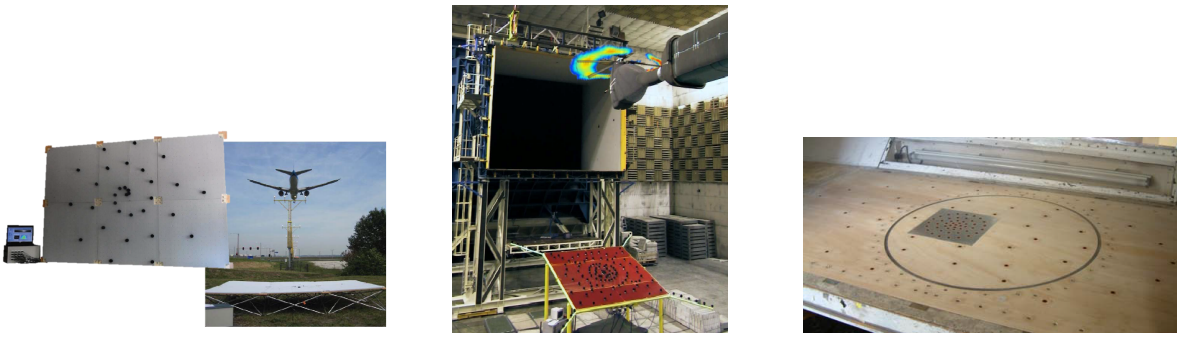

(a) (b) (c)

Figure 1.1: Various usages of acoustic arrays; (a) Acoustic array for measuring aircraft noise at operating conditions (source: Merino-Martínez et al. (2016)), (b) Acoustic array in an open-jet wind tunnel (source: Sijtsma et al. (2001)), and (c) Acoustic array in a closed-section wind tunnel (source: Shin et al. (2007))

An ideal source map should show clear and separable sources at the correct locations with the accurate magnitudes of the sound sources. Moreover, it should be free from false positives which could cause misinterpretations. Many attempts have been made in modifying the beamforming algorithm, i.e. the post-processing steps of the received signal, to obtain a clear and accurate source map (Brooks and Humphreys, 2006, Malgoezar

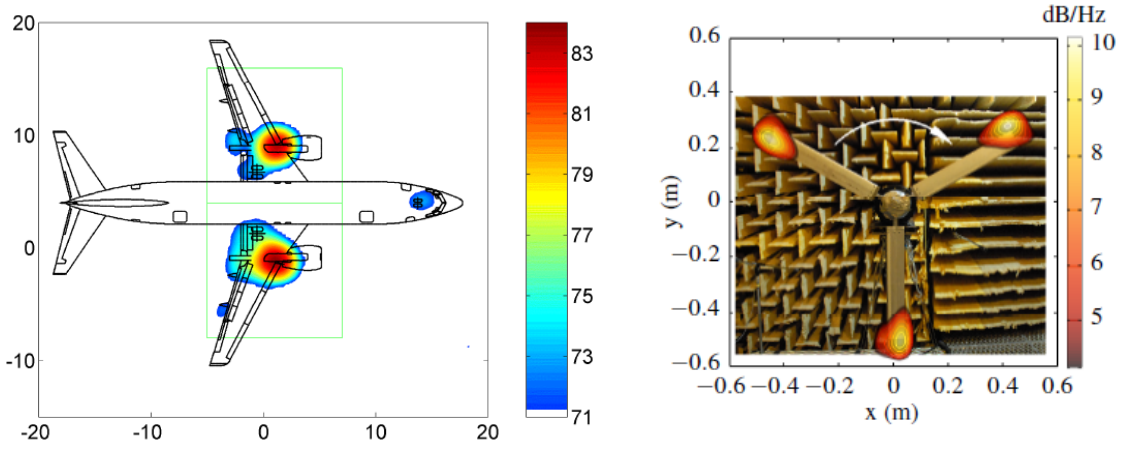

(a) (b)

Figure 1.2: Examples of acoustic source maps; (a) Source map of a B737-400 aircraft fly over processed at 2 kHz (source: Sijtsma and Stoker (2004)) and (b) Source map overlaid on a rotor rig in an anechoic chamber processed at 7.17 kHz (source: Prime et al. (2014))

et al., 2016b, Sijtsma, 2007). However, another way of ensuring a high quality source map is by strategically placing microphones on an array (Malgoezar et al., 2016a). Since there are several requirements for the source map which sometimes lead to different microphone array designs, an optimization process is required to find a proper design compromise and come up with an optimized array.

1.2. TU Delft's V-tunnel

The newly-constructed 'V-tunnel' facility of TU Delft shown in Figure 1.3 is an anechoic open-jet wind tunnel aimed for aero-acoustic studies. The jet flows vertically from a circular duct having a diameter of 0.6 m. The jet has low turbulence level and can achieve a speed of 40 m/s. A planar acoustic array holding 64 microphones is used in acquiring the sound signals from test objects in the wind tunnel. The array's dimension is 2×2 m and consists of small holes arranged in a square lattice manner, enabling various microphone arrangements with quick re-configuration.

Since the number of microphones is limited, they need to be strategically placed on the array to ensure the production of high-quality source maps. Since there are countless possible microphone arrangements on this array, the optimal microphone arrangement is to be found out of those possibilities.

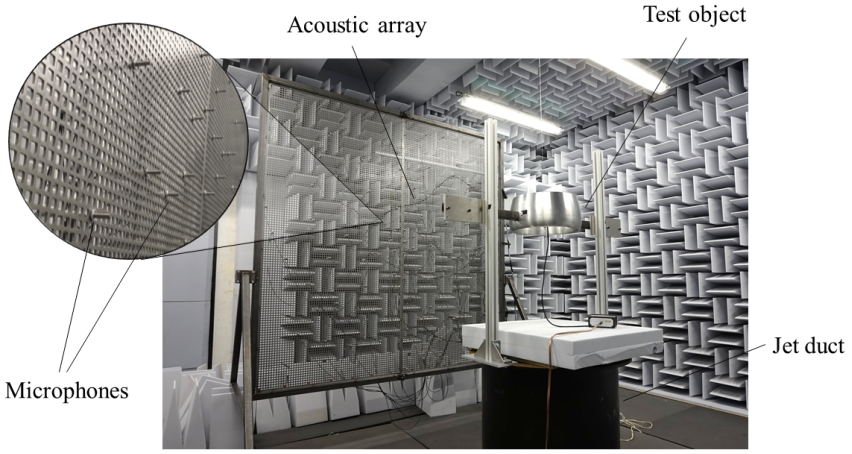

Figure 1.3: TU Delft's V-tunnel facility (photo: Anwar Malgoezar)

1.3. Objective and Structure of the Thesis Project

The objective of this thesis project has been stated as follows:

> The objective of this thesis is to develop an optimal microphone array for TU Delft's V-tunnel by optimizing the placement of microphones and performing experimental validation.

The rest of this thesis project report presents the steps taken, and their results, in order to achieve the stated thesis objective. Chapter 2 and 3 summarize the insights from the previous works on acoustic array design optimization. Chapter 2 focuses on the beamforming theory, the measures for beamforming performance, and summarizes the relationships of the acoustic array's geometry with its beamforming performance. Chapter 3 focuses on the optimization of the acoustic array, starting from the benchmark, the techniques for formulating the optimization problems, and then scopes down to the design considerations for wind tunnel acoustic arrays. After that, Chapter 4 utilizes the insights obtained from previous research works to come up with the proposed optimization methodology. In this chapter, the proposed optimization method is extensively discussed together with some preliminary investigations of the parameter design space. Having employed the proposed optimization methodology, Chapter 5 presents the optimization results. Further investigations of the optimized acoustic arrays are conducted to select the potential designs for experimental testings. Chapter 6 presents the experimental validation where the selected optimal acoustic array and the reference arrays are tested. Chapter 7 presents results from a case-study which employs the selected arrays close to the real aero-acoustic operating conditions. Finally, Chapter 8 summarizes this thesis project and provides recommendations for future works.

2

Beamforming Performance Relationship with Acoustic Array's Geometry

2.1. Theory of Beamforming

The translation of the sound signals acquired by an acoustic array into source maps is made possible by applying *beamforming*. Consider an acoustic array consisting of N microphones schematically shown in Figure 2.1. The known n^{th} microphone location is represented by a vector $\vec{x}_n$ pointing from a reference origin. It is assumed that the potential sound sources to be investigated lie on a plane at the distance h from the acoustic array. The *scan plane* can be defined and discretized by defining grid points. Let $\vec{\xi}_j$ be a vector pointing from the reference origin to the j^{th} grid point on this scan plane. Then $r_{j,n}$ can be defined as the distance from the j^{th} grid point to the n^{th} microphone as $r_{j,n} = \left\| \vec{x}_n - \vec{\xi}_j \right\|$.

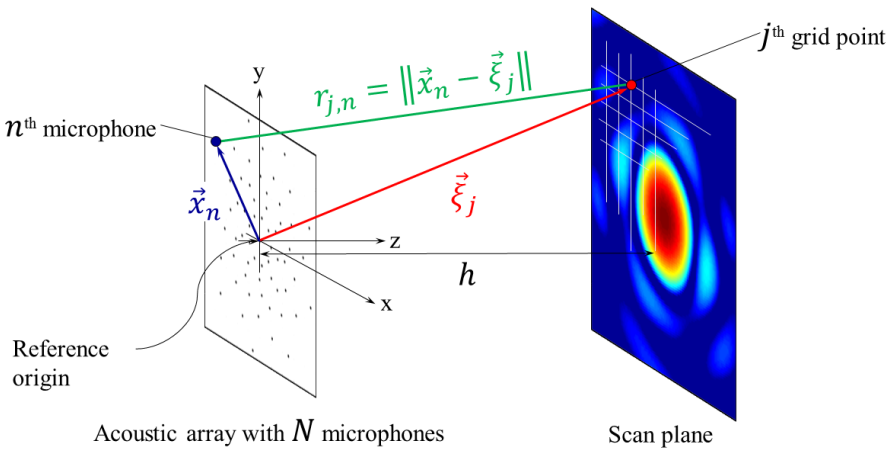

Figure 2.1: Schematic definitions of vectors and distances used in beamforming

Since the time required, or the *time delay* ($\Delta t_{j,n}$), for the sound pressure to travel from a certain grid point to different microphones is known and can be calculated by $\Delta t_{j,n} = r_{j,n}/c$, where c is the speed of sound, this information can be used to account for the time the signals travel to different microphones. Focusing on a certain grid point on the scan plane can be done by delaying the signals per microphone such that, constructive interference is obtained when there is a sound source present in that grid point and destructive or partial interferences for sound sources in other grid points. After summing up the signals from all microphones per grid point at all grid points and mapping the resulting levels, a source map that localizes the contributing sound sources on the

scan plane is constructed (Malgoezar et al., 2016a, Sarradj et al., 2006). According to its working principle, this method is called the *delay-and-sum beamforming* or *conventional beamforming*.

The conventional beamformer is usually applied at a predefined k^{th} frequency (f_k). Let $p_n(t)$ be the sound pressure signal received by the n^{th} microphone. The information in the frequency domain of the signal can be obtained by applying the Fourier transform. Let P_n be the received sound signal after applying the Fourier transform to p_n. After that, $P_n(f_k)$ can be taken out from the signal's spectrum. The vector $\vec{P}(f_k)$, containing all $P_n(f_k)$ can be written as

$$\vec{P}(f_k) = \begin{bmatrix} P_1(f_k) & P_2(f_k) & \dots & P_N(f_k) \end{bmatrix}^T. \tag{2.1}$$

The *Cross Spectral Matrix* (CSM), denoted by $\mathbf{S}$, can be constructed by multiplying the vector $\vec{P}(f_k)$ with its complex conjugate, $\vec{P}(f_k)^*$, as

$$\mathbf{S} = \frac{1}{2}\vec{P}(f_k)\vec{P}(f_k)^*. \tag{2.2}$$

For a long time domain signal, sometimes the signal in time domain is divided in small segments. The Fourier transform is applied to each data segment. Then the vector $\vec{P}(f_k)$ is obtained and the CSM is determined per each segment as in Equation 2.2. After that, all obtained CSMs are averaged.

For beamforming, the *steering vector* from the j^{th} grid point to the microphones is calculated by

$$\vec{g}_j = \begin{bmatrix} g_{j,1} & g_{j,2} & \dots & g_{j,N} \end{bmatrix}^T, \tag{2.3}$$

where the component of $\vec{g}_j$ associating with the n^{th} microphone is

$$g_{j,n} = \frac{-e^{-2\pi i f_k \Delta t_{j,n}}}{4\pi r_{j,n}}. \tag{2.4}$$

The steering vector represents the modelled signals as received on the microphones. By minimizing the difference between the measured CSM and that modelled through the steering vector, an estimated source strength is obtained per grid point. The source autopower (A_j) at the j^{th} point on the scan plane can be calculated from

$$A_j = \frac{\vec{g}_j^* \vec{P}(f_k)\vec{P}(f_k)^* \vec{g}_j}{\left\|\vec{g}_j\right\|^4} = \frac{\vec{g}_j^* \mathbf{S} \vec{g}_j}{\left\|\vec{g}_j\right\|^4}. \tag{2.5}$$

Finally, the output of the beamforming is usually presented as the Sound Pressure Level (SPL) at the reference distance R_1 from the j^{th} point on the scan plane and can be obtained from

$$\text{SPL}_j = 20\log_{10}\left(\frac{\sqrt{A_j}}{4\pi R_1 p_0}\right), \tag{2.6}$$

where $p_0 = 2 \times 10^{-5}$ Pa is the reference pressure. By repeating the steps from Equation 2.3 to 2.6 for all grid points, the source map can be produced.

As mentioned earlier, the beamforming method presented above is the conventional, delay-and-sum, beamforming method. Apart from that, there exist a number of beamforming techniques that attempt to improve the source maps' quality such as the CLEAN methods (Sijtsma, 2007) or the DAMAS method (Brooks and Humphreys, 2006), and that usually require iterative calculations (Arcondoulis et al., 2010). Some other methods also require global optimization (Malgoezar et al., 2016b). These advanced beamforming methods are suitable for additional post-processing the sound signal.

2.2. Measuring the Acoustic Array's Beamforming Performance

The performance of an acoustic array can be judged by analyzing the quality of the source maps it produces. The quality of the source map is commonly quantified by two parameters; namely, the Main Lobe Width (MLW) and the Maximum Side lobe Level (MSL).

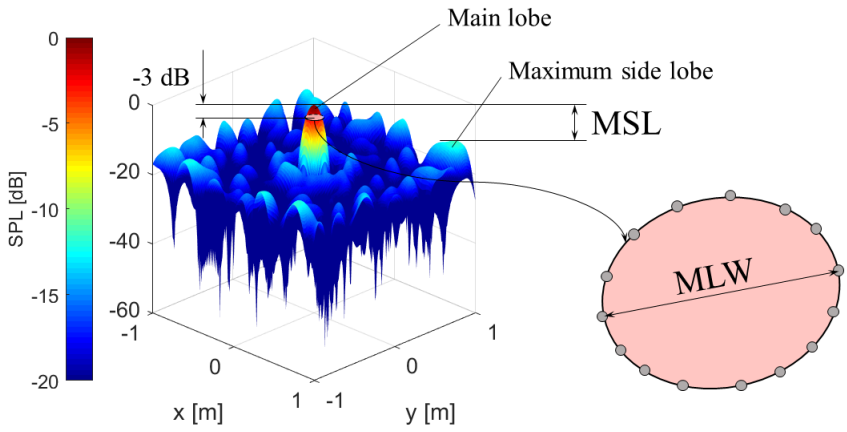

Figure 2.2: Definitions of MSL and MLW

2.2.1. Main Lobe Width (MLW)

The *main lobe* in the acoustic source map represents the magnitude and location of the true sound source in the scan plane. The MLW is defined as the maximum distance between two points in the extracted set of points representing the main lobe contour at -3 dB from the main lobe's peak[1] as shown in Figure 2.2. MLW provides information on spatial resolution of the acoustic array as the narrower the main lobe is, the more likely that closely located but different sources can be distinguished.

However, there exists a distance limit where the sound sources which are closer than that distance are no longer resolvable as separated sources by a finite aperture array. This limit is called the *Rayleigh limit/ Rayleigh criterion*. The derivation of this limit together with its relationship with the MLW are shown in Section 2.3.

2.2.2. Maximum Side lobe Level (MSL)

As a result of constructive interference, beamforming can produce regions having high magnitude of sound although there is no sound source present (Malgoezar et al., 2016a). These peaks in the source map are called *side lobes* when the constructive interference is partial and the magnitude of the peak is not as high as the main lobe, or *grating lobes* when the constructive interference is full and the magnitude of the peak is as high as the main lobe. The value of MSL can be calculated my measuring the relative magnitudes of the main lobe to the maximum side lobe in the acoustic image (Le Courtois et al., 2016) as shown in Figure 2.2. There exist slightly different ways of defining MSL such as the Mainlobe Peak to Side lobe Ratio (MPSR) (Yu and Donohue, 2012) or Signal to Noise Ratio (SNR). (Ayllón et al., 2014, Sarradj et al., 2006, Yu and Donohue, 2013, Yu et al., 2013). However, they all present a similar concept. The MSL tells how close the magnitude of the highest side lobe is to the main lobe and implies how likely it is to be misinterpreted as a true sound source in the source map.

2.3. Beamforming Performance of Finite-aperture Circular Arrays

Supposing that there exists one point source at a certain distance normal to the center of a circular array having the finite diameter of D, this point source cannot perfectly be resolved as a point in the source map, but rather a lobe, i.e. main lobe, having the dimension together with a series of side lobes. This phenomenon is analogous to the ability of a circular lens in resolving a point light source in optics where the diffraction of light causes the extension of the source's boundary and a pattern of lower light intersity around it (Malgoezar et al., 2016a). This pattern is called the Point Spread Function (PSF). The analytical PSF resolved by a finite-aperture circular

[1]Instead of extracting the area of the main lobe's cross section at -3 dB as in Le Courtois et al. (2016), the maximum distance between two points in the point cloud is used instead as it has been found that a distorted main lobe shape can also have a small cross-section area and this can mislead the optimization. In contrast, a distorted main lobe will have a high maximum distance between two points in the point cloud and will be reflected as having a bad MLW performance in the optimization. It is also worth noting that the accuracy of the MLW value depends on the discretization resolution of the scan plane.

acoustic array having an infinite number of microphones at the beamforming frequency f_k can be written as (Sarradj, 2016)

$$W(\Theta) = 2\frac{J_1(\frac{\pi f_k D}{c}\sin\Theta)}{\frac{\pi f_k D}{c}\sin\Theta}, \tag{2.7}$$

where J_1 is the Bessel function of the first kind. The value of Θ determines the location on the scan plane and can be written as $\Theta = \cos^{-1}(\frac{h}{\|\vec{\xi}_j\|})$, according to Figure 2.1. The SPL at any spatial point j on the scan plane can then be calculated from (Sarradj, 2016)

$$\mathrm{SPL}_j = 10\log_{10}|W(\Theta)|^2. \tag{2.8}$$

A source map produced by employing Equations 2.7 and 2.8 using an array having the diameter (D) of 1.9 m, containing an infinite number of microphones, and the beamforming frequency (f_k) of 4 kHz is shown in Figure 2.3a. The dash line shows the cut plane where the SPL in that plane is shown in Figures 2.3b and 2.3c. The SPL produced by the same method using different values of D and f_k are shown together in these Figures. The dash lines indicate the SPL of -3 dB where the MLW is evaluated. It can be seen that the MLW reduces as the array's diameter (D) or the beamforming frequency (f_k) increase. However, for all cases, the MSL does not change and remains at -17.6 dB. This indicates the theoretically minimum attainable MSL.

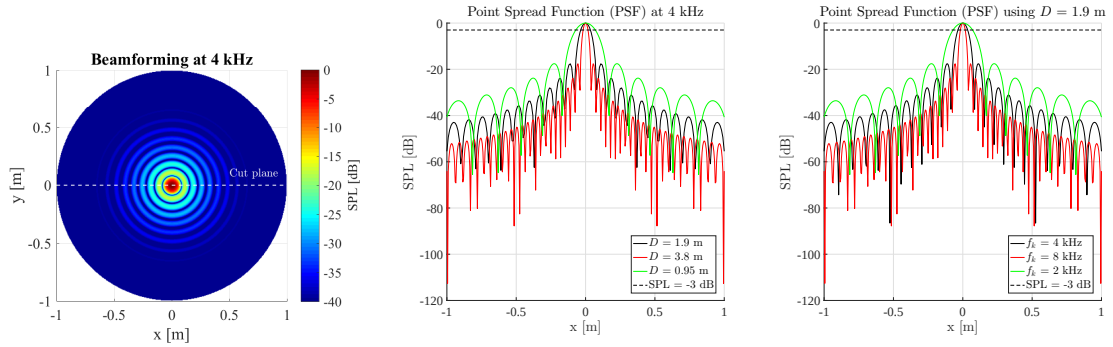

(a) (b) (c)

Figure 2.3: PSF produced by a circular array with an infinite number of microphone; (a) D = 1.9 m, f_k = 4 kHz, (b) f_k = 4 kHz, with varying D, (c) D = 1.9 m, with varying f_k

In reality, it is only possible to have an acoustic array with a finite number of microphones. The SPL from source maps produced by acoustic arrays with different number of microphones regularly placed in a circular as in Figure 2.4 area are shown in Figure 2.5. It can be seen that the SPL patterns deviate from that from the array with an infinite number of microphone as the number of microphones decreases. This can also be indicated by the deterioration of the array's performance in terms of MSL and MLW.

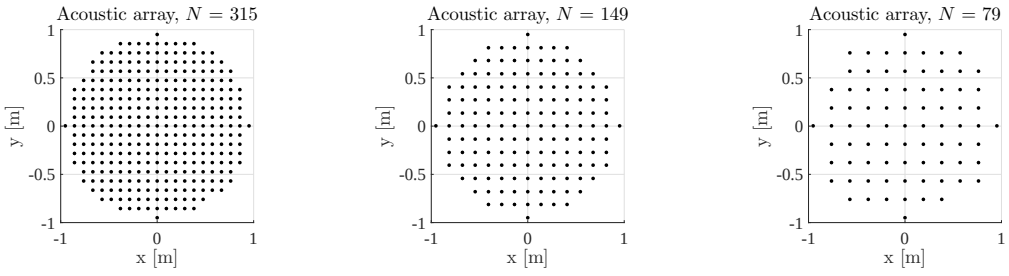

(a) (b) (c)

Figure 2.4: Acoustic arrays with various number of microphones placed regularly in a circular area

When there are multiple point sources on the scan plane, each point source will produce its individual PSF pattern. When one point source is placed closer than the first zero crossing of the PSF of another point source, these two sources are no longer resolvable as two separate sources by a finite-aperture array. This distance is the

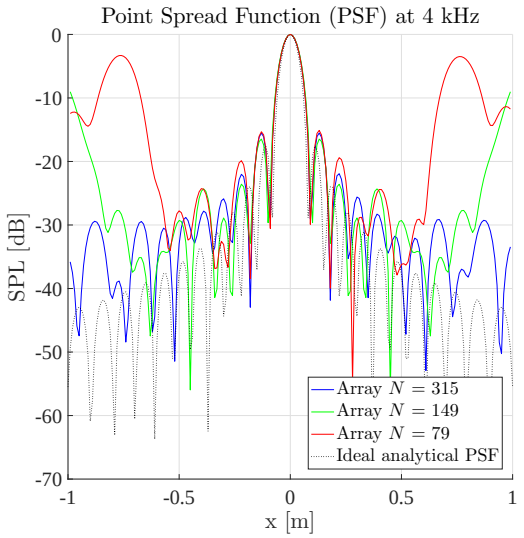

Figure 2.5: PSF produced by acoustic arrays in Figure 2.4

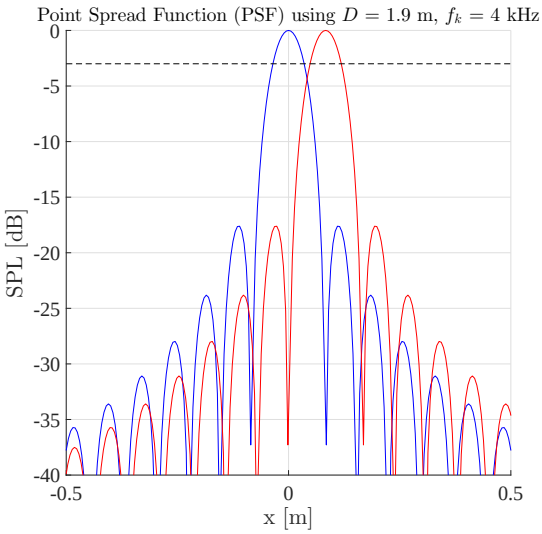

Figure 2.6: Two PSFs placed at the Rayleigh limit of each other

so-called *Rayleigh limit* introduced in Section 2.2.1. Having introduced the PSF in Equations 2.7 and 2.8, the expression for the Rayleigh limit can be derived as follows.

The first zero crossing of Equation 2.7 will occur when the numerator or the Bessel function of the first kind equals to zero, i.e. $J_1(u) = 0$. According to the property of the Bessel function, the first zero crossing happens when $u \approx 3.83$. Let Θ_{min} denote the minimum angle where two sources are still resolvable, $\Theta_{\text{min}} = \tan^{-1}\frac{RL}{h}$, where RL is the Rayleigh limit. From Equation 2.7, this limit can be written in terms of f_k and D as

$$\frac{\pi f_k D}{c} \sin\Theta_{\text{min}} = 3.83. \tag{2.9}$$

Using small angle approximation, we have

$$\Theta_{\text{min}} = 1.22\frac{c}{f_k D}. \tag{2.10}$$

This can be written in terms of RL and h as

$$RL = h\tan\left(1.22\frac{c}{f_k D}\right) \tag{2.11}$$

When the term J_1 in Equation 2.7 is zero, Equation 2.8 will give $\text{SPL}_j \to -\infty$, since $\log(x) \to -\infty$ when $x \to 0$. This indicates that the actual boundary of the main lobe is at $\text{SPL} \to -\infty$. Practically, the MLW cannot be measured at that SPL. Therefore, the MLW is measured at SPL = −3 dB instead, as shown previously. It can be seen that the MLW defined close to the peak using this convention is always smaller than the actual width of the main lobe. This can make it somewhat more complicated to relate the MLW with the Rayleigh limit RL. To understand this, two PSFs produced by Equations 2.7 and 2.8 using $D = 1.9$ m and $f_k = 4$ kHz are plotted together in Figure 2.6. The peaks of these PSF are separated by the distance equal to the Rayleigh limit, i.e. right above the point where the SPL of the other PSF is reaching $-\infty$. If we used the actual MLW measured at $-\infty$, we could say that the Rayleigh limit is half of the MLW. However, the MLW is measured at SPL = -3 dB indicated by the dashed line which is smaller. Because of this, there exists a gap between the main lobes at this level and it is possible that the MLW is smaller than the Rayleigh limit.

The presence of side- and/or grating lobes together with the MLW are affected by the microphone positions on the acoustic array as the microphone locations also contribute in the beamforming equations. Therefore, the relationship between the microphone placement and the array's performance have to be derived from the beamforming equations or from source maps obtained from simulations. The knowledge obtained so far is summarized in Section 2.4.

2.4. Influences of Acoustic Array's Geometry on Beamforming Performance

Within the literature study, detailed insights on the relationship between the beamforming performance and some geometric features of an array were obtained. Three main aspects were found in literature; the array redundancy parameter, the array aperture or dispersion from its centroid, and the inter microphone distance. Findings from these studies can be very useful as a primany knowledge for array design and will be discussed in this section.

2.4.1. Array's Redundancy

Consider the numerator of Equation 2.5, and defining this part as *beam spectrum* (p_B) (Havelock et al., 2008). Under the plane wave assumption, this can be re-written as

$$p_B = \vec{g}_j^* \mathbf{S} \vec{g}_j = \sum_{n=1}^{N} \sum_{m=1}^{N} S_{nm}(f_k) e^{\frac{2\pi i f_k (\vec{x}_m - \vec{x}_n)}{c}}. \tag{2.12}$$

It can be realized that the cross-correlation calculation is done as a function of all microphone pairs located at $\vec{x}_m$ and $\vec{x}_n$, and is directly dependent on the way microphones are arranged on the array (Havelock et al., 2008), which contributes to the occurrence of side lobes and grating lobes. The term *redundancy* of an array refers to the redundancy in the cross-correlation of the microphone locations involved in Equation 2.12, which is a part of the beamforming calculation.

This knowledge has been utilized in array design and a parameter that indicates the array's redundancy based on the aforementioned knowledge or the so-called *co-array* (*vector spacing*) was first defined by Haubrich (1968) in the seismological applications. The co-array can be used to investigate the irregularity redundancy in sensor position. It should be ensured that all sensors are placed with minimal redundancy to avoid spatial aliasing (Prime and Doolan, 2013, Underbrink, 2002).

Let $\vec{X}_p$ be the so-called co-array of an array with N microphones, $\vec{X}_p$ is a set of all possible vector spacings in this array as

$$\vec{X}_p = \vec{x}_m - \vec{x}_n, \tag{2.13}$$

where $m = 1, 2, \ldots, N$ and $n = 1, 2, \ldots, N$. Since the elements in $\vec{X}_p$ are the products of vector subtraction, for any given pair of microphones, two elements in $\vec{X}_p$ can be produced, i.e. $\vec{x}_m - \vec{x}_n$ and $\vec{x}_n - \vec{x}_m$. Therefore, there are N^2 elements in $\vec{X}_p$. However, N elements in $\vec{X}_p$ are vectors of zeros produced when $m = n$. Thus, the maximum number of unique vector spacings in the co-array is $P_{\max} = N^2 - (N-1)$ (all possible non-zero vectors minus all zeros and plus one zero). Let the actual number of unique vector spacings in the array be $P \leq P_{\max}$, the redundancy of the array can be defined as

$$\gamma = \frac{P}{P_{\max}} = \frac{P}{N^2 - (N-1)} \leq 1. \tag{2.14}$$

One simple way of designing a low-redundancy array is by arranging microphones in a circular manner with an odd number of microphones per circle (Dudgeon and Johnson, 1993). Examples are shown in Figure 2.7 and Figure 2.8. Both arrays consist of 64 microphones. The array in Figure 2.7 has an even number of microphones per circle while that of array in Figure 2.8 has an odd number. The co-arrays, which are the points defined by the vectors in $\vec{X}_p$, of both arrays are shown on the right hand side and it is noticeable that the co-array of the array in Figure 2.8 is covering more white space, implying its higher number of unique vector spacings. The value of γ for both arrays are calculated using Equation 2.14 also shown above the co-arrays and γ of the odd-numbered array is higher than the even-numbered array, confirming the low redundancy.

Similar concepts have been implemented by Yu and Donohue (2012). Consider a scan plane where a true sound source is located at $\vec{\xi}_s$, for any scan points $\vec{\xi}_j$ where $\vec{\xi}_j \neq \vec{\xi}_s$, the magnitude of sound determined by the beamforming should be minimized, i.e. no side lobes, while it should be maximum when $\vec{\xi}_j = \vec{\xi}_s$ as a result of coherent addition (Yu and Donohue, 2015). For any scan points j and source locations s, the *Differential Path Distance* (DPD), of microphones m and n can be defined as

$$\Delta_{mn}(\vec{\xi}_j, \vec{\xi}_s) = (d_{sn} - d_{sm}) + (d_{jm} - d_{jn}), \tag{2.15}$$

where d represents the distance from the point j or s to microphone m or n, according to the subscripts. In order to minimize the interference in beamforming, it has been proposed that the microphones on the array should be arranged such that the values of $\Delta_{mn}(\vec{\xi}_j, \vec{\xi}_s)$ cover as wide as possible range and distribute as evenly as possible.

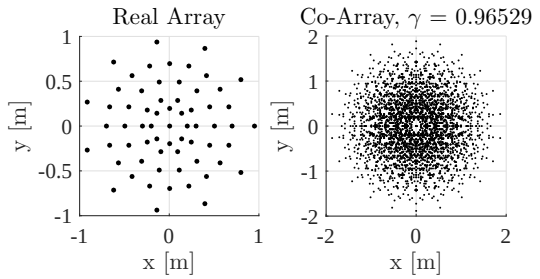

Figure 2.7: Even-numbered array (left) and co-array (right)

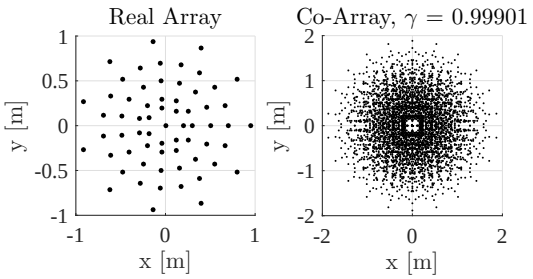

Figure 2.8: Odd-numbered array (left) and co-array (right)

This knowledge of array redundancy and concentric arrays with odd number of microphones per circle has been employed in the synthesis of several well-known benchmarking arrays, which will be discussed in detail in Section 3.1.

2.4.2. Microphone Distribution Density wrt. Array's Radial Distance

By observing microphone arrangements after optimization and investigating the resulting array's performance, it has been commonly proven that the microphone distance from the array's centroid has a strong correlation with the array's performance in terms of MSL and MLW. Arrays with more microphones clustered around the centroid are more likely to have better side lobe suppression (low MSL) while arrays with microphone placed close to the edge are more likely to achieve a narrower main lobe (low MLW) (Babale et al., 2014, Jin and Rahmat-Samii, 2007, Le Courtois et al., 2016, Prime and Doolan, 2013) as a result of having a higher effective array diameter (D). Two arbitrary arrays that have the same diameter can have different performance based on how microphones inside are arranged. Schulze et al. (2004) investigated two circular arrays with identical diameter containing 32 microphones. One array consisted of only one circle while the other has a smaller circular array inside and fewer microphones on the outer circle. It was found that the first array provided lower MLW while the second provided lower MSL. However, due to the even number of microphones, the first array also suffered from high side lobes due to its redundancy as discussed in Section 2.4.1.

Since it is desirable to have both low MSL and MLW and these requirements lead to opposite designs, this becomes an interesting trade-off to make in the array design optimization problem.

Several attempts have been made to quantify and geometrically describe this microphone distribution and correlate it directly to the array's performance. Yu and Donohue (2012) proposed *array dispersion* (δ) which describes the average distance of microphones from the array's centroid as

$$\delta = \sqrt{\frac{1}{N}\sum_{n=1}^{N}\Big[(x_n - x_0)^2 + (y_n - y_0)^2 + (z_n - z_0)^2\Big]}, \tag{2.16}$$

where $\vec{x}_0 = [x_0, y_0, z_0]^T$ is the array's centroid and $\vec{x}_n = [x_n, y_n, z_n]^T$ is the location of the n^{th} microphone. Dependencies of the MSL and MLW on the proposed geometry descriptor was found. The MSL is low when δ is low while the MLW is low when δ is high. Apart from that, Sarradj (2015) and Sarradj (2016) proposed a generic way of defining all microphone locations on the array with a nature-inspired method that attempts to describe the sunflower seeds arrangement with a mathematical formula. The radial and the angular positions of the n^{th} microphones are defined as

$$r_n = R_{\max}\sqrt{\sum_{i=1}^{n}\frac{\int_0^{R_{\max}} f_H(H,r)dr}{N f_H(H,r_i)}} \tag{2.17}$$

and

$$\phi_n = 2\pi n\frac{1+\sqrt{V}}{2}, \tag{2.18}$$

respectively, where

$$f_H(H,r) = \begin{cases} I_0(\pi H\sqrt{1-(r/R_{\max})^2}), & H \geq 0 \\ 1/\big[I_0(\pi H\sqrt{1-(r/R_{\max})^2})\big], & H < 0 \end{cases}, \tag{2.19}$$

$R_{\max}$ is the maximum radius of the array, and I_0 is the modified 0^{th} order Bessel function. By fixing V to 5 and adjusting the value of H in the expressions, the microphones density with respect to the radial distance can be controlled as shown in Figure 2.9, the microphones are densely placed close to the array's center when H is high and close to the array's edge when H is low. It is shown on the plot in Figure 2.10 that H can determine the resulting MSL and MLW of the array. The array will produce low MSL and high MLW when the value of H is high and vice versa when the value of H is low.

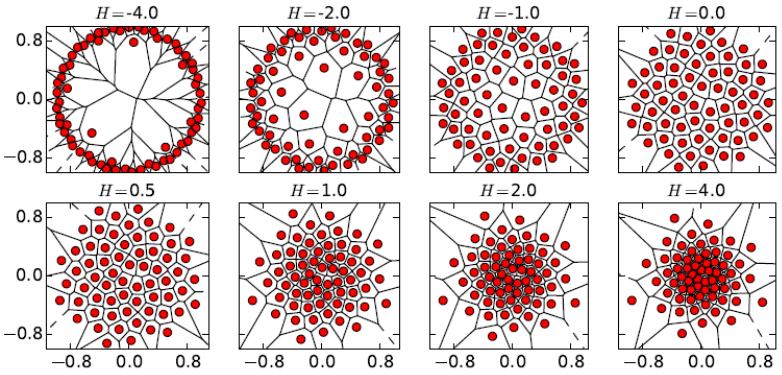

Figure 2.9: Various acoustic array geometries generated by Equations 2.17 to 2.19, setting $N = 64$, $V = 5$, and vary H, source: Sarradj (2016)

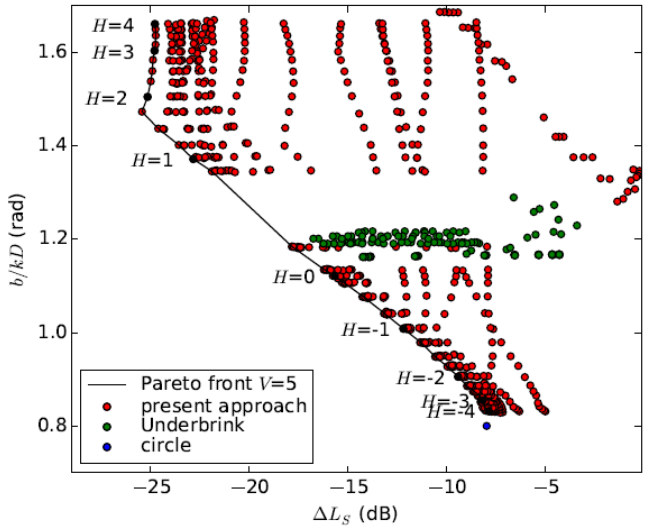

Figure 2.10: A scatter plot showing performance of arrays generated by Equations 2.17 to 2.19, setting $N = 64$, $V = 0.5$, and vary H, the parameter on the Y axis is equivalent to MLW and the parameter on the X axis is equivalent to MSL, source: Sarradj (2016)

2.4.3. Nearest Neighbor Microphone Distance

By using an array with a finite number of microphones, the distance between microphones can be critical. Consider the beamforming results with a line array having various nearest neighbor microphone distances (d_{nn}) in Figure 2.11, the grating lobes are no longer present in the directionality plot ($D(\theta)$) when the d_{nn} is lower than the wave length (λ). Analogously, for planar arrays, it has been suggested that the distance between microphones should be lower when the beamforming frequency increases (Malgoezar et al., 2016a, Nordborg et al., 2000, Schulze et al., 2004).

Malgoezar et al. (2016a) studied this relationship by performing an optimization of microphone positions on a planar array using different design frequencies. Accordingly, it was found that the distance between microphones became closer as the frequency increases. Finally, a linear relationship between the inter-microphone distance and wavelength, which can be used as a design guideline, was derived as

$$d_{nn} = 1.38\lambda = 1.38\frac{c}{f}. \tag{2.20}$$

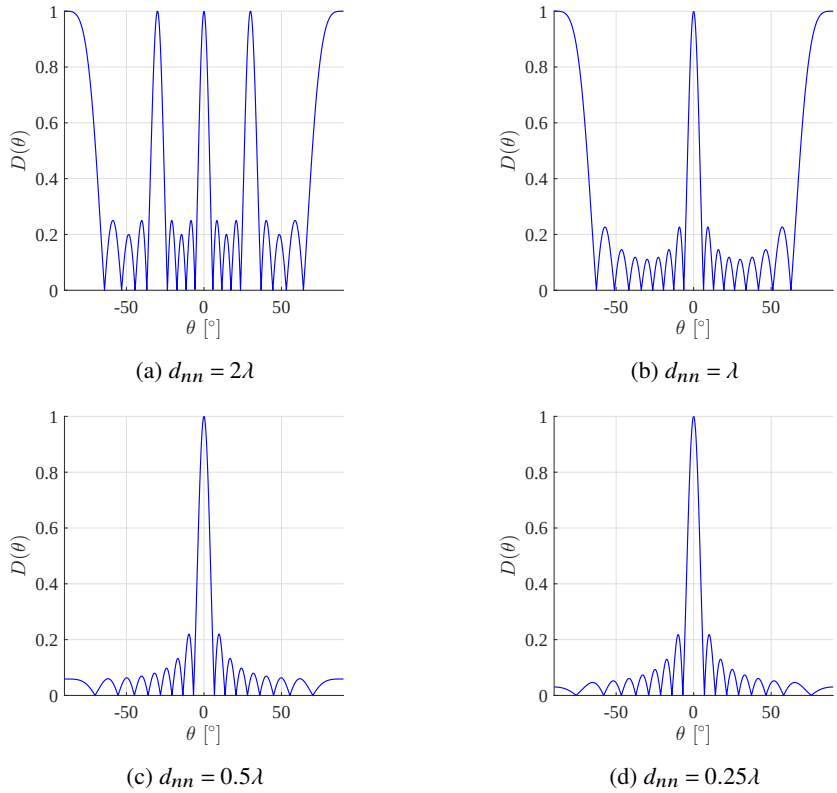

(a) $d_{nn} = 2\lambda$ (b) $d_{nn} = \lambda$

(c) $d_{nn} = 0.5\lambda$ (d) $d_{nn} = 0.25\lambda$

Figure 2.11: Directionality ($D(\theta)$) plots of a line array having the same array length with varying inter-microphone distances (d_{nn})

The relationships between the acoustic array's geometry and its beamforming performance discussed throughout this chapter are summarized in Table 2.1.

Table 2.1: Summary of beamforming performance relationship with acoustic array's geometry

Geometry	Effects	Supporting literature
Array's redundancy: odd/ even number of concentric microphone arrangement/ spiral arms/ microphones per spiral arm	Side lobes suppression ability	Yu and Donohue (2012), Underbrink (2002), Haubrich (1968), Prime et al. (2014)
Array's aperture/ dispersion: distribution of microphones wrt. radial distance from the array's centroid	Trade-off between MSL and MLW	Le Courtois et al. (2016), Babale et al. (2014), Prime and Doolan (2013), Jin and Rahmat-Samii (2007)
Nearest neighbor microphone distance	Suitable beamforming frequency	Malgoezar et al. (2016a)

3

Acoustic Array Design and Optimization

3.1. Design Benchmark for Acoustic Arrays

The knowledge of low-redundancy arrays and inter-microphone distance discussed in Section 2.4 have been employed by researchers to synthesize a number of acoustic arrays (Prime and Doolan, 2013, Underbrink, 2002). Some of these arrays have been employed by many researchers either for direct usage or comparison as benchmarking arrays (Arcondoulis et al., 2010, Prime et al., 2014, Sarradj, 2015). It has been proven and agreed that both single-arm and multi-arm spiral arrays are likely to achieve good beamforming performance, i.e. having low MSL and MLW (Nordborg et al., 2000, Underbrink, 2002, van der Goot et al., 2012). This section further discusses the ideas behind the development of the popular benchmarking arrays and provides quantitative performance evaluation results of them.

3.1.1. Single-arm Spiral Arrays

The single-arm spiral array was introduced by Dougherty (1998) and is also known as log-spiral array. Arcondoulis et al. (2010) attempted to reduce the MSL produced by the log-spiral when performing airfoil's trailing edge noise measurement by adjusting the microphone distribution in the spiral and perturbing the spiral shape. As a result, the so-called *Arcondoulis spiral* array has been proposed. The x and y coordinates of the n^{th} microphone on an Arcondoulis spiral array are

$$\mathrm{x}_n = \frac{n+\epsilon_x N}{N} a\cos(\phi_n)\exp(b\phi_n), \quad n = 1,2,\ldots,N \tag{3.1}$$

and

$$\mathrm{y}_n = \frac{n+\epsilon_y N}{N} a\sin(\phi_n)\exp(b\phi_n), \quad n = 1,2,\ldots,N, \tag{3.2}$$

repectively, where

$$\phi_n = \frac{(n-1)\Phi_{\max}}{N-1}, \quad n = 1,2,\ldots,N, \tag{3.3}$$

$$a = R_0\frac{N}{\epsilon_x N+1}, \text{ and} \tag{3.4}$$

$$b = \frac{1}{\Phi_{\max}}\ln\frac{R_{\max}}{a\sqrt{(1+\epsilon_x)^2\cos^2(\Phi_{\max})+(1+\epsilon_y)^2\sin^2(\Phi_{\max})}}. \tag{3.5}$$

The parameter R_0 is the radial distance of the innermost microphone while $R_{\max}$ and $\Phi_{\max}$ are the radial distance and the spiral angle of the outermost microphone, respectively. By varying these parameters, together with ϵ_x and ϵ_y, the shape of the Arcondoulis spiral array can be adjusted. The main feature of this array is to have denser microphone distribution close to the array's center than the log-spiral array. It has been proven that the Arcondoulis spiral array is able to achieve a lower MSL than the log-spiral array (Arcondoulis et al., 2010, Prime and Doolan, 2013). However, Prime and Doolan (2013) have identified that the performance of the Arcondoulis

spiral array in terms of MLW is not favorable, i.e. having a wide main lobe. An example of the Arcondoulis spiral array together with its co-array is shown in Figure 3.1.

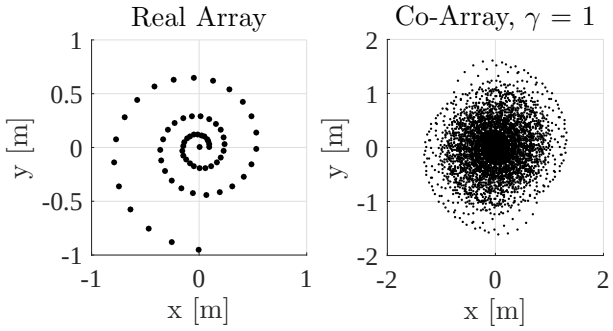

Figure 3.1: Arcondoulis spiral array (left) and co-array (right), the Arcondoulis spiral array is defined by Equations 3.1 to 3.5, setting $N = 64$, $\epsilon_x = 0.9$, $\epsilon_y = 0.9$, $\phi = 11\pi/12$ $R_{\max} = 0.95$ m, and $R_0 = 0.1R_{\max}$

3.1.2. Multi-arm Spiral Arrays

Underbrink's multi-arm spiral array (Underbrink, 2001) is another well-recognized array as it is known to provide the best trade-off between MSL and MLW (Prime and Doolan, 2013), and has been used as a benchmarking array in most array design studies (Prime et al., 2014, Sarradj, 2015). The first steps in defining an Underbrink array are to choose the inner radius (R_0) and outer radius ($R_{\max}$) together with selecting the number of spiral arms (N_a) and number of microphones per spiral arm (N_m). The radius and the angle of the n^{th} microphone on the m^{th} arm are defined in polar coordinates as

$$r_{m,n} = \begin{cases} R_0, & m = 1,2,\ldots,N_a, \quad n = 1 \\ \sqrt{\frac{2n-3}{2N_m-3}}R_{\max} & m = 1,2,\ldots,N_a, \quad n = 1,2,\ldots,N_m \end{cases} \tag{3.6}$$

and

$$\phi_{m,n} = \frac{\ln \frac{r_{m,n}}{R_0}}{\cot \nu} + \frac{m-1}{N_a}2\pi, \quad m = 1,2,\ldots,N_a, \quad n = 1,2,\ldots,N_m, \tag{3.7}$$

respectively, while ν is the spiral angle, i.e. an angle between a line drawn from the array's centroid to intersect with the spiral arm and a line tangent to the spiral arm at that point of intersection. The distribution of microphones is selected such that each microphone covers the same segment area on the array. Moreover, in this thesis, where the number of microphones is fixed to 64, the number of spiral arms is chosen to be nine, an odd number. This ensures that the number of microphones with the same radial distance is an odd number and the array's redundancy is at its lowest, $\gamma = 1$. An example of an Underbrink array is shown in Figure 3.2 together with its coarray.

Another example of a multi-arm spiral array is the Brüel & Kjær (B&K) array (Christensen and Hald, 2006) which consists of multiple linear spiral arms. The array has been designed for simple construction, due to the linear shape of the spiral arms (Prime and Doolan, 2013). However, the Underbrink array has been proven to outperform the B&K array by Prime and Doolan (2013) and Prime et al. (2014). Hence, the B&K array is not considered further in this report.

Preliminary investigations have been done in the research presented in this report to test the beamforming performance of the Arcondoulis spiral and Underbrink array (same design variables as in Figure 3.1 and 3.2). The two arrays were tested in simulations by placing a monopole at the distance (h) of 1.5 m from the array's center. The beamforming frequency (f_k) was varied from 1 to 10 kHz with a step of 1 kHz and the beamforming was performed using a scan plane of 2×2 m. Plots showing MSL and MLW of both arrays are shown in Figure 3.3 and 3.4, respectively. It can clearly be seen that the Underbrink array has better performance in terms of MLW than the Arcondoulis array as found by Prime and Doolan (2013). However, at higher frequencies, the Arcondoulis spiral array has a better side lobe suppression (lower MSL) as it has a relatively closer inter-microphone distance than the Underbrink array. Several further observations can also be made; while the MLW always monotonically decreases with frequency, the MSL does not have this monotonic trend. However, it can roughly be seen that the MSL fluctuates around a certain lower value up to 4 kHz and jumps to a higher value at this frequency. This

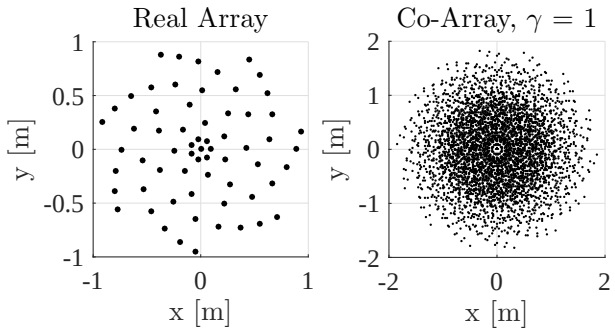

Figure 3.2: Underbrink array (left) and co-array (right), the Underbrink array is defined by Equations 3.6 to 3.7, setting $N = 64$, $N_a = 7$, $N_m = 9$, $R_{\max} = 0.95$ m, $R_0 = 0.1R_{\max}$ and $\nu = 3\pi/8$

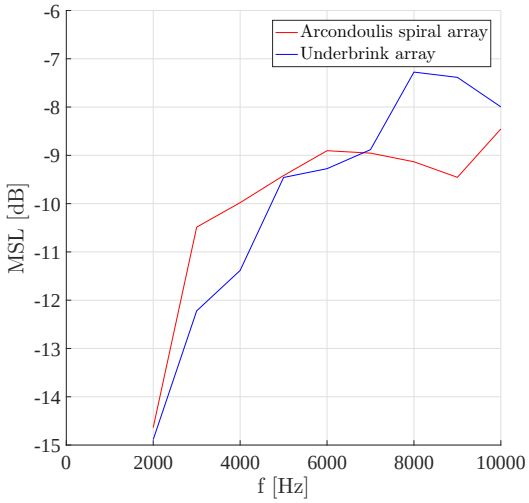

Figure 3.3: MSL of the Arcondoulis spiral and Underbrink array

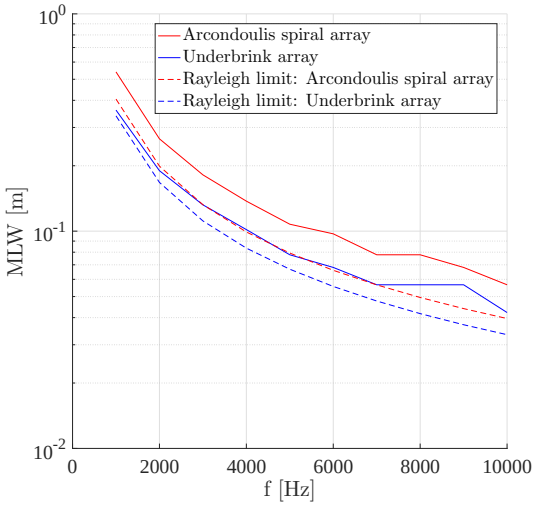

Figure 3.4: MLW and the Rayleigh limits of the Arcondoulis spiral and Underbrink array

is a common finding which also found by Yu and Donohue (2012) that since the main lobe is wide at lower frequencies, the side lobes are usually 'pushed' outside the scan area. Because of that, the values of MSL are indeterminate at 1 kHz. Therefore, observing the performance in terms of MSL at low frequencies could not provide clear implications of the array's side lobes suppression ability. In contrast, observing the MLW only at the lowest frequency can provide enough information on the array's spatial resolution due to the monotonic trend of MLW with respect to the frequency.

3.2. Optimization Problem Formulation

Although there have been many attempts in array design optimization and there are many variations of optimization strategy, the way of formulating and solving an optimization problem always consist of several common steps and components. This section summarizes the choices and variations that have been used so far by researchers in each component of the optimization problem solving, starting from the microphone locations parameterization method, the objective function, to the choice of optimization algorithm and the architecture of the optimization framework.

3.2.1. Array Parameterization and Design Vector

The first step in optimizing microphone placement on a planar array is the definition of microphone locations by means of parameterization. Different ways of parameterization require different numbers of variables to completely define the locations of all microphones on the array. These variables are passed on to the the optimization routine as a *design vector* containing all *design variables*. The more design variables the optimization

has to handle, the larger the optimization problem scale is. Therefore, different ways of parameterization can affect the problem scale, convergence time, and solution. This section discusses different ways of microphone array parameterization found in previous works, starting from the method that requires more to fewer design variables.

The most classical way of defining microphone locations on a planar acoustic array is to define the X and Y coordinates of every individual microphone such as in Malgoezar et al. (2016a) and Le Courtois et al. (2016). With this method, the size of the design vector will become $2N$ for a planar array with N microphones. Because of the continuous design variable definition, the number of design possibilities for the optimization problem will become infinite. Since the optimized microphone coordinates usually have to be fitted to a square lattice grid in real array constructions, it would be more practical to limit the possible microphone coordinates to available grid coordinates. This has inspired some researchers to parameterize the microphone location to only be on a predefined coordinates (Ayllón et al., 2014, Jin and Rahmat-Samii, 2007, Le Courtois et al., 2016). This method discretizes the optimization problem and limits possible designs to a finite number.

One way to avoid defining all microphone locations on the array and thus reduce the dimension of the design vector is to define the microphone array with concentric microphone arrangement such as in Prime et al. (2014) and Sasaki et al. (2011). As illustrated in Figure 3.5, for the i^{th} circle, the radius of the circle and the rotation of the first microphone can be defined by r_i and φ_i, respectively. Once the location of the first microphone on the circle is defined, the remaining microphones are placed with equal spacing along the circumference, hence there is no need to directly assign any design variables to those microphones. This arrangement allows a direct control of the array's aperture (Prime et al., 2014). Moreover, the concentric microphone arrangement is close to the spiral or multi-arm spiral arrangement which has been proven to have good performance (Nordborg et al., 2000, Underbrink, 2002, van der Goot et al., 2012). Despite the concentric microphone parameterization, (Prime et al., 2014) found that the microphones tend to eventually arrange themselves in a multi-arm spiral manner in the optimized design. As shown in Figure 3.6, the first and the second digits in the brackets indicate the number of the spiral arm and the number of microphones per arm, respectively, the parameter on the X and Y axis are equivalent to MLW and MSL, respectively. Prime et al. (2014) show that, for an acoustic array with 64 microphones, the multi-arm spiral microphone arrangement with 9 arms and 7 microphones per arm (plus one more microphone in the center) can achieve the lowest MSL and MLW.

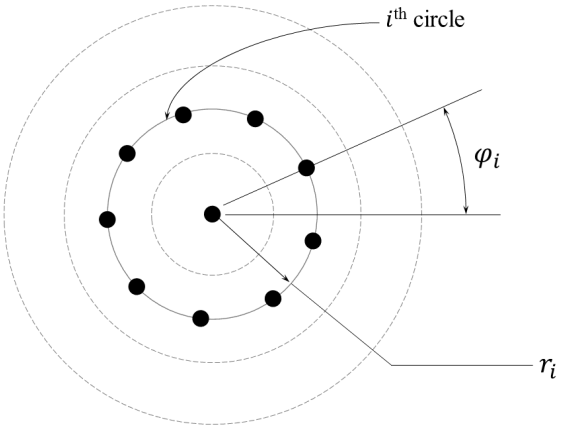

Figure 3.5: Definition of a concentric array used in Prime et al. (2014)

As mentioned in Section 2.4.2, Sarradj (2015) and Sarradj (2016) have proposed a generic way of defining an acoustic array with minimal design variables using nature-inspired equations. The microphone coordinates are defined using the equations formerly used for defining locations of sunflower seeds on a sunflower's head (Puhle and Hollands, 2016) which gives a spiral-like microphone arrangements. It has been shown that, by varying H and V from Equation 2.17 to 2.19, many different array geometries can be generated. Moreover, the MSL and the MLW can be varied as shown in Figure 2.10.

Apart from parameterizing the microphone locations for the optimization, some geometric features have been extracted from the arrays to collectively describe how all microphones are arranged on the array. One popular way of describing an array is by using a statistical distribution. Features that have been extracted and studied vary among different works. For example, Yu and Donohue (2012) studied the distribution of the Differential

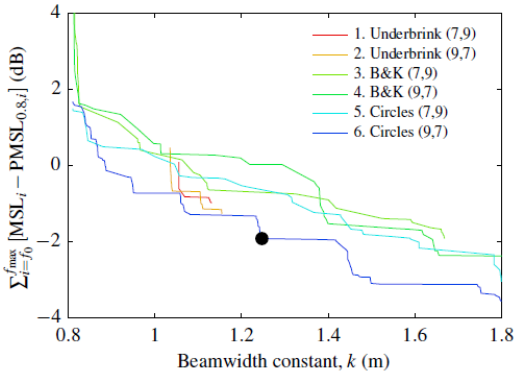

Figure 3.6: Performance of arrays considered in the research by Prime et al. (2014), the first and the second digits in the brackets indicate the number of the spiral arm and the number of microphones per arm, respectively, the parameter on the X and Y axis are equivalent to MLW and MSL, respectively, source: Prime et al. (2014)

Path Distance (DPD) to ensure array's irregularity, Puhle and Hollands (2016) considered the microphone density with respect to the radial distance on the array, and Malgoezar et al. (2016a) studied the distribution and variety of nearest neighbor microphone distance with respect to the design frequency and number of iterations in the optimization. The distance between microphones, or microphone density, are sometimes linked to the weighing function usually applied to each microphone in beamforming (Sarradj, 2015, Sijtsma and Stoker, 2004). By describing an acoustic array through the use of a statistical measure of microphone features could also be a promising way of microphone array parameterization in the optimization since only a few variables, such as the mean and the standard deviation, are required to describe the distribution. Moreover, it is not necessary for arrays with the same geometric or statistical feature to have exactly the same microphone arrangement. Thus, there is no need to search for the one-and-only optimized design in the optimization as long as every array that shares the same geometric feature can achieve similarly good performance.

3.2.2. Objective Function and Model

The most popular objective of optimizing a microphone array is to have a microphone array that gives as low as possible side lobes. Therefore, this objective is usually implemented in the optimization such that MSL is minimized (Le Courtois et al., 2016, Prime et al., 2014). Similar objective functions are the maximization of the Main lobe Peak to Side lobe Ratio (MPSR) (Yu and Donohue, 2012) or the Signal to Noise Ratio (SNR) (Ayllón et al., 2014, Sarradj et al., 2006, Yu and Donohue, 2012, 2013), which are conceptually the same as MSL. The previously-mentioned work searches through the entire beampattern to find the interference while some researchers seek to minimize side lobes more specifically. For example, Austeng et al. (1997) applied weights to the side lobes and attempted to minimize the maximally-weighted side lobe while Malgoezar et al. (2016a) defined a ring-like domain around the main lobe and minimize side lobes in that particular area.

Another objective when optimizing an acoustic array is to maximize the array's resolution. High resolution can ensure the separability of sources placed closely together and this can be achieved by minimizing the MLW. A number of researchers have attempted to include the minimization of the MLW in the objective function and minimize it simultaneously with the MSL (Le Courtois et al., 2016, Prime et al., 2014, Sarradj, 2016). This makes the optimization problem a multi-objective optimization, as discussed in Section 2.4.2, in which the two objectives lead to opposite designs and a proper compromise has to be found.

There exist several techniques for combining multiple objective functions into one. Let J_{MSL} and J_{MLW} be generic objective functions associated with MSL and MLW, respectively. The aim is to minimize the values of both J_{MSL} and J_{MLW}. For example, Jin and Rahmat-Samii (2007) employed the Conventional Weighted Aggregation (CWA) method which combines the two parameters into one objective function as

$$J = \alpha J_{\mathrm{MSL}} + \beta J_{\mathrm{MLW}}, \tag{3.8}$$

where α and β are the weighing coefficients to be determined while Le Courtois et al. (2016) proposed other ways of formulating the objective function such as

$$J = J_{\mathrm{MSL}} J_{\mathrm{MLW}}. \tag{3.9}$$

It is however complicated to judge which method works most efficiently for this optimization problem. Moreover, some methods such as the Conventional Weighted Aggregation (CWA) also require a determination of some other parameters (α and β in Equation 3.8), in order to give proper results. The MSL and MLW can be visualized separately on a scatter plot similar to a pareto plot and the designs can freely be chosen from the Pareto front as done by Sarradj (2016), Sarradj (2015), and Prime et al. (2014).

Another indispensable part of the objective function is the model. In this optimization problem, in order to get the exact MSL and MLW values for each design, it is necessary to carry out a beamforming simulation while evaluating the objective function. For planar microphone array optimization, most researchers opt for the most simple case by simulating a single sound source in the middle of the scan plane (Malgoezar et al., 2016a, Prime and Doolan, 2013, Sarradj, 2015, 2016). In practice, the frequency (range), the location, and the Sound Pressure Level (SPL) of the monopole vary.

3.2.3. Optimization Algorithm and Framework

Due to the nature of the acoustic array optimization problem which is non-linear and non-convex (Chan et al., 2017, Li et al., 2013), most researchers have employed 0^{th} order random search algorithms which do not require gradient information to solve this problem. Several variations in algorithm choices exist, but these algorithms also share some common characteristics, including heuristic or evolutionary processes and assess a set of design vectors (the *swarm* or *population*) in each iteration.

The most popularly-used algorithm is the Genetic Algorithm (GA) (Haupt, 1994, Le Courtois et al., 2016, Li et al., 2013, Malgoezar et al., 2016a, Yu and Donohue, 2013, Yu et al., 2013) which mimics the evolution of organisms through a number of generations. In this optimization, a set of different microphone array design vectors (*individuals*) is defined as a *population*. In each iteration (*generation*) every design in the population is evaluated by the objective (*fitness*) function. After that, each individual will undergo a *reproduction* (*immortal elite*, according to Yu and Donohue (2013) and Yu et al. (2013)), *crossover*, or *mutation* operations, based on their performance. The purpose is to maintain and/or improve performance of the population by keeping individuals that have good performance, blending good features of different individuals to create a better individual, or applying some perturbations. The optimal design is often chosen by taking the best individual in the final generation. Alternatively, other individuals in this generation could also be collectively considered as a set of optimal designs. Therefore, this algorithm gives a set of solutions that the designer can explore and choose. Another similar algorithm is the Differential Evolution (DE) algorithm used by Malgoezar et al. (2016a). This is a variant of GA which also involves partner generation, crossover, and selection operations, controlled by certain predefined probability and factor. Apart from GA and DE, the Particle Swarm Optimization (PSO) algorithm was also employed in several works (Jin and Rahmat-Samii, 2007, Recioui, 2012). This algorithm simulates the behavior of an insect swarm when they are looking for a region with an abundance of food resources. Different individuals in the swarm represent different design vectors based on their location in the design space. These individuals will move around in the design space with a certain direction and speed which are controlled by the best location they have found themselves and the best location found by the entire swarm. This information is updated in every time step until the swarm finds the optimal solution.

Several issues have been encountered by the researchers when attempting to implement the aforementioned algorithms for solving the acoustic array optimization problem. First, the algorithms tend to have premature convergence and converge to local minima (Chan et al., 2017). Second, since every individual has to be evaluated in the objective function in each generation or time step, this evaluation can be time-consuming, especially when the objective function evaluation involves expensive beamforming simulation (Chan et al., 2017, Sarradj, 2015, Yu and Donohue, 2012). Finally, the first two problems can be more pronounced when the problem scale is large, i.e. having more microphones to be placed on the array and/or more design variables (Chan et al., 2017, Yu and Donohue, 2012). Therefore, a good optimization framework, including an efficient way of array parameterization and a suitable optimization algorithm should be formulated.

Some adjustments or modifications have usually been made in the optimization framework. In GAs, the dynamic *mutation rate* is often used to help jump out of local minima. For example, (Yu and Donohue, 2013) and (Yu et al., 2013) have employed decaying mutation rate which decreases as the number of generation increases. On the other hand, (Ayllón et al., 2014) abruptly increases the mutation rate when the optimization is likely to converge. Apart from that, some researchers have introduced hybrid methods in which the evolutionary algorithms are coupled with some other algorithms. For instance, (Li et al., 2013) introduced the *hybrid descent method* which uses GA to find local minima and a gradient-based optimization to move between different minima.

3.3. Design Considerations for Wind Tunnel Measurements

This section scopes the review down to acoustic array design for wind tunnel measurements. Scenarios and complications that might be encountered in this particular application and should be kept in mind when designing the V-tunnel array are discussed.

3.3.1. Relevant Frequency Band

A specific frequency range is the most crucial feature that must be defined before starting the array design process (Underbrink, 2002). As discussed in Section 2.4.3, this directly affects the resulting nearest neighbor microphone distance on the array. If the frequency range is large, the inter-microphone distance on the array will vary largely, having dense microphones locations close to the array's centroid while gradually reducing the density when moving towards the array's edge. It has been suggested by Underbrink (2002) that when an array is meant to be used at any beamforming frequency f_k where $f_{k,\min} \leq f_k \leq f_{k,\max}$ and $f_{k,\max}/f_{k,\min} \leq 10$, the whole array can be designed as one array. An example is the optimized array by (Prime et al., 2014) that was used in a frequency range between 2 and 12 kHz. When $f_{k,\max}/f_{k,\min}$ is larger, it is recommended to have a *nested array*, i.e. a smaller array in the middle of a larger array. An example of a nested array in a wind tunnel application can be found in Shin et al. (2007) which was intended to be used in a large frequency range, 650 Hz to 50 kHz. However, this array is not a product of an optimization process.

3.3.2. Source Characteristics

Although the source model used in the optimization routine is usually the simplest monopole source according to Section 3.2.2, more complex sources can be found in real wind tunnel applications.

Trailing edge noise is one of the most common measured phenomena in aero-acoustic applications (Arcondoulis et al., 2010, Ehrenfried et al., 2006). Instead of being a point source, this will appear as a line source. One way to approximate a line source is by simulating a line array of monopoles (Crocker, 1998). When the number of monopoles is high enough, i.e. monopoles are placed densely together, a line-like source can be produced.

Another situation that can be found in wind tunnel measurements is the case with multiple sources. These can be arranged either arbitrarily in a 3D space such as complex landing gear noise measurements (Sarradj, 2012) or in a circular manner such as for rotor noise measurements (Prime et al., 2014, Sijtsma et al., 2001).

3.3.3. Influences of Flow on the Aero-acoustic Measurements

Different noise sources can be expected depending on how the acoustic arrays are installed. For wall-mounted acoustic arrays, the array is underneath the turbulent boundary layer of the wind tunnel wall. The noise level depends on the roughness of the wall and can be reduced by covering the microphones with a certain type of material (Soderman and Allen, 2002). On the other hand, microphone arrays can also be placed outside the flow in case of open jet wind tunnels. The main noise source of this setting is the shear layer which can add noise to the measurement. For example, when the sound source in the flow is tonal, the spectrum of the sound received by the microphone array will become broadband, and the sound magnitude and the coherence of signal received can be weakened. This phenomenon is called *spectral broadening* (Sulaiman, 2011). Apart from that, since the sound has to travel through moving air inside the flow and still air outside the flow before reaching the microphone, the sound propagation path can deviate from straight propagation paths by *refraction* and the measured noise source locations can be shifted. More details on this topic are given in the case study discussed in Chapter 7, Section 7.3.

Apart from the types of array installation, the environment in the wind tunnel can also affect the acoustic measurements. If the wind tunnel is anechoic, it can be assumed that the sound propagates only directly from the source to the microphone. However, if the wind tunnel wall is hard, the indirect sound propagation from reflection will also affect the measurement. This could result in mirrored noise sources which would affect the interpretation of acoustic images. This becomes even worse if the array does not have good enough spatial resolution (Dougherty, 1998).

4

Optimization Methodology

4.1. Overview of the Optimization Methodology

The idea of the proposed optimization method is to utilize the known relationships between the array geometry and performance. Apart from that, to avoid convergence to local minima and optimization time problems, the number of design variables used is selected to be as low as possible. Beamforming simulation is only done when necessary.

The proposed optimization method is schematically shown in Figure 4.1. The optimization routine consists of one main optimization loop and a nested optimization loop. The main optimization loop has four design variables, μ_{nr}, σ_{nr}, μ_{nn}, and σ_{nn}. These variables are used to collectively describe the microphone distribution on the array. They are parsed to the nested optimization loop which attempts to generate a set of multi-arm spiral arrays that has the geometry as close as possible to the predefined geometry descriptions. The assumption is that arrays designed by the same combination of geometry descriptors have similar performance with regards to MSL and MLW, i.e. they will cluster close together as schematically shown in the plot in Figure 4.1. The main optimization loop attempts to find a set of geometry descriptors which can be used to generate an array with as low as possible MSL and MLW.

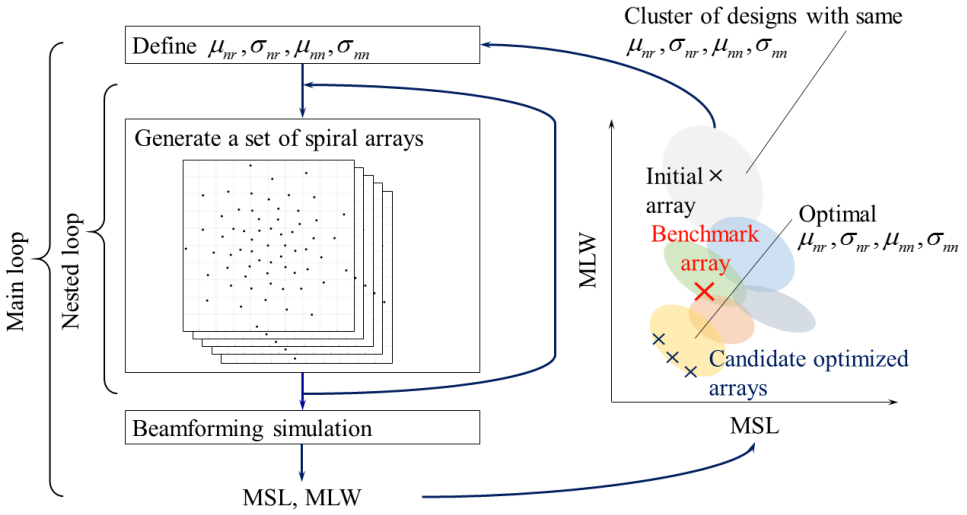

Figure 4.1: Schematic diagram of the proposed optimization method

The remainder of this chapter explains both optimization loops in detail; the main optimization loop in Section 4.2 and the nested optimization loop in Section 4.3. The formulation of the optimization problem, the definition of the design variables and the objective functions, in each loop are discussed. The utilized optimization algorithms are explained.

4.2. The Main Optimization Loop

4.2.1. Optimization Problem Formulation

There are four design variables in this optimization loop, μ_{nr}, σ_{nr}, μ_{nn}, and σ_{nn} which are the parameters in the truncated normal distribution. They affect the array's geometry as follows:

- μ_{nr} and σ_{nr} describe the microphone distribution along the array's radial distance
  - μ_{nr} describes the center of microphone distribution along the array's radial distance
  - σ_{nr} describes the standard deviation of the microphone distribution
- μ_{nn} and σ_{nn} describe the shape of a curve that represents the relationship between the microphone's radial distance on the array and that microphone's nearest distance to its neighbour microphone
  - μ_{nn} describes the location of the inflection point on the curve
  - σ_{nn} describes the smoothness of the curve

These design variables are involved in the definition of an array as follows. Suppose that the radial distance on the array is discretized into n_{bin} statistical bins (intervals), then the expected number of microphones at the b^{th} bin (N_{r_b}) which is centered at r_b on the array is

$$N_{r_b} = \frac{N f_r(r_b)}{\sum_{b=1}^{n_{\text{bin}}} f_r(r_b)}, \tag{4.1}$$

where N is the total number of microphones on the array, the summation term in the denominator is summed over all bins in the array's radial distance, and $f_r(r_b)$ returns the probability from the Probability Distribution Function (PDF) of a truncated normal distribution at the radial distance r_b. This function is defined as

$$f_r(r;\mu_{nr},\sigma_{nr},R_{\max}) = \frac{\psi(\frac{r-\mu_{nr}}{\sigma_{nr}})}{\sigma_{nr}\left[\chi(\frac{R_{\max}-\mu_{nr}}{\sigma_{nr}}) - \chi(\frac{-\mu_{nr}}{\sigma_{nr}})\right]}, \tag{4.2}$$

where $R_{\max}$ is the maximum radius of the array in m,

$$\psi(x) = \frac{1}{2\pi}\exp\left(-\frac{1}{2}x^2\right), \tag{4.3}$$

and

$$\chi(x) = \frac{1}{2}(1+\text{erf}(x/\sqrt{2})), \tag{4.4}$$

where erf(x) is the error function. By adjusting μ_{nr} and σ_{nr}, different distributions can be obtained as shown in Figure 4.2.

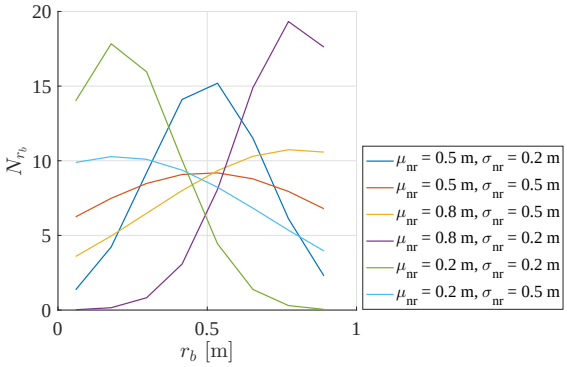

Figure 4.2: Example of PDFs from the truncated normal distribution with varying μ_{nr} and σ_{nr}

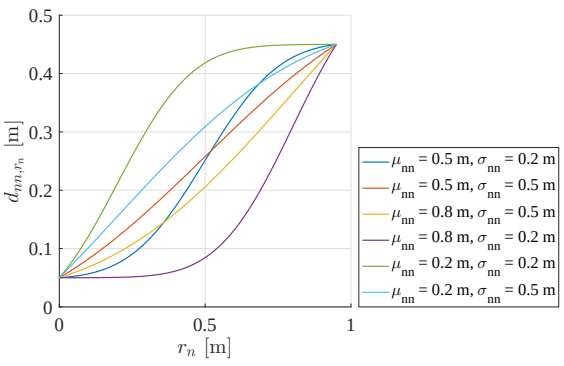

Figure 4.3: Example of CDFs from the truncated normal distribution with varying μ_{nn} and σ_{nn}

Second, the nearest neighboring microphone distance of the n^{th} microphone at the distance r_n, d_{nn,r_n}, is described by the Cumulated Distribution Function (CDF) of the truncated normal distribution function described by μ_{nn} and σ_{nn}. The value of d_{nn,r_n} at any arbitrary distances r_n can be determined from

$$d_{nn,r_n} = nn_{\min} + F_r(r_n)(nn_{\max} - nn_{\min}), \tag{4.5}$$

where, $nn_{\min}$ and $nn_{\max}$ are the minimum and maximum nearest neighbor microphone distance in m of all microphones on the array, respectively, and the CDF is defined as

$$F_r(r; \mu_{nn}, \sigma_{nn}, R_{\max}) = \frac{\chi(\frac{r-\mu_{nn}}{\sigma_{nn}}) - \chi(\frac{-\mu_{nn}}{\sigma_{nn}})}{\chi(\frac{R_{\max}-\mu_{nr}}{\sigma_{nr}}) - \chi(\frac{-\mu_{nr}}{\sigma_{nr}})}. \tag{4.6}$$

Again, by varying the values of μ_{nn} and σ_{nn}, the curve representing the relationship between the radial distance of the microphone and its nearest neighbor distance can be adjusted. It is assumed that the inter-microphone distance will increase as the microphone is further away from the array's centroid. The minimum and maximum possible values of d_{nn}, $nn_{\min}$ and $nn_{\max}$, are chosen to be 0.05 m and 0.45 m, according to the relationship given by Malgoezar et al. (2016a) shown in Equation 2.20 and the design operating frequency range of the array, which ranges from 1 to 10 kHz. An example of different curves for different combinations of μ_{nn} and σ_{nn} is shown in Figure 4.3.

Given the array's size of 2×2 m, the bounds for all design variables; μ_{nr}, σ_{nr}, μ_{nn}, and σ_{nn}, are set to be 0.1 to 1 m. Examples of arrays generated by the extreme values of these variables are shown in Figure 4.4.

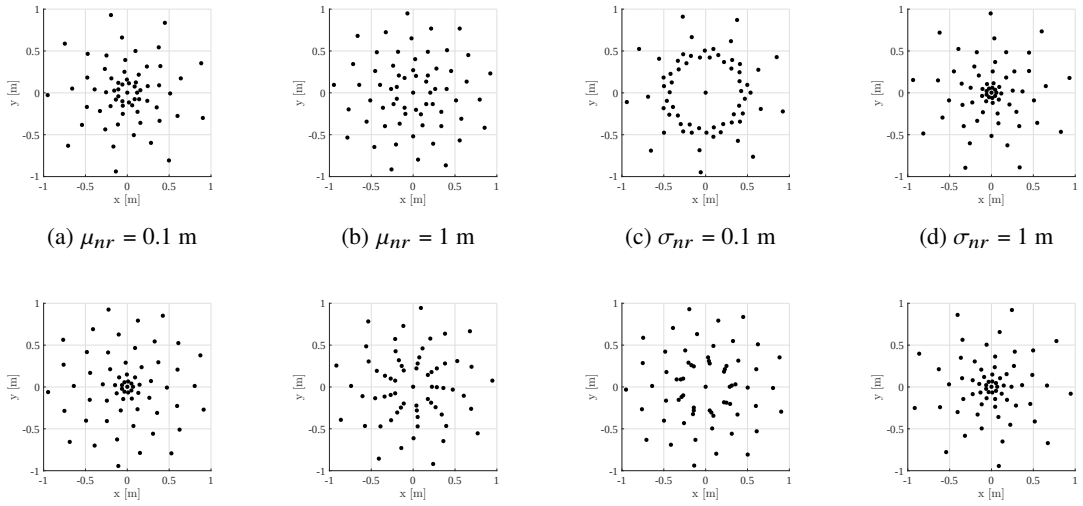

(a) μ_{nr} = 0.1 m (b) μ_{nr} = 1 m (c) σ_{nr} = 0.1 m (d) σ_{nr} = 1 m

(e) μ_{nn} = 0.1 m (f) μ_{nn} = 1 m (g) σ_{nn} = 0.1 m (h) σ_{nn} = 1 m

Figure 4.4: Examples of acoustic arrays generated by extreme values of μ_{nr}, σ_{nr}, μ_{nn}, and σ_{nn}, the remaining values of μ_{nr}, σ_{nr}, μ_{nn}, and σ_{nn} are fixed at 0.5 m, unless indicated

The specified set of μ_{nr}, σ_{nr}, μ_{nn}, and σ_{nn} is parsed to the nested optimization loop which attempts to generate a set of multi-arm spiral array that has the geometry as close as possible to the predefined geometry descriptors. Having obtained the set of arrays, the beamforming performance of them are evaluated. The simulation attempts to replicate the real usage in the wind tunnel as shown in Figure 4.5. One source emitting white noise is placed at 1.5 m in front of the array. It is assumed that the scan plane to be used in the real application is 1×1 m but the scan plane in the optimization is extended to a circular area having a diameter of 2 m to account for the uncertainty of the source's location. The beamforming is performed at 8 frequencies within the design frequency range of 1 to 10 kHz. The MLW is evaluated only at the lowest frequency of 1 kHz since it is known that the MLW reduces with frequency. However, the MSL is evaluated and averaged at 4 to 10 kHz with a step of 1 kHz due to the non-monotonic trend of MSL with the beamforming frequency.

Let $\overline{MLW}$ and $\overline{MSL}$ denote the averaged values of MLW and MSL obtained from the beamforming evaluation of all generated multi-arm spiral arrays using a certain fixed combination from the set of μ_{nr}, σ_{nr}, μ_{nn}, and σ_{nn} over all relevant frequencies. The objective function of the main optimization loop, which attempts to minimize both MLW and MSL, simultaneously can be written as

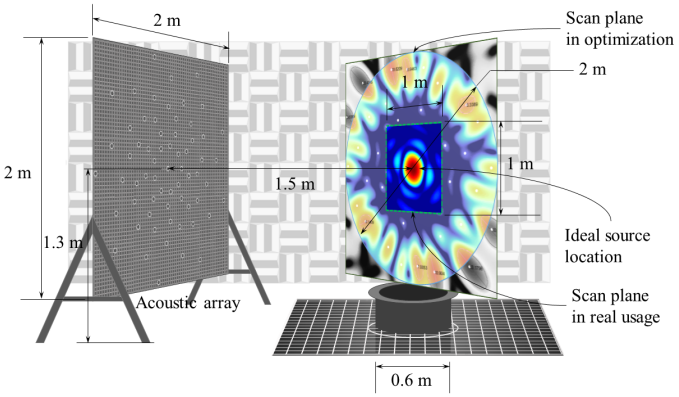

Figure 4.5: Beamforming in the wind tunnel simulated in the optimization

$$J_{\text{main}} = \frac{\overline{MSL} - MSL_{\text{ref}}}{-MSL_{\text{ref}}} + \frac{\overline{MLW} - MLW_{\text{ref}}}{MLW_{\text{ref}}}. \tag{4.7}$$

This function is to be minimized, where MLW_{ref} and MSL_{ref} are the reference values of MLW and MSL, respectively. The minus term is used such that, when the difference between the actual and the reference value is high, the objective function is high, and vice versa. Since the units of MSL and MLW are different, the normalization is done to ensure that the two different quantities can be combined in one objective function. The values of MLW_{ref} and MSL_{ref} can influence the relative importance of MSL and MLW minimization in the objective function, in the same manner as α and β in Equation 3.8. The selection of these reference values are to be done in the optimization algorithm tuning step which will be presented later.

4.2.2. The Optimization Algorithm

The optimization problem in this main optimization loop has four bounded design variables, μ_{nr}, σ_{nr}, μ_{nn}, and σ_{nn}. The objective function is defined in Equation 4.7. The main objective function is expected to be more computationally expensive than the objective function in the nested optimization loop since it requires a beamforming simulation in order to evaluate the values of MSL and MLW. In addition, the generation of the multi-arm spiral array using the nested optimization loop is also one step to take in evaluating this objective function. It will be shown further that the optimization implemented in the nested nested loop is stochastic. As a result, the objective function in the main optimization loop is also stochastic. Therefore, the optimization algorithm for the main optimization loop should be suitable to account for these conditions.

The Hooke-Jeeves (HJ) algorithm (Hooke and Jeeves, 1961) is in the family of the Generalized Pattern Search Algorithms (GPS) (Torczon, 1997) which are 0^{th} order optimization methods, i.e. do not require the gradient information of the objective function. This algorithm has been employed in various design optimization problems, especially problems which require simulation such as sensor placement design (Beal et al., 2008) or Heating, Ventilation and Air Conditioning (HVAC) system design (Wetter and Wright, 2003), as it is stated that it requires less objective function evaluations compared to GA or PSO. Moreover, it is able to handle non-smooth objective functions or objective functions which involves stochastic processes (Sriver et al., 2009). The algorithm has been extended to cover a number of more complicated optimization problems, including a case where the design variables are subjected to predefined bounds (the bound-constrained case) (Lewis and Torczon, 1999). This will also be used in solving this particular optimization problem.

Let $\mathbf{X}_q$ be the design vector at the q^{th} iteration containing n design variables. The design vector is bounded by the lower bound ($\mathbf{X}_{\text{LB}}$) and the upper bound ($\mathbf{X}_{\text{UB}}$). Let Ω denote the feasible design space such that for all $\mathbf{X}$, $\{\mathbf{X} : \mathbf{X} \in \Omega, \mathbf{X}_{\text{LB}} \leq \mathbf{X} \leq \mathbf{X}_{\text{UB}}\}$.

For a given $\mathbf{X}_q \in \Omega$, there exist a set of design points ($\mathbf{M}$) or a *mesh* defined by

$$\mathbf{M} = \{\mathbf{X} \in \Omega, \mathbf{X} = \mathbf{X}_q + \Delta_q \mathbf{D}_c, c = 1, 2, \ldots, 2n\}, \tag{4.8}$$

where $\Delta_q > 0$ is the *mesh size factor* at the q^{th} iteration, $\mathbf{D}_c$ is the c^{th} column in the matrix $\mathbf{D}$ which is the matrix denoting the search pattern. In different variations of the HJ or the GPS algorithm, the definition of matrix $\mathbf{D}$ varies. In this optimization problem, $\mathbf{D}$ is defined to be a concatenation of an identity matrix ($\mathbf{I}$) of dimension

$n \times n$ and a negative identity matrix ($-\mathbf{I}$) of dimension $n \times n$, $\mathbf{D} = [\mathbf{I}|-\mathbf{I}]$. Therefore, the number of columns in $\mathbf{D}$ is $2n$, i.e. twice as much as the number of the design variables.

The design points $\mathbf{X} \in \mathbf{M}$ are basically the set of points in the design space spanning in all possible dimensions of the design space in both positive and negative directions (as a result of $\mathbf{I}$ and $-\mathbf{I}$ in $\mathbf{D}$) and centered at $\mathbf{X}_q$. The value of Δ_q determines how far those points are from $\mathbf{X}_q$.

Since this optimization problem is bounded, it is possible that some search directions will fall outside the bounds. Some adjustments have to be made to ensure that those search directions which exceed the bounds will stay on the nearest bounds. Let $X^i_{q,c}$ be the i^{th} dimension of X_q subjected to the c^{th} search pattern, i.e. $X^i_{q,c} = X^i_q + D^i_c$, according to the method suggested by (Lewis and Torczon, 1999), for all $X^i_{q,c} \in \mathbf{X} \in \mathbf{M}$ and $i = 1, 2, \ldots, n$,

$$X^i_{q,c} = \begin{cases} X^i_{\text{LB}}, & X^i_{q,c} < X^i_{\text{LB}} \\ X^i_{q,c}, & X^i_{\text{LB}} \le X^i_{q,c} \le X^i_{\text{UB}} \\ X^i_{\text{UB}}, & X^i_{q,c} > X^i_{\text{UB}} \end{cases} . \tag{4.9}$$

At the q^{th} iteration, the objective function is evaluated at $\mathbf{X}_q$ and all $\mathbf{X} \in \mathbf{M}$. Let $\mathbf{X}' \in \mathbf{M}$ be $\mathbf{X}' = \mathbf{X}_q + \Delta_q \mathbf{D}_{c'}$ which gives the lowest $J_{\text{main}}(\mathbf{X}')$ amongst all other $J_{\text{main}}(\mathbf{X})$ calculated from all $\mathbf{X} \in \mathbf{M}$. If $J_{\text{main}}(\mathbf{X}_q) - J_{\text{main}}(\mathbf{X}') > \tau$ where τ is a tolerance, that point in the mesh has led to a lower value of J_{main}, we then set $\mathbf{X}_{q+1} = \mathbf{X}'$. Otherwise, there is no surrounding points which gives an improved J_{main}, the next iteration will stay at the same point and search using a more refined set of mesh points which lie closer to $\mathbf{X}_q$, setting $\mathbf{X}_{q+1} = \mathbf{X}_q$. The mesh size factor is reduced as $\Delta_{q+1} = m\Delta_q$ where $0 < m < 1$.

The optimization will terminate when $\Delta_q < \Delta_{\text{min}}$, where Δ_{min} is the predefined minimum mesh size factor. The workflow of the HJ/GPS algorithm is shown in Figure 4.6.

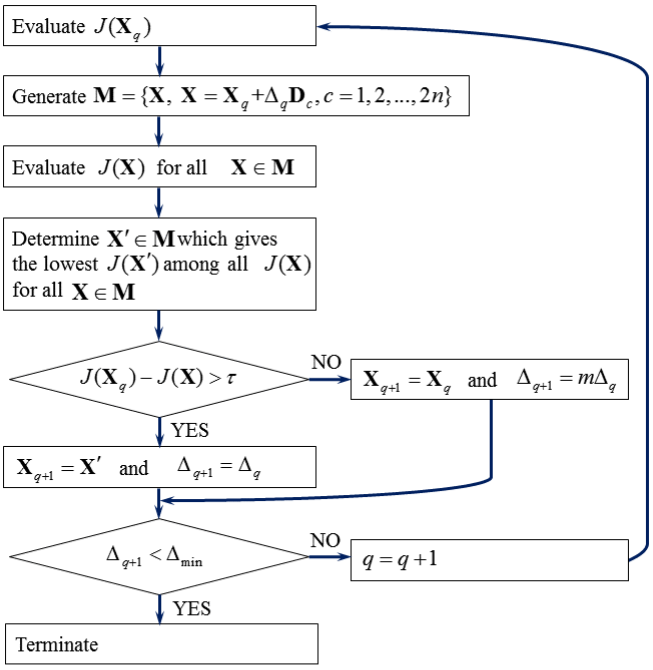

Figure 4.6: Flowchart of the HJ/GPS algorithm

An exemplary schematic diagram illustrating the convergence of the HJ/GPS algorithm having $n = 2$ is shown in Figure 4.7. At $q = 0$ one point $\mathbf{X} \in \mathbf{M}$ exceeds the upper bound. It is adjusted to lie on the upper bound. Then it is found that there exist $\mathbf{X}' \in \mathbf{M}$ that gives a lower value of the objective function. Therefore, this point becomes the center point of the mesh in the next iteration, $\mathbf{X}_1 = \mathbf{X}'$. The optimization proceeds in the same manner until $q = 3$ where no $\mathbf{X} \in \mathbf{M}$ gives a lower value of the objective function. The center point then remains at the same point when $q = 4$, $\mathbf{X}_4 = \mathbf{X}_5$. The optimization progresses further in a similar manner until it reaches the optimal point.

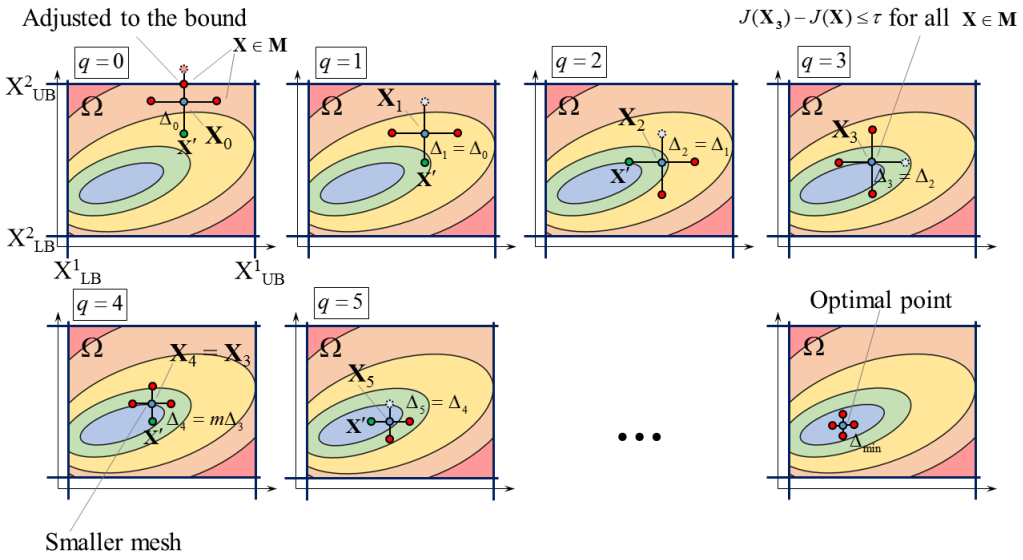

Figure 4.7: Schematic example of the HJ/GPS optimization applied to a problem with $n = 2$, the adjusted bound is shown at $q = 0$, at $q = 3$ there are no points which gives an improved value of J found so Δ is reduced at $q = 4$

It is notable that the definition of the search pattern (**D**) can be critical in the case of bound-constrained optimization, it should be ensured that there exist one direction in **D** which points parallel to the constraint boundary so that it is possible for the algorithm to iterate along this boundary when the optimal point lies on the constraint, i.e. boundary of Ω (Beal et al., 2008, Lewis and Torczon, 1999). An illustration is shown in Figure 4.8 where the optimization is bounded and the optimal point lies on the lower bound of one design variable. Two different definitions of **D** are graphically presented. The definition of **D** in the left figure creates a mesh parallel to the bounds while that in the right figure does not. Only the optimization in the left figure can reach the true optimal point on the bound due to its ability to iterate along the bound. This explains why the matrix **D** is defined as $\mathbf{D} = [\mathbf{I}|-\mathbf{I}]$ in this particular optimization case.

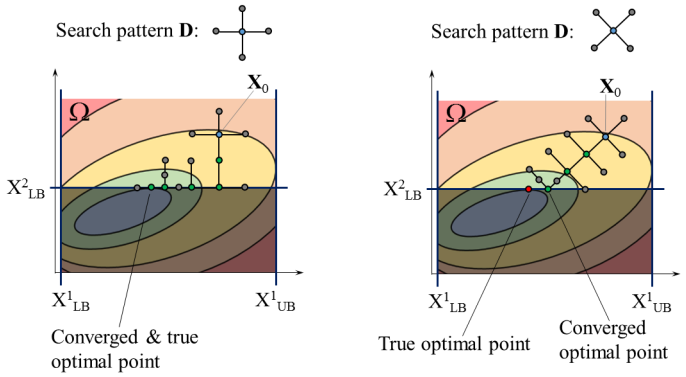

Figure 4.8: Convergence of the HJ/GPS algorithm starting from the same $\mathbf{X}_0$ having different search patterns **D**; **D** has a direction parallel to the bound and converges to the true optimal point (left) and **D** has no direction parallel to the bound and converges to a wrong point (right)

4.2.3. Tuning and Testing the Optimization

To test the sensitivity of MSL and MLW with varying μ_{nr}, σ_{nr}, μ_{nn}, and σ_{nn}, each one of these variables is varied from 0.1 to 1 m with a step of 0.025 m while keeping the remaining variables at 0.5 m. The nested optimization loop is used to generate a set of five multi-arm spiral arrays for each combination of μ_{nr}, σ_{nr}, μ_{nn}, and σ_{nn}. Beamforming simulation using the settings as described in Section 4.2.1 is used to determine the values of MSL and MLW for every array. The results are shown in Figure 4.9. The left column shows the averaged MSL and the right column shows the averaged MLW. For different rows, different variables from μ_{nr}, σ_{nr}, μ_{nn}, and σ_{nn} are varied while the rest are kept constant.

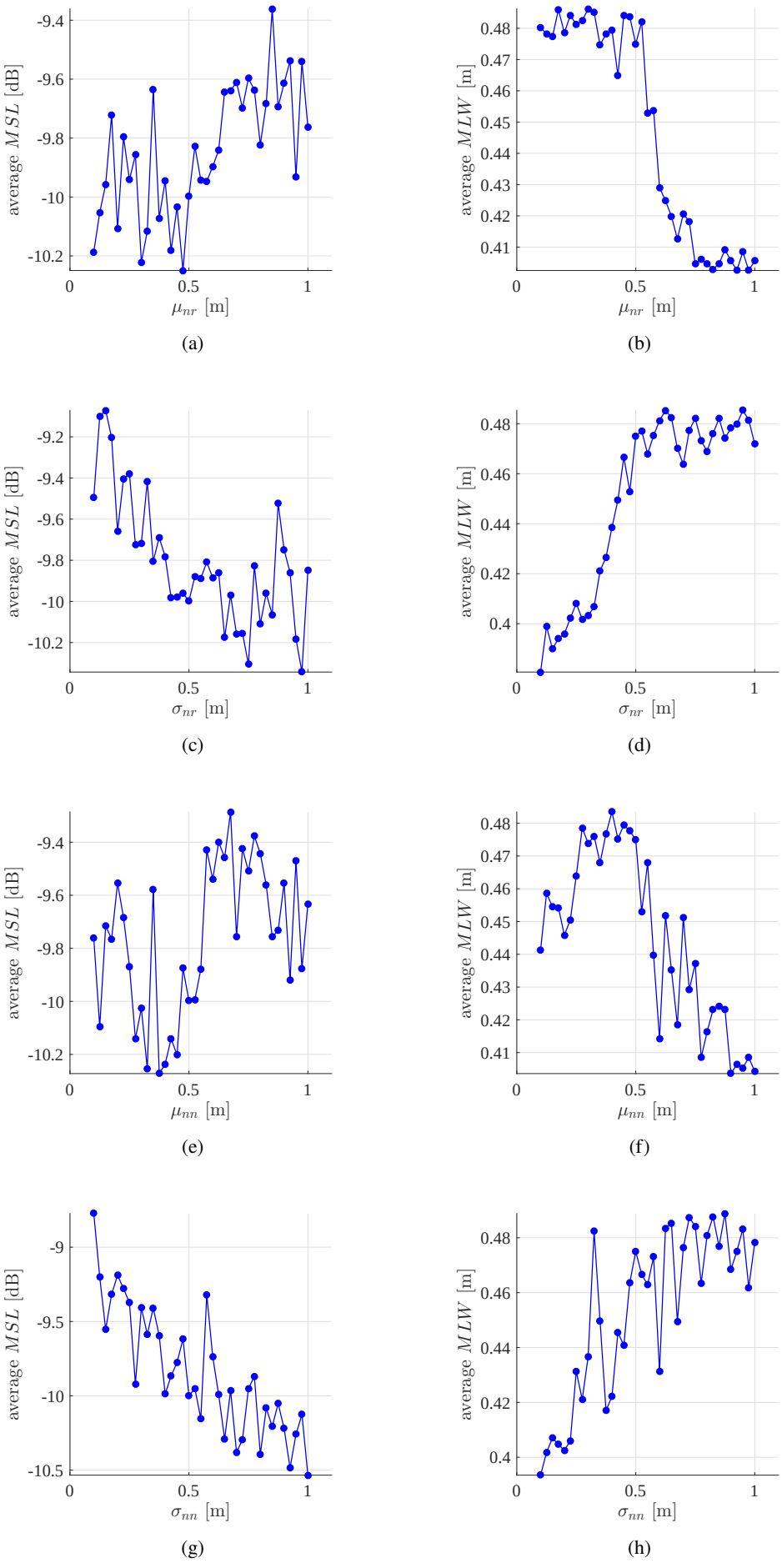

Figure 4.9: Sensitivities of averaged MSL ((a), (c), (e), and (g)) and averaged MLW ((b), (d), (f), and (h)) wrt. μ_{nr} ((a) and (b)), σ_{nr} ((c) and (d)), μ_{nn} ((e) and (f)), and σ_{nn} ((g) and (h))

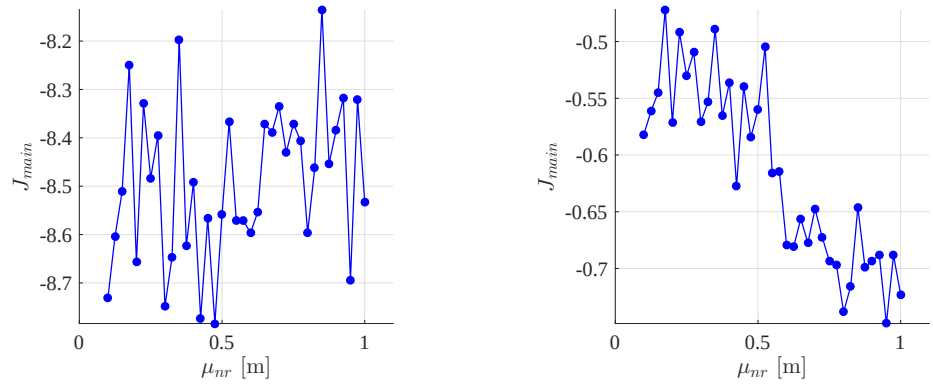

(a) MSL_{ref} = -1 dB

(b) MSL_{ref} = -5 dB

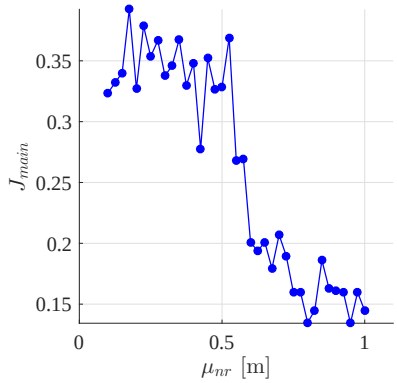

(c) MSL_{ref} = -9 dB

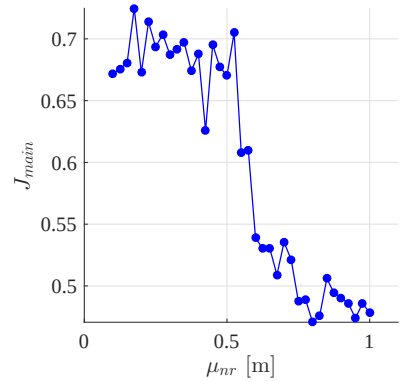

(d) MSL_{ref} = -14 dB

Figure 4.10: Sensitivities of J_{main} wrt. μ_{nr} with different settings of MSL_{ref}

From the plots in Figure 4.9, the variation of MSL and MLW with μ_{nr}, σ_{nr}, μ_{nn}, and σ_{nn} can be seen, especially when the sampling values of these variables are far apart. However, when the sampling values are close together, this trend can be seen to fluctuate. This is because the difference is too small to produce arrays with different performances.

One notable trend that can be seen from all plots is that the trends of MSL and MLW are always opposite, the lower the MSL, the higher the MLW and vice versa. This agrees with the findings the previous works and clearly shows that it is not possible to minimize MSL and MLW simultaneously. A good trade-off between these two performance parameters needs to be found.

Despite being visualized separately in Figure 4.9, the MSL and MLW are considered altogether in the optimization routine according to the objective function in Equation 4.7. Therefore, the objective function should be formulated such that it is a good representation of both MSL and MLW. This can be done by properly choosing MSL_{ref} and MLW_{ref}. Let the MLW_{ref} be fixed to 0.33 m which is the Rayleigh limit for this array at f_k = 1 kHz, the suitable value of MSL_{ref} is to be found.

The value of the objective function should ideally change both when the values of MSL and MLW change, i.e. it should be influenced by both parameters which are to be minimized. It should give a low value when a point which gives a good trade-off between MSL and MLW is obtained. For each pair of plots from Figure 4.9, plots showing the objective function (J_{main}) using MSL_{ref} = -1, -4, -9, and -13 dB are produced. An example of these plots from the combination of the first pair in Figure 4.9 (Figure 4.9a and 4.9b) is shown in Figure 4.10 which is basically the sensitivity of J_{main} wrt. μ_{nr}. It can be seen that for a high value of MSL_{ref} = -1 dB in Figure 4.10a, the trend of J_{main} main follows the average MSL in Figure 4.9a and hardly shows the trend of the average MLW from Figure 4.9b. Therefore, it is foreseeable that if this MSL_{ref} = -1 dB is used, the optimization will attempt to minimize the MSL and disregard the MLW. Likewise, for the lower values of MSL_{ref} = -9 and -13 dB in Figure 4.10c and 4.10d, the trend of J_{main} resembles to the trend of the average MLW from Figure 4.9b and hardly shows the influence of MSL from Figure 4.9a. It is also foreseeable that the opposite effect will occur in the optimization. Therefore, the value of MSL_{ref} is chosen to be -5 dB as shown in Figure 4.10b where the trend of the objective function is a good mixture between the average MSL and MLW from Figures 4.9a and 4.9b.

The mesh size factor (Δ_q) in the HJ/GPS algorithm determines how far apart from the current values of design variables the objective function is to be evaluated. This factor will start from (Δ_0) and will be reduced when there is no point where the objective function is lower than the current point is found. The optimization will terminate when the current mesh size factor is lower than Δ_{min}. The mesh size factor should be selected such that the correct trend of the objective function is seen in order to descend in the correct direction. If the mesh size factor is too small and the sampling of the objective function is done in a region where the fluctuation of the objective function is large, the algorithm could make an erroneous decision and descend in a wrong direction.

It can be observed from the plots shown so far in Figures 4.9 and 4.10 that the values of averaged MSL, MLW, J_{main} somewhat vary with changing μ_{nr}, σ_{nr}, μ_{nn}, and σ_{nn}. However, there also exists small fluctuations at the smallest step size of 0.025 m. Arrays generated by such small values of μ_{nr}, σ_{nr}, μ_{nn}, and σ_{nn} are not expected to have different performances and these fluctuations are the results of the randomness in the nested optimization loop. It is desirable that the optimization captures the *real* trend of the change in the objective function and ignores the small fluctuation. It can be seen that with a step $\geq$ 0.3 m, it is likely to see the change in the average MSL, MLW, and objective function, which are larger than the small fluctuations. Therefore, the initial mesh size factor (Δ_0) is set to be 0.3 m. As the step size gets closer to 0.025 m (higher sampling resolution), small fluctuations in the values of average MSL, MLW, and hence J_{main} can be seen and are likely to be taken by the optimization as the real trend. Therefore, if the optimization starts to use this small sampling step by having a low mesh size factor, the evaluated J_{main} will no longer provide a good indication of the objective function trend and the optimization algorithm is prone to descend in a wrong direction based on the inaccurate information. Hence it is motivated to terminate the optimization by setting Δ_{min} = 0.1 m where the objective function trend can still be seen with some acceptable fluctuation.

4.3. The Nested Optimization Loop

4.3.1. Optimization Problem Formulation

Given a set of μ_{nr}, σ_{nr}, μ_{nn}, and σ_{nn} from the main optimization loop, the nested optimization loop aims at generating a set of multi-arm spiral arrays that has the geometry as close as possible to the predefined geometry descriptor. The design variables for this optimization loop are used to define a multi-arm spiral array. The multi-arm spiral array is chosen to have 9 arms and 7 microphones per arm (including one more microphone at the array's centroid) as it has been found to achieve the best performance by Prime et al. (2014). The definition

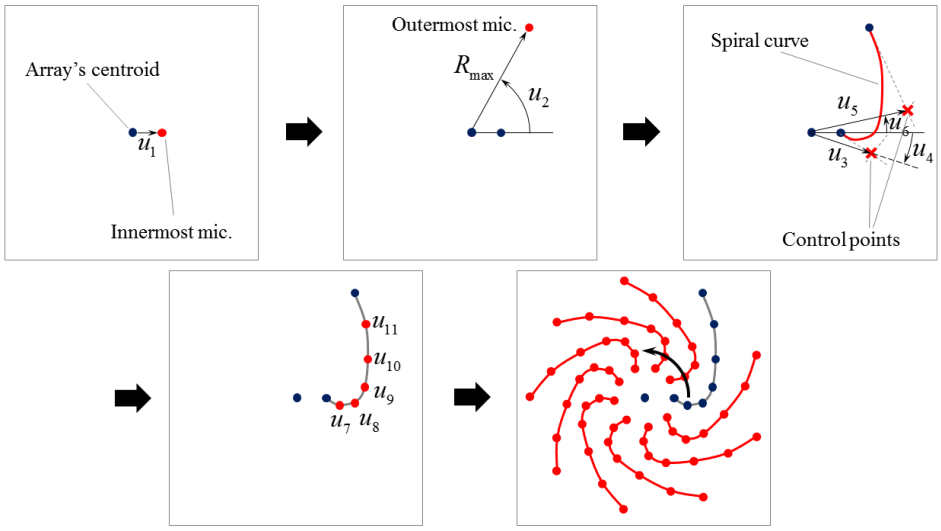

Figure 4.11: Generation of the multi-arm spiral arrays in the nested optimization loop

of a multi-arm spiral array does not require many design variables since once one spiral arm is defined, the remaining arms can be replicated by equidistant rotation of the first arm around the array's centroid. The design vector ($\mathbf{u}$) consists of 11 design variables (u_i) which are assigned as follows:

- u_1 describes the radial distance of the innermost microphone in the arm (the rotation angle of this microphone is not needed as the arm will anyway be replicated around the array's centroid)
- u_2 describes the rotation angle of the outermost microphone in the arm (the radial distance of the outermost microphone is fixed to R_{max})
- u_3 and u_5 describe the radial distance of the control points for generating the spiral arm's curve
- u_4 and u_6 describe the rotation angle of the control points for generating the spiral arm's curve
- u_7 to u_{11} describe the location of the five remaining microphones along the spiral arm's curve

A diagram showing the steps taken to generate a multi-arm spiral array is shown in Figure 4.11. The spiral arm's curve is defined by a Bezier curve starting from the innermost towards the outermost microphone. Let $t \in [0,1]$ be the number representing the location on the curve, the innermost and outermost microphones are at $t = 0$ and $t = 1$, respectively. The x and y locations of a microphone at any arbitrary t are

$$\mathrm{x}(t) = (1-t)^3\mathrm{x}_1 + 3t(1-t)^2\mathrm{x}_2 + 3t^2(1-t)\mathrm{x}_3 + t^3\mathrm{x}_4 \tag{4.10}$$

and

$$\mathrm{y}(t) = (1-t)^3\mathrm{y}_1 + 3t(1-t)^2\mathrm{y}_2 + 3t^2(1-t)\mathrm{y}_3 + t^3\mathrm{y}_4, \tag{4.11}$$

where the x and y coordinates are as shown in Figure 4.12.

Once a multi-arm spiral array has been generated, the geometric features of it are extracted to compare with the desired array geometry. A schematic diagram showing the extraction of the array's geometric features is shown in Figure 4.13. Let the radial distance on the array be divided into n_{bin} statistical bins, the actual number of all microphones in the b^{th} bin is N'_{r_b}. In addition, for the n^{th} microphone at the distance r_n m from the array's centroid, the actual distance to its nearest neighbor microphone is d'_{nn,r_n}. The objective is to minimize the total errors between the desired values of N_{r_b} and d_{nn,r_n} from Equation 4.1 and 4.5, respectively, and the actual values, N'_{r_b} and d'_{nn,r_n}. Accordingly, the objective function (J_{nested}) can be written as

$$J_{\text{nested}} = \frac{1}{n_{\text{bin}}} \sum_{b=1}^{n_{\text{bin}}} \frac{\left|N'_{r_b} - N_{r_b}\right|}{N_{r_b}} + \frac{1}{N} \sum_{n=1}^{N} \frac{\left|d'_{nn,r_n} - d_{nn,r_n}\right|}{d_{nn,r_n}}. \tag{4.12}$$

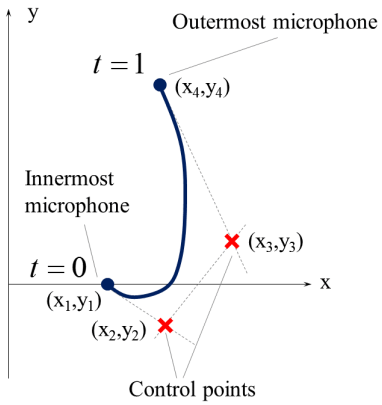

Figure 4.12: Definition of the spiral arm's curve by a Bezier curve

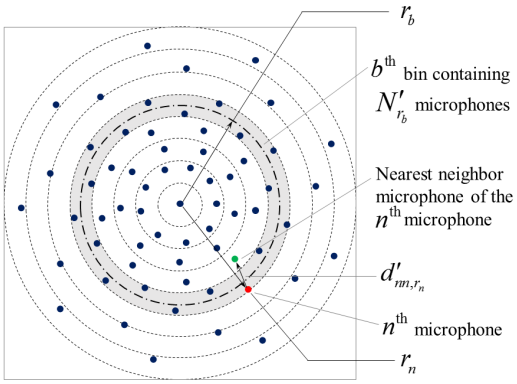

Figure 4.13: Extraction of the generated array's geometric features

Again, the normalization by N_{r_b} and d_{nn,r_n} ensures that the two errors having different units can be combined in one equation. Since the evaluation of d_{nn,r_n} needs to be done for all microphones while the N_{r_b} needs to be done only for all distance bins which is not as many as the number of microphones, the terms $1/n_{\text{bin}}$ and $1/N$ are added to ensure that the sum of d_{nn,r_n} errors does not overrule the sum of N_{r_b} errors.

4.3.2. The Optimization Algorithm

Since there is no a priori knowledge on the formulated objective function's convexity and differentiability and various designs are needed for the same set of μ_{nr}, σ_{nr}, μ_{nn}, and σ_{nn} to prove the design flexibility, an optimization algorithm which can handle this uncertainty and requirement is to be used.

The Differential Evolution (DE) algorithm was first introduced by Storn and Price (1997) and Storn (1996). Apart from acoustic array design (Malgoezar et al., 2016a), it has been used in various applications such as in beamforming (Malgoezar et al., 2016b) and geoacoustic inversion (Simons and Snellen, 1998).

The DE algorithm is a variant of the Genetic Algorithm (GA) which requires no a priori knowledge on the formulated problems and searches through the design space using a set of designs in each iteration. The algorithm consists of a randomized part which makes the process stochastic. This results in an extensive exploration of possible designs and a set of different solutions can be obtained.

In DE, multiple design vectors ($\mathbf{u}$) are treated simultaneously in the form of *population*. Let N_P be the *population size*, i.e. the number of $\mathbf{u}$ in the optimization. In each iteration, or the so-called *generation* lower than the maximum number of generations (N_G), the members of this population are improved to obtain a lower value of the objective function. Therefore any arbitrary design vector within any arbitrary generation can be written as $\mathbf{u}_{l,p}$ where $l = 1,2,\ldots,N_G$ and $p = 1,2,\ldots,N_P$.

In each generation (l), the *partner population* ($\mathbf{p}$ containing $p_{l,p}$) is generated from a random combination of the original population ($\mathbf{u}$) as

$$\mathbf{p}_{l,p} = \mathbf{u}_{l,r_1} + F(\mathbf{u}_{l,r_2} - \mathbf{u}_{l,r_3}), \tag{4.13}$$

where r_1, r_2, and r_3 are randomly chosen from $\{1,2,\ldots,N_P\}$. The *multiplication factor*, $F \geq 0$, indicates the difference between $\mathbf{p}_{l,p}$ and $\mathbf{u}_{l,p}$. In this case, F is chosen to be $F \in [0,1]$.

The *descendant*, $\mathbf{d}$ is the combination of $\mathbf{p}_{l,p}$ and $\mathbf{u}_{l,p}$ which results from the *crossover* operation;

$$d^j_{l,p} = \begin{cases} p^j_{l,p}, & [\mathrm{U}(0,1)]^j \leq p_c \\ u^j_{l,p}, & [\mathrm{U}(0,1)]^j > p_c \end{cases}, \tag{4.14}$$

where $d^j_{l,p}$, $p^j_{l,p}$, and $u^j_{l,j}$ represent the j^{th} component, i.e. a design variable, in the vectors $\mathbf{d}_{l,p}$, $\mathbf{p}_{l,p}$, and $\mathbf{x}_{l,j}$, respectively. The symbol $[\mathrm{U}(0,1)]_j$ represents the j^{th} randomized number in the uniform distribution between 0 and 1 and $p_c \in [0,1]$ is the *crossover probability*. This randomization process determines which value for a specific design variable the original and the partner population will become part of the descendant. The process is controlled by the value of p_c.

The population of the next generation ($\mathbf{u}_{l+1,p}$) is obtained by

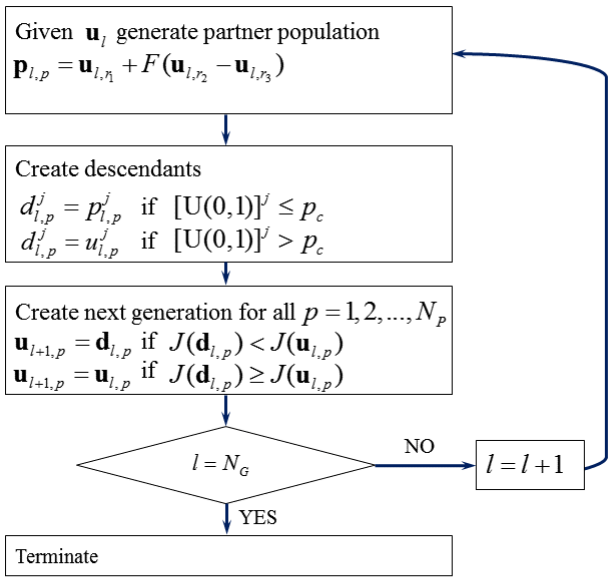

Figure 4.14: Flowchart of the DE algorithm

Table 4.1: Different combinations of μ_{nr}, σ_{nr}, μ_{nn}, and σ_{nn} used in the tests

	μ_{nr} [m]	σ_{nr} [m]	μ_{nn} [m]	σ_{nn} [m]
Combination 1	0.5	0.5	0.5	0.5
Combination 2	0.5	1	0.1	0.8
Combination 3	1	0.4	0.8	0.8

$$\mathbf{u}_{l+1,p} = \begin{cases} \mathbf{d}_{l,p}, & J_{\text{nested}}(\mathbf{d}_{l,p}) < J_{\text{nested}}(\mathbf{u}_{l,p}) \\ \mathbf{u}_{l,p}, & J_{\text{nested}}(\mathbf{d}_{l,p}) \ge J_{\text{nested}}(\mathbf{u}_{l,p}) \end{cases}, \tag{4.15}$$

which means that the p^{th} design vector in the population will be replaced by the p^{th} design vector in the descendant if $\mathbf{d}_{l,p}$ can produce a lower value of the objective function (J_{nested}). Otherwise, the original design vector will proceed to the next generation.

The optimization will repeat until l reaches N_G. At this final generation, one design vector in $\mathbf{x}_{N_G}$ which gives the lowest value of J_{nested} is found. A diagram showing the work-flow of the DE algorithm is shown in Figure 4.14.

4.3.3. Tuning and Testing the Optimization

As can be seen from the previous section, there are some parameters in the DE algorithm that can freely be chosen; namely, N_P, N_G, F, and p_c. From previous works (Malgoezar et al., 2016a,b, Simons and Snellen, 1998), it can be seen that the suitable values of these parameters can be different. It is a common practice to perform a deterministic study to determine the best combination of these optimization parameters before utilizing the algorithm. Therefore, for this particular application, the suitable values for N_P, N_G, F, and p_c are to be determined.

Following the framework of Malgoezar et al. (2016a), the value of N_G is set to be 4000 and three different values of N_P, 11, 16, and 22, are tested. The tested values for N_P are chosen based on the number of design variables, i.e. dimension of $\mathbf{u}_{l,p}$. Three different combinations of μ_{nr}, σ_{nr}, μ_{nn}, and σ_{nn} shown in Table 4.1 are tested. Therefore, there are nine test schemes in total. In these tests, the values of F and p_c are set to be 0.7 and 0.6, respectively, in accordance with Simons and Snellen (1998) and Malgoezar et al. (2016a).

For each test scheme, a Monte Carlo simulation was performed, in which ten independent optimization runs are executed. The averaged values of J_{nested} wrt. generation for different test schemes are shown in Figure 4.15. The dashed line in all plots shows the number of forward calculations $pl = 44000$. For the higher values of N_P, these lines are at the lower values of l due to the higher number of objective function evaluations needed for

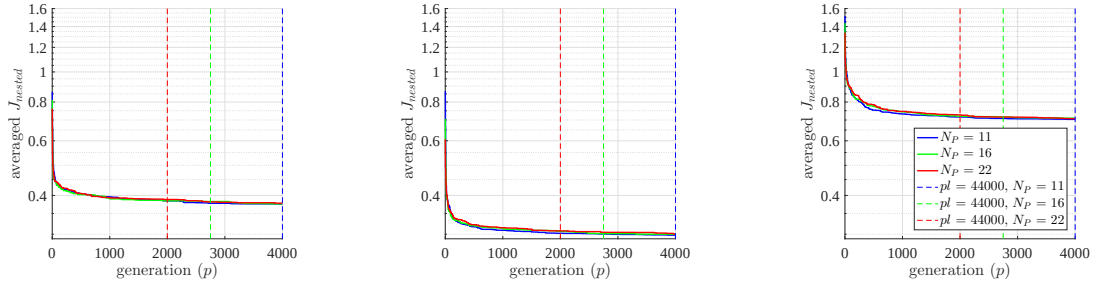

(a) Combination 1 (b) Combination 2 (c) Combination 3

Figure 4.15: Averaged J_{nested} wrt. generation (l) for different N_P and different combinations of μ_{nr}, σ_{nr}, μ_{nn}, and σ_{nn}

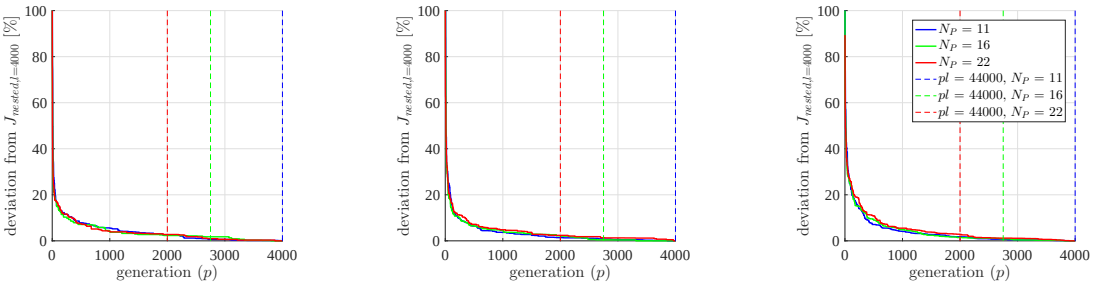

(a) Combination 1 (b) Combination 2 (c) Combination 3

Figure 4.16: Deviation (in percent) of averaged J_{nested} at each generation from J_{nested} at $l = 4000$ for different values of N_P and different combinations of μ_{nr}, σ_{nr}, μ_{nn}, and σ_{nn}

more individuals in the population. In addition, the deviations of the objective function value from the minimum objective function value as a function of generation are shown in Figure 4.16.

By comparing the values of J_{nested} for different values of N_P in Figure 4.15, it can be seen that the optimization cannot achieve notably lower values of J_{nested} although N_P is set to be twice as much. As the optimization progresses, the averaged J_{nested} for different N_P are similar at the same number of generations (l). Therefore, to save the computational effort, the value of N_P is chosen to be 11. The suitable value of N_G is determined by considering Figure 4.16. According to the plot, it is acceptable to terminate the optimization at $N_G = 500$.

As shown in Equations 4.13 and 4.14, the selection of F and p_c can control how much the partner design vectors. Using different combinations of $F \in \{0, 0.1, 0.2, \ldots, 1\}$ and $p_c \in \{0.2, 0.3, 0.4, \ldots, 1\}$, five independent optimization runs are performed. For every run, the values of N_P and N_G are fixed to be 11 and 500, respectively. In addition, the values of μ_{nr}, σ_{nr}, μ_{nn}, and σ_{nn} are chosen according to combination 1 in Table 4.1. A map showing the averaged values of J_{nested} for all possible combinations of F and p_c is shown in Figure 4.17. From the map, a region of low J_{nested} can be seen as a somewhat inter-connected region curving from $p_c = 0.4$ to 0.9 and $F = 0.2$ to 0.6, together with a small region at $p_c = 0.9$ and $F = 0.8$ to 0.9. It is decided that $F = 0.4$ and $p_c = 0.8$ are to be used further.

To visualize and examine the ability of the nested optimization loop to generate multi-arm spiral arrays close to the predefined sets of μ_{nr}, σ_{nr}, μ_{nn}, and σ_{nn}, three example acoustic arrays are generated using different combinations of μ_{nr}, σ_{nr}, μ_{nn}, and σ_{nn} from Table 4.1. The exemplary results are shown in Figure 4.18. It can be seen that the optimization attempts to fit the microphone arrangement to the array as close as possible to the predefined μ_{nr}, σ_{nr}, μ_{nn}, and σ_{nn}. For Figures 4.18a and 4.18b, it is relatively easy to place the microphones according to the desired geometric descriptions. The only challenge is that, for the microphones close to the array's edge, it is difficult to position each microphone sufficiently far apart since the density of microphones to be placed at that particular radial distance is high according to μ_{nr} and σ_{nr}. On the other hand, for the case in Figure 4.18c, it is more difficult to satisfy all geometry descriptors simultaneously since most of the microphones are to be placed close to the array's edge. This is also reflected in a higher value of averaged J_{nested} in Figure 4.15c than in Figures 4.15a and 4.15b. However, it can be seen that the optimization tries to find the best compromise of all requirements and the value of J_{nested} can indicate how well the generated array satisfy the predefined geometric descriptions.

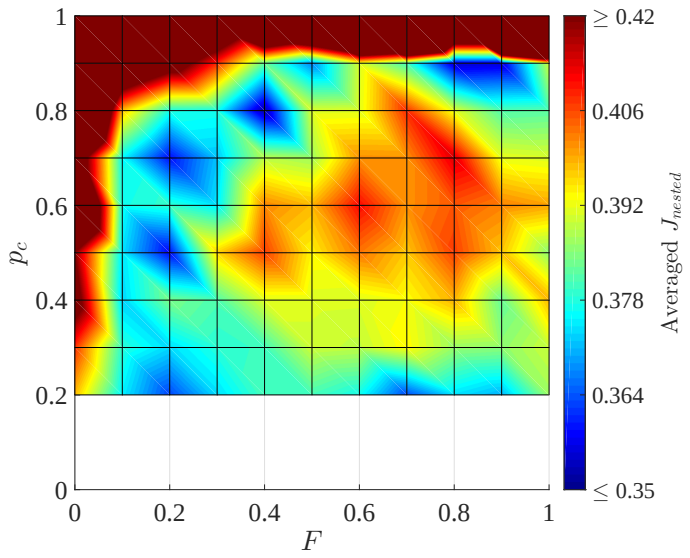

Figure 4.17: Map of averaged J_{nested} with varying F and p_c

The summary of the entire optimization process is shown in Table 4.2.

Table 4.2: Summary of the optimization architecture

	Main optimization loop	Nested optimization loop
Design variables	**X** containing the array's geometric feature descriptors; μ_{nr}, σ_{nr}, μ_{nn}, and σ_{nn}	**u** containing 11 design variables used for defining a multi-arm spiral array
Objective function	Equation 4.7 aims at minimizing MSL and MLW	Equation 4.12 aims at minimizing the errors between the array's actual and desired geometric features
Optimization algorithm	HJ/GPS	DE

4.4. Preliminary Investigation of the Design Space

The initial investigation is done to examine the design space and to check the feasibility of moving in the design space to arrive at an optimal array design. A test is done by generating multi-arm spiral arrays using the nested optimization loop. The values of μ_{nr}, σ_{nr}, μ_{nn}, and σ_{nn} are chosen from $\{0.1, 0.4, 0.7, 1\}$ m, resulting in $4^4 = 256$ combinations. For every combination, five arrays are generated.

A scatter plot showing the performance of all arrays in terms of average MSL and MLW (same plot as conceptually shown in Figure 4.1) is shown in Figure 4.19. The MSL and MLW of all designs considered are plotted. It can be seen that, most of the multi-arm spiral arrays generated can already achieve a lower value of average MSL than the Underbrink array. In comparison, the MSL and MLW of randomly-generated arrays with microphones arranged in a concentric manner having random numbers of circles, microphones per circle, and rotation angle of each circle are also shown in the plot. It can be observed that, in average, the randomly-generated concentric arrays cannot achieve as low MSL as the multi-arm spiral arrays with 9 arms and 7 microphones per arm. This finding confirms the result from (Prime et al., 2014) as shown in Figure 3.6. Moreover, the data also shows the trade-off between the MSL and MLW, the lower MSL an array can achieve, the higher MLW it is likely to produce and vice versa. However, there exists a region where designs which gives both lower MSL and MLW than the benchmarking Underbrink array. This implies that the design space to be explored covers the potential design.

Four plots from the same data set as in Figure 4.19 present the scatter plot with different colors according to the values of μ_{nr}, σ_{nr}, μ_{nn}, and σ_{nn} used in the generation of each particular arrays. It can be seen that the separation is obvious in the case of μ_{nr} and σ_{nr} in Figures 4.20a and 4.20b. For example, μ_{nr} which represents

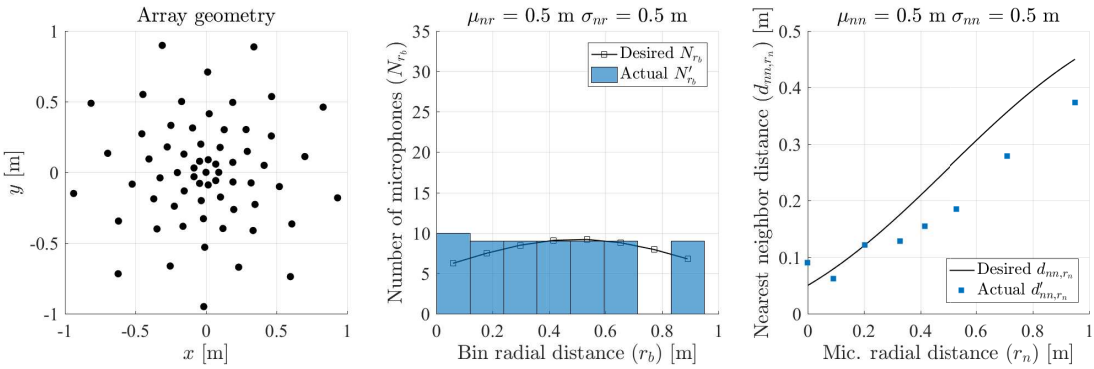

(a) Combination 1

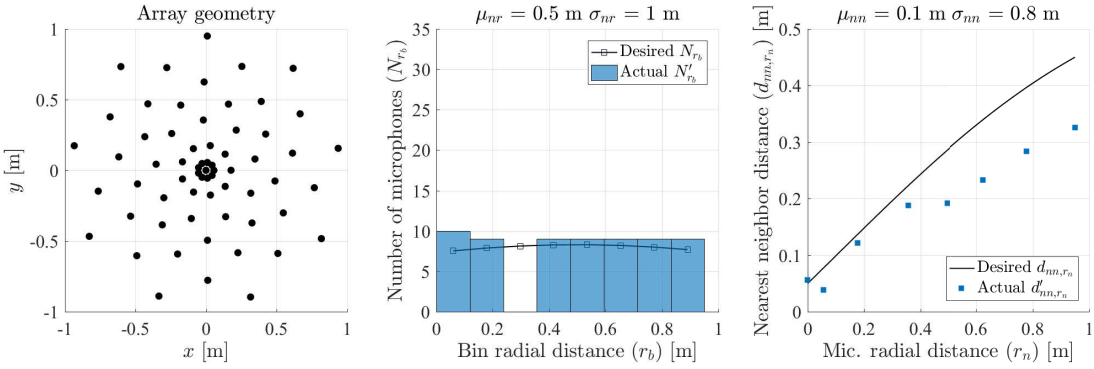

(b) Combination 2

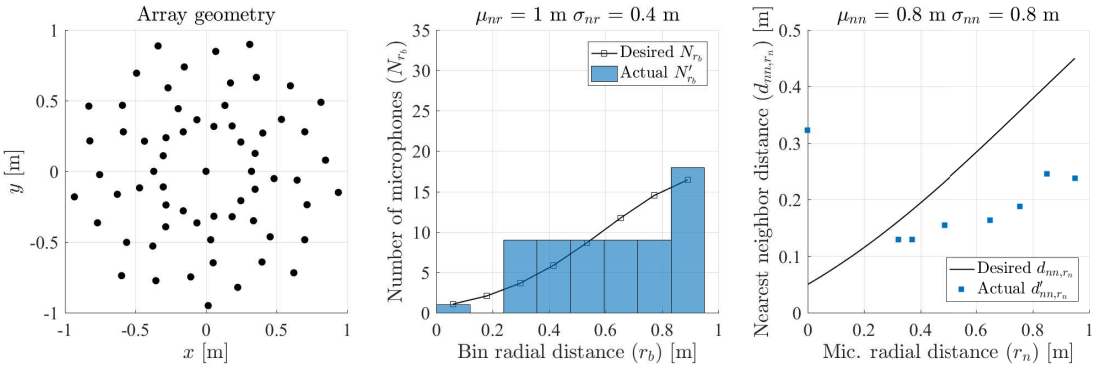

(c) Combination 3

Figure 4.18: Examples of the optimized arrays from the nested optimization loop using different combinations of μ_{nr}, σ_{nr}, μ_{nn}, and σ_{nn}

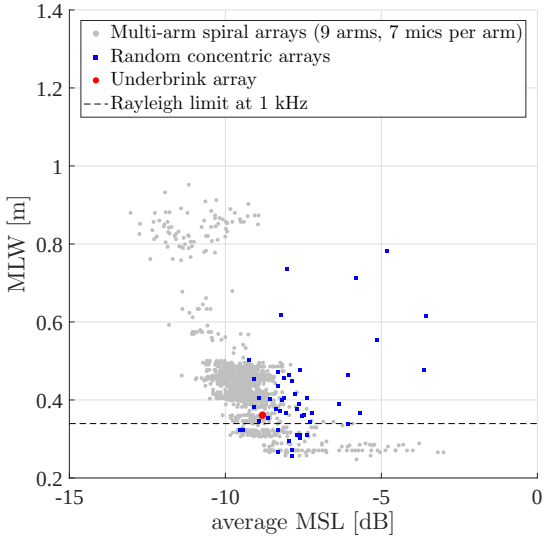

Figure 4.19: MSL and MLW of arrays generated in the possible range of μ_{nr}, σ_{nr}, μ_{nn}, and σ_{nn} compared with those of random concentric arrays and the Underbrink array

the center of microphone distribution wrt. the array's radial distance is related to the values of MLW. From these plots, it can already be anticipated that the optimal value of μ_{nr} should be close to 1 m and the optimal value of σ_{nr} should be close to 0.4 m. However, the separation of designs wrt. μ_{nn} and σ_{nn} as shown in Figures 4.20c and 4.20d cannot be seen as clearly as the first two variables and the optimal values of them cannot be anticipated from these plots.

Finally, a plot shown in Figure 4.21 is also generated from the same data set. The colors represent the values of the objective function (J_{main} in Equation 4.7) achieved by each design. It can be seen that the objective function is defined such that the region with the lowest value of J_{main} has both lower MSL and MLW than the Underbrink array. Therefore, if the objective function is able to arrive at that region, it can be ensured that the resulting design will improve the array's performance in both MSL and MLW as compared to the Underbrink array.

4.5. Variations of the Optimization Scheme

The optimization method discussed so far in this chapter will further be called the *general case*. The variations of the optimization schemes are to be made by altering some steps in the optimization as extra test cases to test the robustness of the proposed optimization method and to see the variations of the resulting optimized array geometries when additional conditions are imposed. The following optimization schemes will be made:

- Optimization with side lobe weighing: Side lobes are less desirable when they appear close to the main lobe in the source map as they are more likely to mislead the interpretation of the true sound source's acoustic behavior. This optimization scheme penalizes side lobes close to the main lobe by applying *weighing*. The weights are maximum when the side lobes are close to the scan plane's center, where the main lobe is in the simulation, and decrease linearly as the side lobes are further away from the main lobe. To implement this, the side lobe levels in the source map will be weighted according to their distances from the center of the scan plane before evaluating the MSL value. The MLW however will be evaluated from the original, i.e. without weighing, source map. An example visualizing the influence of weighing on the beampattern is shown in Figure 4.22. It is notable from the figure that only the beampattern at x = 0 m is at its original SPL while the side lobe levels are decreased due to the weighing factor < 1. Hence, it is possible to see the *weighted* MSL value lower than -17.6 dB, the minimum attainable non-weighted SPL.

- Optimization with multiple sources: Instead of one sound source, three sound sources will be placed in the scan plane in the beamforming simulation step. These sources will be arranged on a triangular and a linear line. The MSL will be evaluated as presented before and the MLW will be measured as the averaged value of MLW from all three sources at 1 kHz.

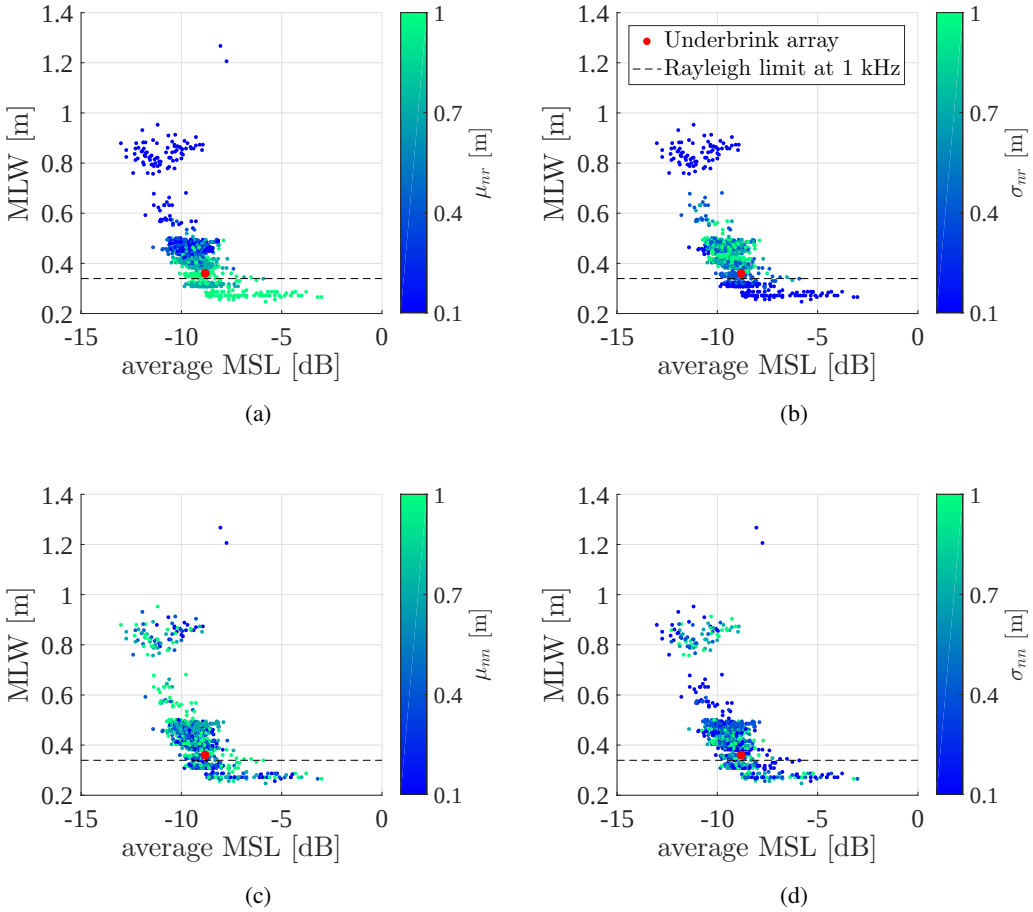

Figure 4.20: MSL and MLW of all array designs investigated in Figure 4.19 plotted with colored marker according to the values of μ_{nr}, σ_{nr}, μ_{nn}, and σ_{nn} used to generate each array

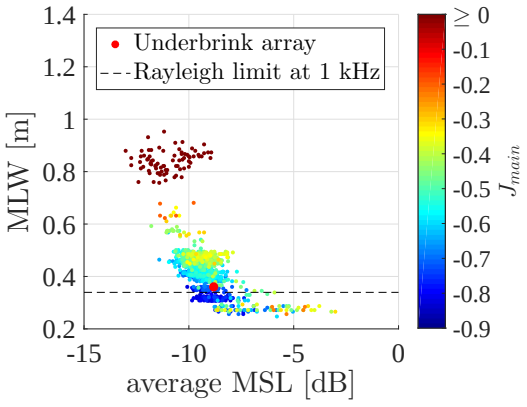

Figure 4.21: MSL and MLW of all array designs investigated in Figure 4.19 plotted with colored marker according to the values of J_{main} calculated as in Equation 4.7

- Optimization with a smaller array: The array size will be reduced to 1×1 m. This means that $R_{\max}$ will be changed to 0.5 m. The remaining steps will be kept the same.

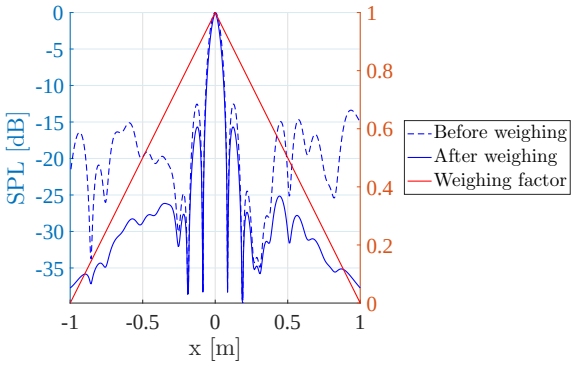

Figure 4.22: Influence of side lobes weighing on the beampattern

5

Optimization Results

5.1. Optimization Results: General Case

By following the optimization method presented in Chapter 4, five independent optimization runs are performed. The optimal set of μ_{nr}, σ_{nr}, μ_{nn}, and σ_{nn} are shown in Table 5.1 ranked according to the resulting objective function value (J_{main}). It can be seen that, for the first four out of five cases that give the lowest value of the objective function, the trend of the optimal μ_{nr}, σ_{nr}, μ_{nn}, and σ_{nn} are similar. The high values of μ_{nr} around 0.8 m indicate that the center of microphone distribution will be close to the array's edge with a low level of spreading according to σ_{nr} = 0.2 m. These values agree with the anticipation made by observing Figures 4.20a and 4.20b. The high values of μ_{nn} and the values of σ_{nn} mostly at 0.5 m indicate a gradual increase of the nearest neighbor inter-microphone distance as the microphone is further away from the array's center. Since the microphones are mostly close to the array's edge, a relatively large inter-microphone distance is expected.

Table 5.1: Optimization results (general case) from five independent optimization runs ranked by the objective function value

J_{main}	μ_{nr} [m]	σ_{nr} [m]	μ_{nn} [m]	σ_{nn} [m]
-0.953	0.8	0.2	0.93	0.5
-0.920	0.97	0.2	0.8	0.5
-0.912	0.8	0.2	1.0	0.5
-0.906	0.83	0.2	0.8	0.5
-0.877	0.8	0.1	0.5	0.28

A scatter plot showing the MSL and MLW of all designs evaluated in the optimization case which gives the lowest J_{main} (the first row of Table 5.1) with the emphasis on the arrays generated at the initial design point, the arrays generated at the optimal design point, and the benchmarking Underbrink array is shown in Figure 5.1. The arrows indicate the selected arrays to represent the initial designs and the optimal designs which will be investigated further. These arrays are shown in Figure 5.2. Plots showing the MSL and MLW of these arrays wrt. frequency taken from the beamforming simulation in the optimization are shown in Figure 5.3 and 5.4. The source maps of these arrays at 4 kHz are shown in Figure 5.5.

From the optimal array in Figure 5.2b, it can be observed that most of the microphones are placed close to the array's edge, with the innermost microphone at around 0.4 m from the array's center. The inter-microphone distances are mostly constant. Figures 5.3 and 5.4 show that the optimized array can achieve, in average, lower MSL and MLW values than the initial and the Underbrink array. According to the plot, the MSL of the selected optimized array is around 1.2 dB lower than the Underbrink array, in average from 4 to 10 kHz. The value of the MLW at 1 kHz is about 5 cm lower than the Underbrink array. This is confirmed by the beampattern comparison shown in Figure 5.5. It can be seen that the MLW values of this optimized array and many other arrays in the optimization history are lower than the Rayleigh limit. This is because the MLW measured in the optimization at -3 dB is lower than the actual MLW as explained in Section 2.3. Despite the low value of MLW, by observing the beampattern of the optimized array, there exist a ring of small side lobe close to the main lobe. The existence of this ring may make this part of the beampattern similar to the ideal pattern from an array with infinite number of microphone shown in Figure 2.3a where the MSL is the first side lobe close to the main lobe and the MLW is at the lowest possible value. The optimization scheme with weighted side lobes according to their distances from

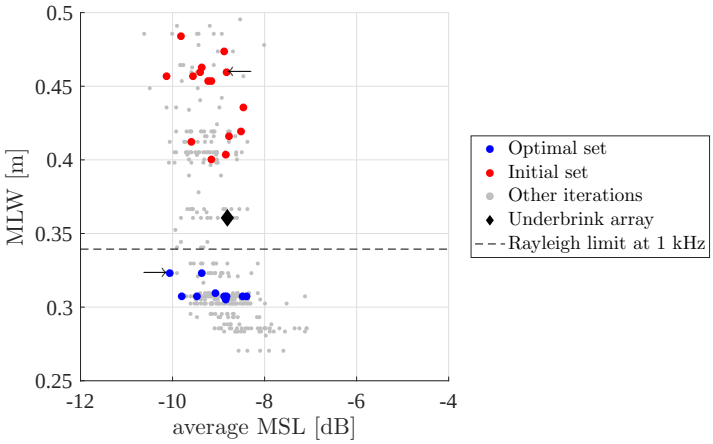

Figure 5.1: MSL and MLW of all arrays considered in the optimization (general case) including the Underbrink array, the arrows show the selected array representing the arrays in the initial and the optimal set

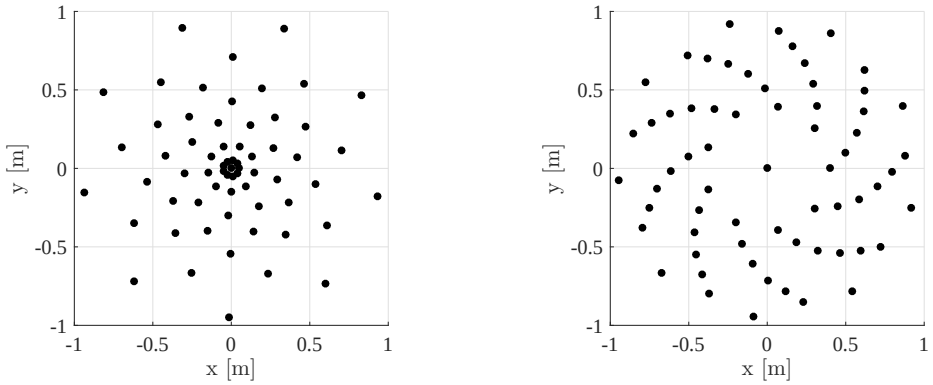

(a) Initial array (b) Optimized array

Figure 5.2: Arrays taken from the optimization history (pointed by arrows in Figure 5.1)

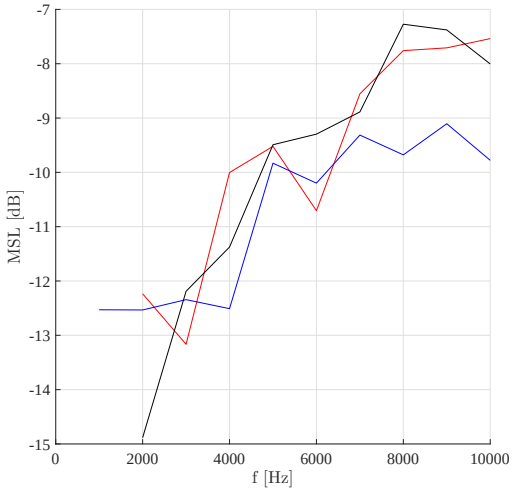

Figure 5.3: MSL of the arrays from Figure 5.2

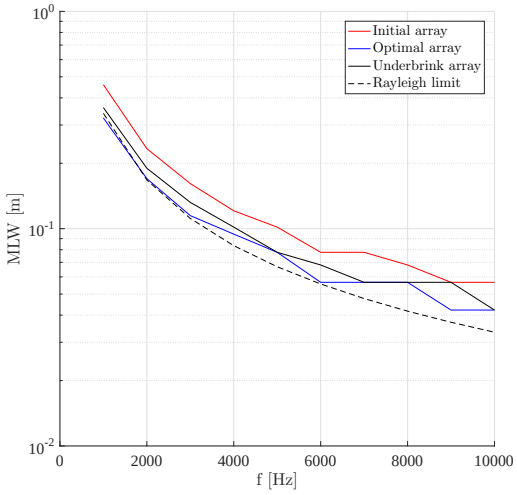

Figure 5.4: MLW of the arrays from Figure 5.2

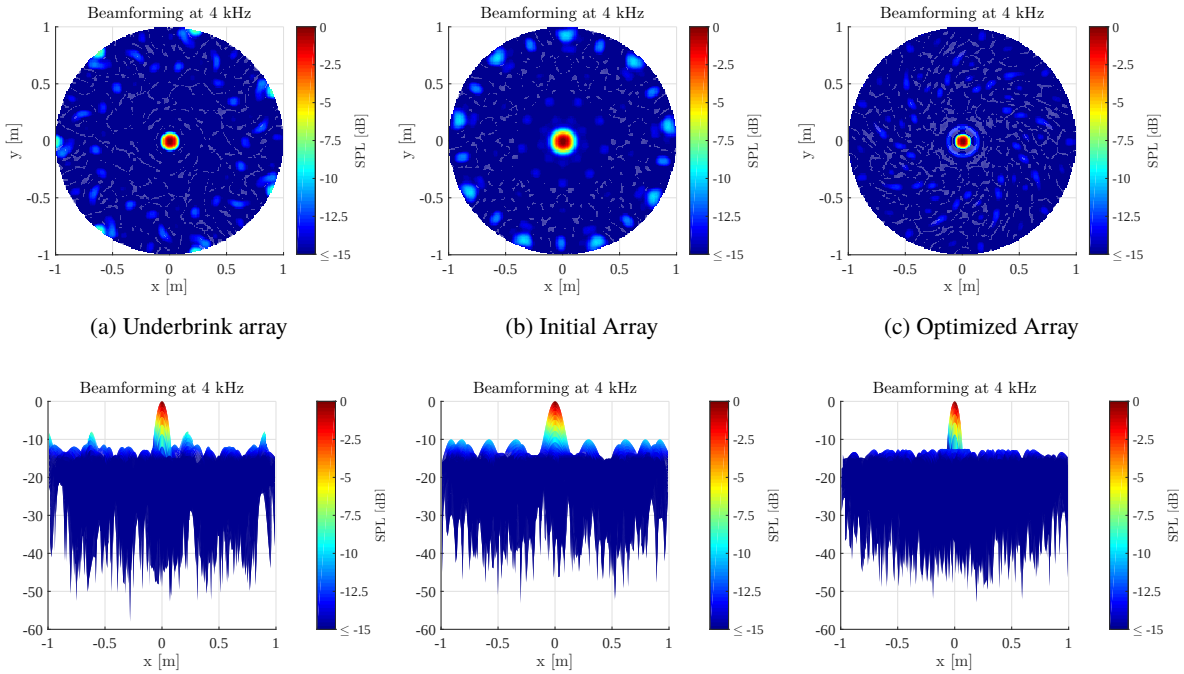

(a) Underbrink array (b) Initial Array (c) Optimized Array

(d) Underbrink array (e) Initial array (f) Optimized array

Figure 5.5: Top and side views of the source maps produced by beamforming at 4 kHz using the arrays from Figure 5.2

the main lobe may force this side lobe to disappear. The result from this variation in the optimization method together with the results from the other variations are discussed in the next Section.

5.2. Optimization Results from Other Optimization Schemes

5.2.1. Optimization with Side Lobes Weighing

This section presents the results from the optimization case with side lobes weighted according to their distances from the main lobe. The optimal values of μ_{nr}, σ_{nr}, μ_{nn}, and σ_{nn} are shown in Table 5.2 ranked according to the resulting objective function value (J_{main}). The trend of the optimal values are different from the optimization case presented in Section 5.1. The values of μ_{nr} are, in average lower and the values of σ_{nr} are higher than the case in Section 5.1. This indicates that the optimal arrays will have the center of microphone distribution closer to the array's centroid and the microphones are more widely distributed wrt. the array's radial distance. The low values of μ_{nn} imply that the inflection point of the nearest-neighbor distance to the nearest microphone is at the radial distance close to the array's centroid. That means most microphones on the array will have a relatively high nearest-neighbor distance to the nearest microphone. Further results from the first row of Table 5.2 is shown from Figure 5.6 to Figure 5.10 in the same manner as the previous section.

Table 5.2: Optimization results (side lobe weighing case) from five independent optimization runs ranked by the objective function value

J_{main}	μ_{nr} [m]	σ_{nr} [m]	μ_{nn} [m]	σ_{nn} [m]
-1.209	0.8	0.33	0.1	0.5
-1.203	0.8	0.33	0.33	0.2
-1.183	0.5	0.33	0.37	0.5
-1.148	0.5	0.2	0.2	0.5
-1.124	0.5	0.2	0.5	0.2

The microphone distribution of the optimal array shown in Figure 5.7b agrees with the optimal geometry descriptors shown and discussed previously. The microphones are distributed more evenly over the array's radial distance than the optimal array in Figure 5.2b. Apart from that, by comparing Figure 5.6 with Figure 5.1, it can be seen that the MLW of the set of arrays generated by the optimal values of μ_{nr}, σ_{nr}, μ_{nn}, and σ_{nn} lies above the Rayleigh limit in case of the optimization with weighted side lobes instead of below the Rayleigh limit as in

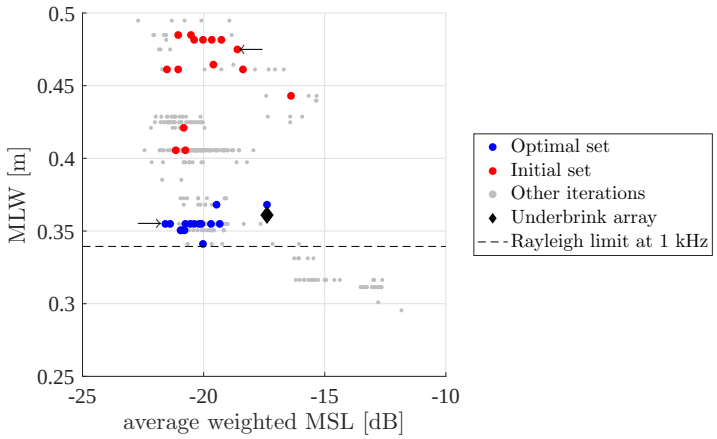

Figure 5.6: MSL and MLW of all arrays considered in the optimization (side lobes weighing case) including the Underbrink array, the arrows show the selected array representing the arrays in the initial and the optimal set

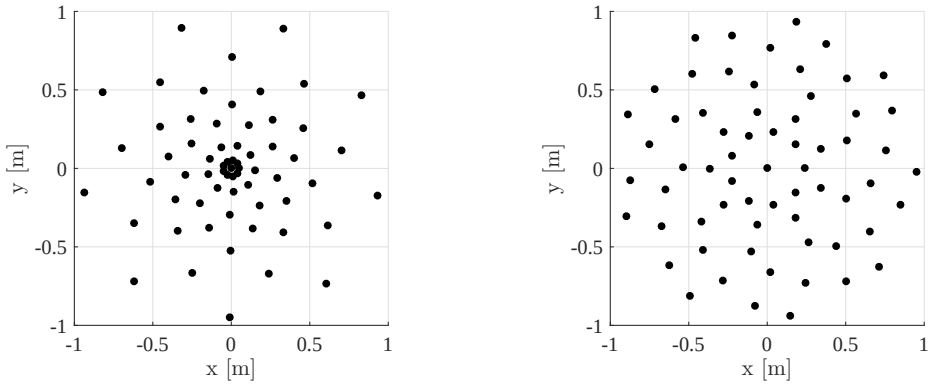

(a) Initial array (b) Optimized array

Figure 5.7: Arrays taken from the optimization history (pointed by arrows in Figure 5.6)

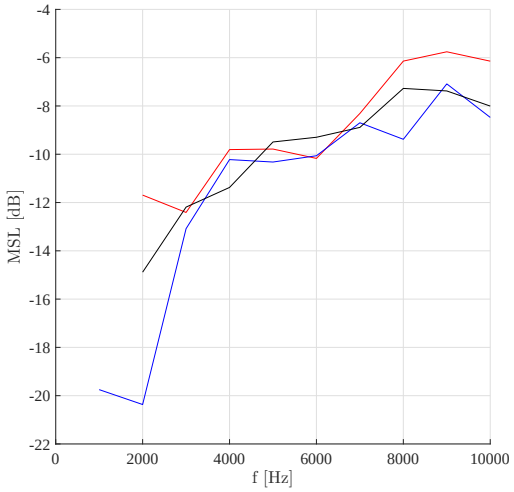

Figure 5.8: MSL of the arrays from Figure 5.7

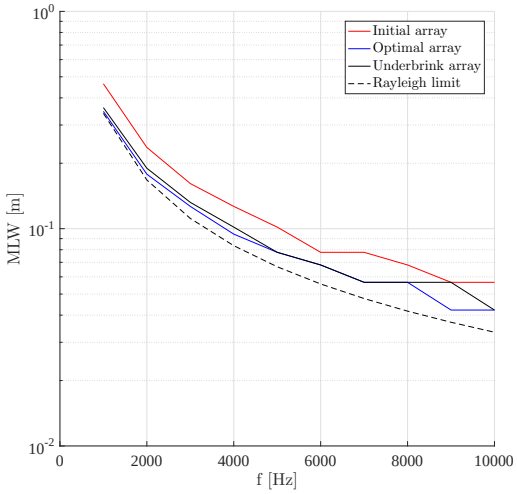

Figure 5.9: MLW of the arrays from Figure 5.7

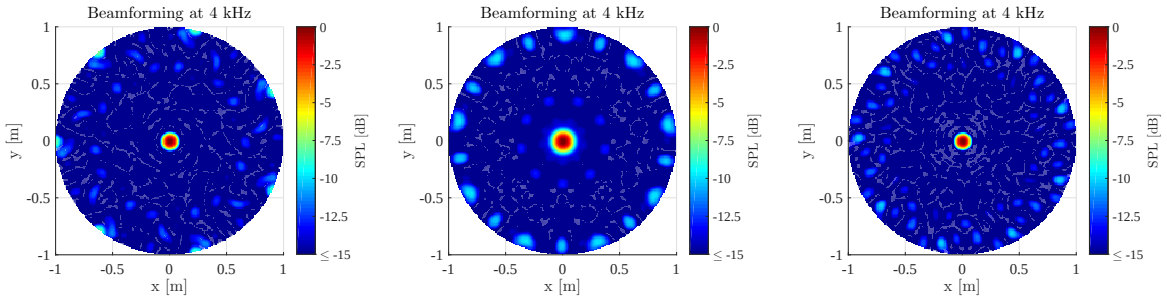

(a) Underbrink array (b) Initial array (c) Optimized array

Figure 5.10: Source maps produced by beamforming at 4 kHz using the arrays in Figure 5.7

the previous case. However, the MLW of most arrays in the optimal set are still slightly lower than that of the Underbrink array. For example, the MLW of the selected array at 1 kHz is 1.4 cm lower than the Underbrink array. This is comfirmed by the plots in Figure 5.9. The performance in terms of MSL of the optimized array in this case is however not as observably lower than the initial and Underbrink array as in the previous optimization case. The average reduction of MSL from the selected optimized array is around 0.36 dB from the Underbrink array calculated at 4 to 10 kHz. It is also notable that the average weighted MSL values in Figure 5.6 are lower than -17.6 dB which is the theoretically minimum MSL as a result of weighing discussed in Section 4.5. However, the non-weighted MSL values of the optimized array in Figure 5.8 are also lower than -17.6 dB at low frequencies. This is because at low frequencies, the main lobe is large and covers most of the scan plane area. As a results, the side lobes are at the region beyond the scan plane's boundary. By considering the beampattern in Figure 5.10c, it can clearly be seen that the low side lobe ring is no longer present next to the main lobe due to the influence of weighing. There exists a large area around the main lobe where the side lobe levels are lower than -15 dB. The trade-off made for this is the lower reduction of MSL and MLW from the Underbrink array compared to those from the general optimization case.

5.2.2. Optimization with Three Sources

Optimization with Three Sources Arranged in a Triangular Manner

This section presents the results from the optimization case with three sound sources present in the beamforming evaluation step of the optimization. In this case, the sound sources are arranged in a triangular shape with the distance between each source of 80 cm. The optimal values of μ_{nr}, σ_{nr}, μ_{nn}, and σ_{nn} are shown in Table 5.3 ranked according to the resulting objective function value (J_{main}). The trend of μ_{nr} and σ_{nr} is similar to the optimization results presented in Table 5.1. Therefore, an array with high microphone density close to the array's edge is expected. However, the clear trend of the optimal μ_{nn} and σ_{nn} cannot clearly be seen. Again, further results from the first row of Table 5.3 is shown from Figure 5.11 to Figure 5.15 in the same manner as the previous sections.

Table 5.3: Optimization results (three sources, triangular case) from five independent optimization runs ranked by the objective function value

J_{main}	μ_{nr} [m]	σ_{nr} [m]	μ_{nn} [m]	σ_{nn} [m]
0.096	0.93	0.2	0.23	0.5
0.103	1.0	0.2	0.73	0.2
0.104	0.97	0.22	0.2	0.5
0.112	0.84	0.2	0.5	0.5
0.139	0.8	0.2	0.5	0.5

The trend of the optimal design variables, together with the optimal array shape, and the source maps are similar to the results from the general optimization case. According to Figures 5.13 and 5.14, when three sources are simulated on the scan plane, the MSL value of the optimized array is around 0.3 dB lower than the Underbrink array in average from 4 to 10 kHz. This array also gives the average MLW of all sources around 10 cm lower than the Underbrink array at 1 kHz. The small side lobe ring close to the main lobe is still present in the source map produced by the optimized array as shown in Figure 5.15c.

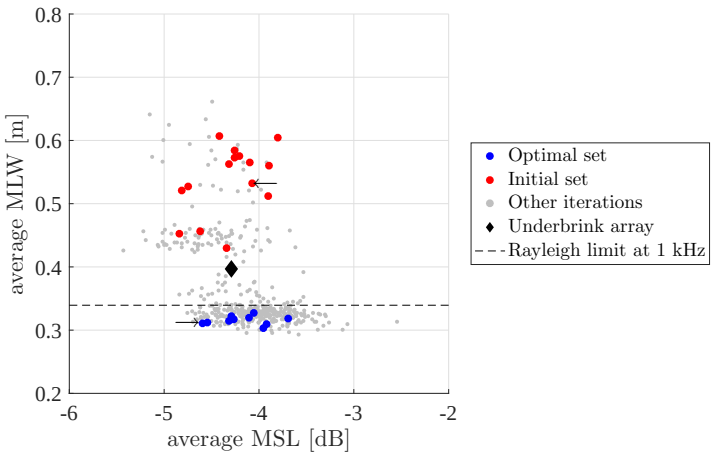

Figure 5.11: MSL and MLW of all arrays considered in the optimization (three sources, triangular case) including the Underbrink array, the arrows show the selected array representing the arrays in the initial and the optimal set

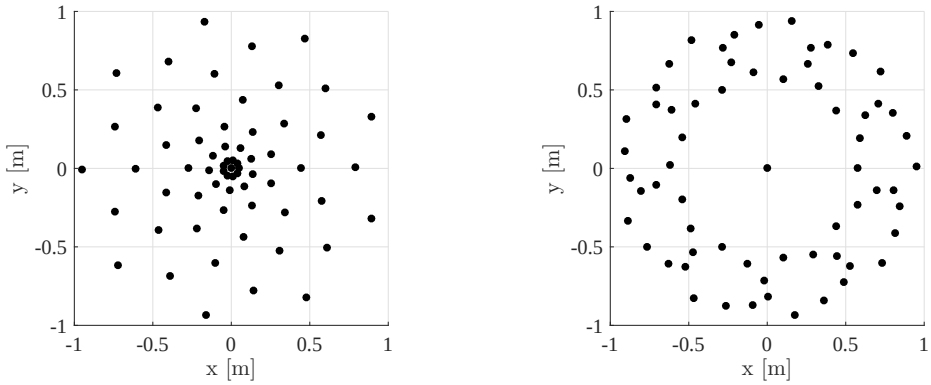

(a) Initial array (b) Optimized array

Figure 5.12: Arrays taken from the optimization history (pointed by arrows in Figure 5.11)

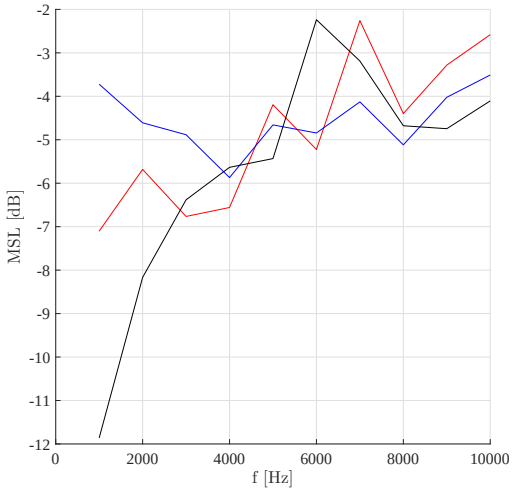

Figure 5.13: MSL of the arrays from Figure 5.12

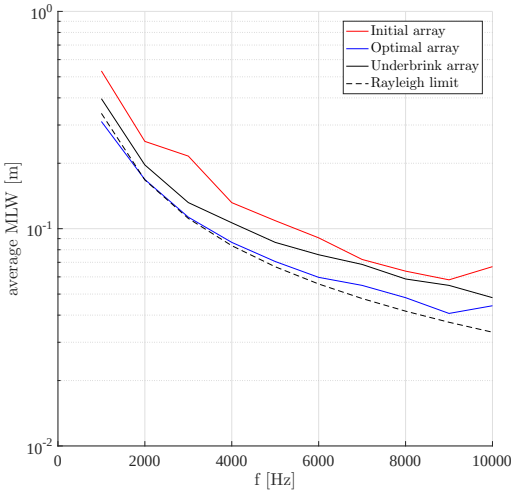

Figure 5.14: MLW of the arrays from Figure 5.12

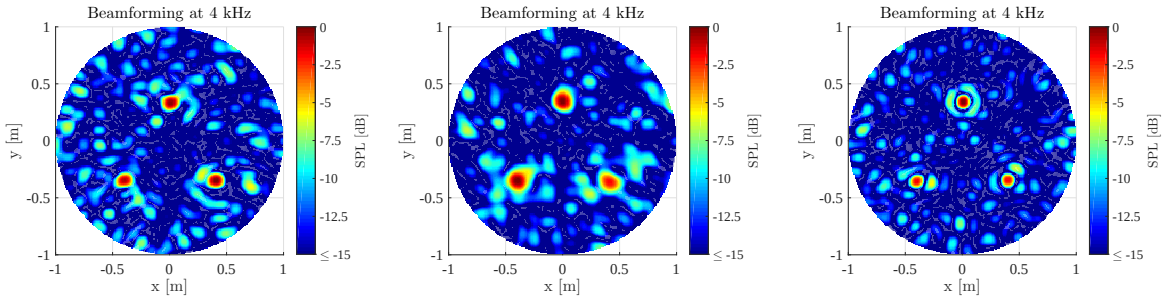

(a) Underbrink array (b) Initial array (c) Optimized array

Figure 5.15: Source maps produced by beamforming at 4 kHz using the arrays in Figure 5.12

Optimization with Three Sources Arranged in a Linear Manner

This section presents the results from the optimization case with three sound sources present in the beamforming evaluation step of the optimization. In this case, the sound sources are arranged in a linear manner with the distance between each source of 75 cm. The optimal values of μ_{nr}, σ_{nr}, μ_{nn}, and σ_{nn} are shown in Table 5.4 ranked according to the resulting objective function value (J_{main}). It is notable that the trend of μ_{nr} and σ_{nr} is completely opposite to the cases presented in Table 5.1 and 5.3. The low values of σ_{nr} imply that the microphones will be distributed close to the array's center in the optimal array. A further observation can be made that the values of J_{main} in Table 5.4 are notably lower than those in Table 5.3 although they are derived from the MSL and MLW in the beamforming simulation in the same manner as in the previous case.

Table 5.4: Optimization results (three sources, linear case) from five independent optimization runs ranked by the objective function value

J_{main}	μ_{nr} [m]	σ_{nr} [m]	μ_{nn} [m]	σ_{nn} [m]
-0.652	0.28	0.5	0.73	0.5
-0.640	0.2	0.5	0.5	0.2
-0.631	0.2	0.5	0.5	0.2
-0.631	0.2	0.2	0.5	0.2
-0.616	0.5	0.5	0.63	0.37

A scatter plot showing the MSL and MLW of the arrays evaluated in the optimization is shown in Figure 5.16 in the same format as shown in the previous sections. It is notable that the values of averaged MLW from the investigated arrays in this case are low compared with that of the Underbrink array. Since these values represent the average MLW of three sources at 1 kHz, the simulated source maps of the Underbrink array, the initial array, and the optimized array are examined.

From the source maps in Figure 5.17, it can be seen that the main lobe representing the source in the middle is relatively smaller than the remaining two main lobes in the source map produced by the initial and the optimized arrays due to the interference. Since the MLW is averaged from all main lobes, the average values of MLW appear to be unrealistically low when there is one out of three main lobe which gives a very low value of MLW. Therefore, this could mislead the optimization and suggests one limitation of modifying the beamforming simulation in the optimization. It is decided that the results from this case will not be considered in further investigations.

5.2.3. Optimization with a Smaller Array Size

This section presents the results from the optimization case with a smaller array size. The array's maximum radial distance for placing a microphone is 0.5 m from the array's centroid instead of 0.95 m. The resulting optimal values of μ_{nr}, σ_{nr}, μ_{nn}, and σ_{nn} are shown in Table 5.5 ranked according to the resulting objective function value (J_{main}). The optimal values of μ_{nr} are identical (0.5 m) for all independent runs. This means that the center of microphone distribution wrt. array's radial distance at 0.5 m and therefore implies that most microphones will be placed close to the array's maximum radial distance limit. The values of σ_{nr} are also quite similar at around 0.2 m for all independent runs. However, the similarity in the optimal values of μ_{nn} and σ_{nn} can hardly be seen. As in previous sections, the results from the first row of Table 5.5 are investigated in Figures 5.18 to 5.22.

From Figure 5.18, it can be seen that the optimized set of array has, in average, worse performance in terms of MSL compared to the initial set. However, this is a trade-off for having a lower MLW. Overall, the performance

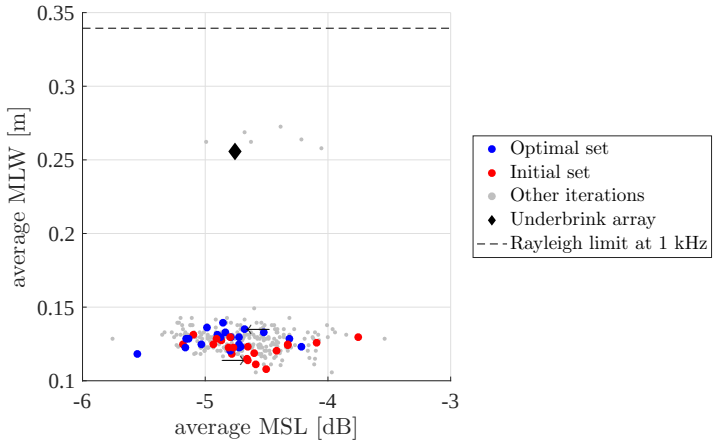

Figure 5.16: MSL and MLW of all arrays considered in the optimization (three sources, linear case) including the Underbrink array, the arrows show the selected array representing the arrays in the initial and the optimal set

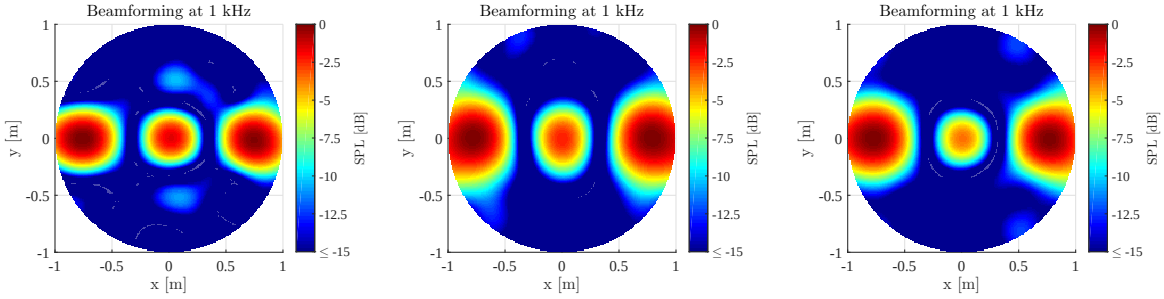

(a) Underbrink array (b) Initial array (c) Optimized array

Figure 5.17: Source maps produced by beamforming at 1 kHz using the arrays from the optimization case with three sources arranged in a linear manner

Table 5.5: Optimization results (small scale case) from five independent optimization runs ranked by the objective function value

J_{main}	μ_{nr} [m]	σ_{nr} [m]	μ_{nn} [m]	σ_{nn} [m]
-0.392	0.5	0.17	0.17	0.3
-0.384	0.5	0.28	0.05	0.05
-0.359	0.5	0.22	0.05	0.3
-0.352	0.5	0.22	0.3	0.5
-0.270	0.5	0.13	0.5	0.08

of the selected optimal array is still better than the Underbrink array both in terms of MSL and MLW. It is also notable that most arrays evaluated in this optimization scheme have the MSL values approximately between -12 and -10 dB while the arrays evaluated in the optimization with a larger array diameter in Figure 5.1 have the higher MSL values approximately between -10 and -8 dB. This confirms with the theory presented in Section 2.4.2 that the more microphones clustered close to the array's centroid, the better the beamforming performance in terms of MSL.

By observing the optimal array's geometry in Figure 5.19c, it can be seen that the nearest-neighbor microphone distance does not increase as the microphone is further away from the array's center. Instead, there exist two regions of dense microphone distribution; the inner circle and the region close to the array's edge. The effect of having relatively high number of microphones close to the arrays edge is the 10 cm reduction of MLW compared with the Underbrink array at 1 kHz as shown in Figure 5.21. On the other hand, the performance in terms of MSL of the optimized array outperforms the initial and the Underbrink array only at high frequencies according to Figure 5.20. At low frequencies, including at 4 kHz where the simulated source maps are shown in Figure 5.22. The Optimized array has the highest and observable side lobe, compared to the remaining two arrays.

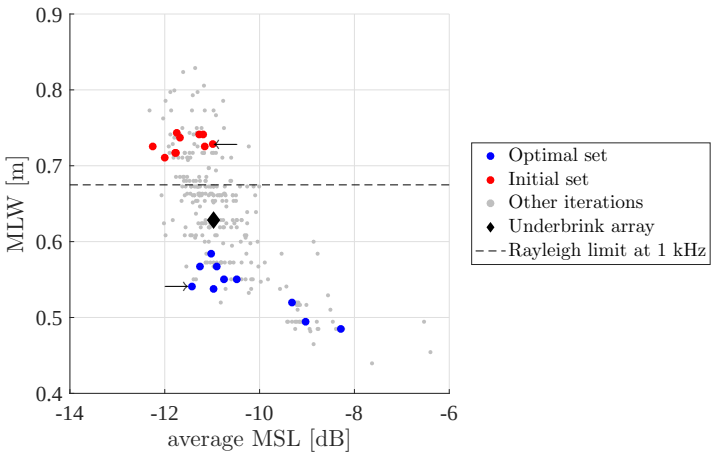

Figure 5.18: MSL and MLW of all arrays considered in the optimization (small array case) including the Underbrink array, the arrows show the selected array representing the arrays in the initial and the optimal set

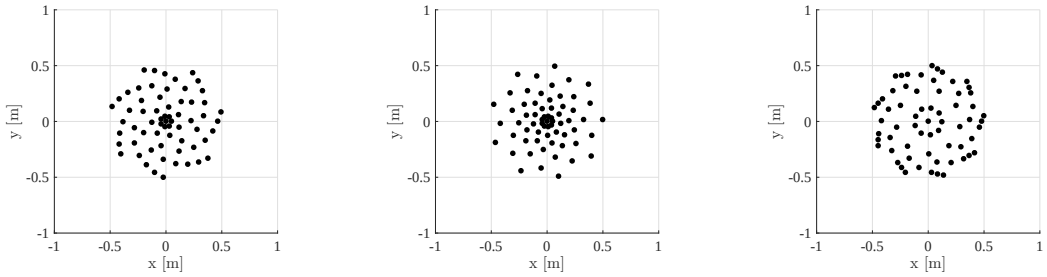

(a) Underbrink array (b) Initial array (c) Optimized array

Figure 5.19: Arrays taken from the optimization history (pointed by arrows in Figure 5.18)

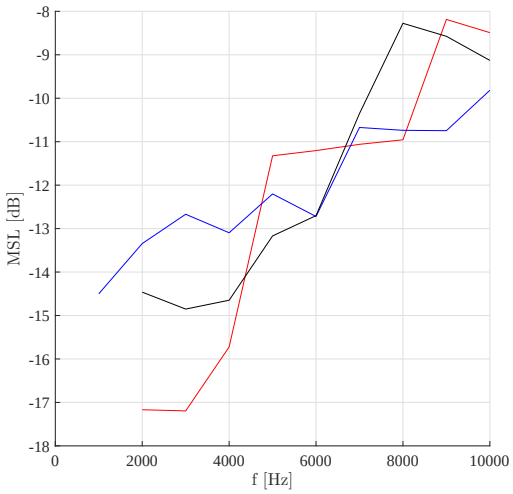

Figure 5.20: MSL of the arrays from Figure 5.19

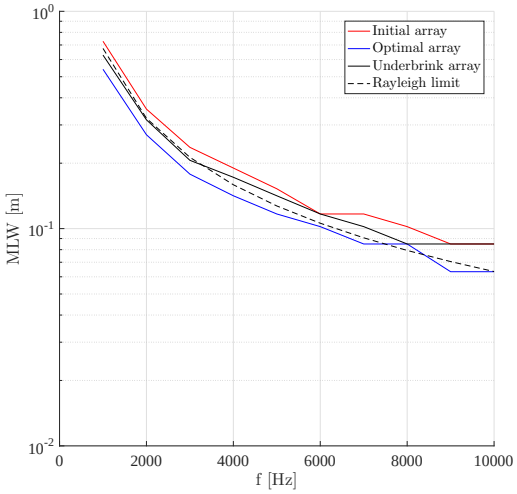

Figure 5.21: MLW of the arrays from Figure 5.19

5.3. Further Investigation of Optimized Arrays Performance

5.3.1. Multiple Sources and Line Source

The sound sources in aero-acoustic experiments will rarely be an ideal single point source as used in the optimization. Instead, there can be multiple sources present in the scan plane. Moreover, the sound sources could

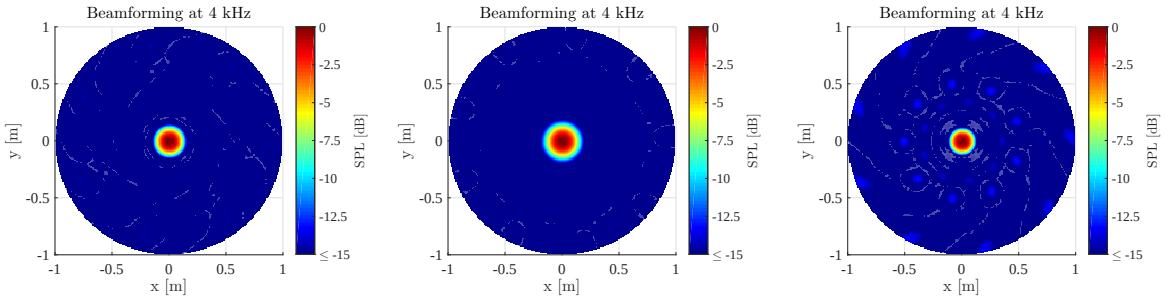

(a) Underbrink array (b) Initial array (c) Optimized array

Figure 5.22: Source maps produced by beamforming at 4 kHz using the arrays in Figure 5.19

also be a line source such as in trailing edge noise measurement of an airfoil. These have been implemented in some optimization cases where multiple sound sources are simulated in array's beamforming performance evaluation. In this section, beamforming simulations with these variations in source arrangements are performed using the optimized array obtained from all different optimization cases. The simulations are done as follows:

- Multiple sources: Three incoherent white noise sources are simulated at the distance of 1.5 m away from the array. The sources are arranged in a triangular manner with the separation distance of 35 cm.
- Line sources: 51 incoherent noise sources are densely placed in a linear line with the length of 60 cm at the distance of 1.5 m away from the array.

Figure 5.23 shows the source maps obtained from the aforementioned beamforming simulations using the Underbrink array, the initial array[1], the general case optimized array, the side lobes weighted optimized array, and the three-source optimized array. To emphasize the differences, the SPL values below -15 dB are omitted. The first column repeats the simulation result with one sound source at 4 kHz. The second and the third column present the source maps from beamforming of multiple and line sources at 3 kHz, respectively.

For the case with a single sound source, most of the simulated source maps have relatively low side lobe levels compared with the multiple and line source cases. The MLWs from all optimization cases are observably lower than the initial case. It is notable that for the general optimization case and the optimization case with three sound sources, there exists a small side lobe ring close to the main lobe. However, this ring of side lobe is not present in the optimization case with weighted side lobe. As a result, the main lobe width of this case is slightly wider than the case where the side lobe ring presents, but still slightly lower than that of the Underbrink array.

For the cases with multiple and line sources, the source maps still follow the same trend as the single source case. The MLW in the single source case can imply how wide the main lobes in the multiple source case will be. The pattern of side lobes is also observable in this case but at a higher level relative to the main lobe compared with the single source case. The arrays which produce a small ring of side lobes close to the main lobe suffer from having side lobes close to the source and this could make the boundary of the sources unclear. These small side lobes are also observable in the source maps produced by the Underbrink array in the multiple and line source cases. In this case, the optimized array with weighted side lobes is the only array that can still maintain low MLW and a clean area with side lobe levels lower than -15 dB up to the distance of approximately four times the MLW around the main lobes. Therefore, it can be concluded that the optimized array with weighted side lobe is the most suitable array among all considered arrays for practical applications in the V-tunnel.

The aforementioned findings can also reflect back to the optimization method. The use of one sound source in the beamforming simulation for evaluating MSL and MLW is sufficient to imply the array's performance in the different cases of source arrangement. However, attempting to minimize MSL and MLW simultaneously can force the optimization to produce an array which attempts to creates a small side lobe to reduce the main lobe width in the source map. These arrays can appear to have quantitatively good MSL and MLW but they are not suitable for practical usages. The findings suggest that one way to produce an optimal array which is suitable for real applications, is to impose weighing of side lobes according to their distances from the main lobe in the optimization.

[1]The initial array is taken from the representative initial array shown in Figure 5.7a. However, it can represent the initial array for all optimization cases as they are generated by the same initial set of μ_{nr}, σ_{nr}, μ_{nn}, and σ_{nn}

5.3.2. Array Scaling

Another remaining optimization case is the optimization with a smaller array size (1×1 m). The investigation of this array's performance has been presented in Section 5.2.3. Since most of the benchmark arrays are designed to be flexible for different array sizes, preliminary investigation of the selected optimal array's in a different scale is presented in this section to assess the scalability of this array.

Figure 5.24 shows the source maps produced by beamforming simulation of a single white noise source at 4 kHz using the Underbrink array, the initial array, the optimized array with side lobe weighing, and the optimized small array. The left column presents the results for arrays with the maximum radius of 0.5 m (the Underbrink array, the initial array, and the optimized array with side lobe weighing are scaled down). This case is called the *small scale* case. The right column presents the results for arrays with the maximum radius of 0.95 m (the optimized small array is scaled up). This case is called the *full scale* case.

The first observable point from the results is that the MLW produced by all array is lower in the case of large array as a result of having larger effective diameter. Apart from that, it can be seen from the initial array case, which has quite a high and clear side lobe pattern, that the side lobe pattern in the case of the small array is a 'zoomed-in' pattern of the source map produced by the full scale array. In other words, the small side lobes, together with the main lobe, are enlarged in the case of small array while the pattern of the relative locations between the main lobe and the side lobes are still the same. This is analogous to the enlarged PSF pattern when the array's diameter (D) is decreased as in Figure 2.3b. Therefore, the optimized array will still provide a source map with low side lobes when it is scaled down since it is known that the area around the main lobe produced by this array is clear from high side lobes. On the other hand, the side lobe pattern further away from the main lobe produced by a scaled up version of the small optimal array is revealed when the array's size is scaled up. Therefore, side lobe pattern of the scaled up array is unknown and unpredictable. A suggestion can be made that, when designing an array, the array should be designed at the maximum effective radius. When needed, the array can be scaled down and it is not highly necessary to perform a design optimization again. When the array is scaled down, the array will certainly produce a larger MLW but the side lobe pattern is predictable by examining the beampattern produced by the same array in a larger scale.

5.4. Conclusions and Recommendations

In this chapter, optimization results have been shown, starting from the general optimization case to the optimization cases with some modifications. For each case, five independent optimization runs were performed. The result from the optimization run which gives the lowest objective function value (J_{main}) is shown. For most cases, the optimal values of μ_{nr} are σ_{nr} are similar from all independent runs. For example, the optimal values of μ_{nr} and σ_{nr} from the general optimization case are as expected in Section 4.4. On the other hand, the optimal values of μ_{nn} and σ_{nn} vary more and no clear trend can be seen in some optimization cases.

The optimization for almost all cases showed that the values of MSL and MLW can be simultaneously minimized. For example, the selected array from the general optimization case gives the average of MSL approximately 1.2 dB lower than the Underbrink array at 4 to 10 kHz. The values of MLW at 1 kHz are from this array is also about 5 cm lower than the Underbrink array. This shows that the optimization can quantitatively minimize the values of MSL and MLW. However, there exist a small ring of side lobes close to the main lobe in this optimization case. The ring of small side lobe close to the main lobe was not seen only in the case with side lobes weighing which penalizes the side lobes appearing close to the main lobe with high weighing factors. However, this array gives a smaller reduction of MSL (0.36 dB reduction in average from 4 to 10 kHz) and MLW (1.4 cm reduction at 1 kHz) than the previously-mentioned optimization case.

The results from the simulation multiple sources suggest that the beampattern around the sources still follows the same trend as in the single source case. The influence of side lobes weighing makes the array able to produce an area free from side lobes close to the main lobe. This characteristic is still preserved in the case of multiple sources where the side lobe levels are lower than -15 dB up to about four times the MLW around the main lobes. This makes the optimized array with side lobe weighing the more promising choice for real applications. Therefore, the optimized array from the weighted side lobes is chosen to be tested through experimental validation.

The other variation in the optimization case was the case with a smaller array. It has been shown that the optimization was still able to produce a smaller optimal array which provides the lower MSL and MLW. However, further study has shown that by scaling up the size of the small optimized array will make the array reveal the unknown side lobe pattern which are further away from the main lobe. In contrast, scaling down the size of the full-scale optimized array is less risky. It is certainly known that the MLW will be higher and the side lobe pattern is known from the beampattern of the full-scale array. Therefore, if an array is meant to be used in various sizes,

the array design optimization should be done at the largest scale of usage. It is possible to come up with a smaller optimized array in a smaller scale but the large scale optimized array can also be scaled down and directly be used.

Based on the results discussed so far, the following recommendations can be made:

1. MLW can be used to measure the array's performance in the optimization but MSL may not be sufficient. Another parameter which can also indicate the location of the side lobe should be used. It has been shown that the side lobes weighing according to their distances from the main lobe can be used to produce satisfactory optimization results. However, this finding can be explored further such as by using different weighing functions.

2. The relationship between the microphone's distance from the array's center and the distance to its nearest neighbor microphone, μ_{nn} and σ_{nn}, could be omitted from the optimization. In contrast, further modifications could be made to the microphone distribution wrt. radial distance, μ_{nr} and σ_{nr}, a more flexible distribution curve may be used. For example, a distribution curve that can produce more than one distribution peaks.

3. It is sufficient to simulate only single sound source in the optimization to evaluate the array's performance. The beampattern around the main lobe in the case with a single source can imply the beampattern in the case of multiple sources.

4. Scaling down the array's size is less risky than scaling up. Therefore, to quickly design an array which is meant to be used in various scale, the array should be design at its largest operational scale.

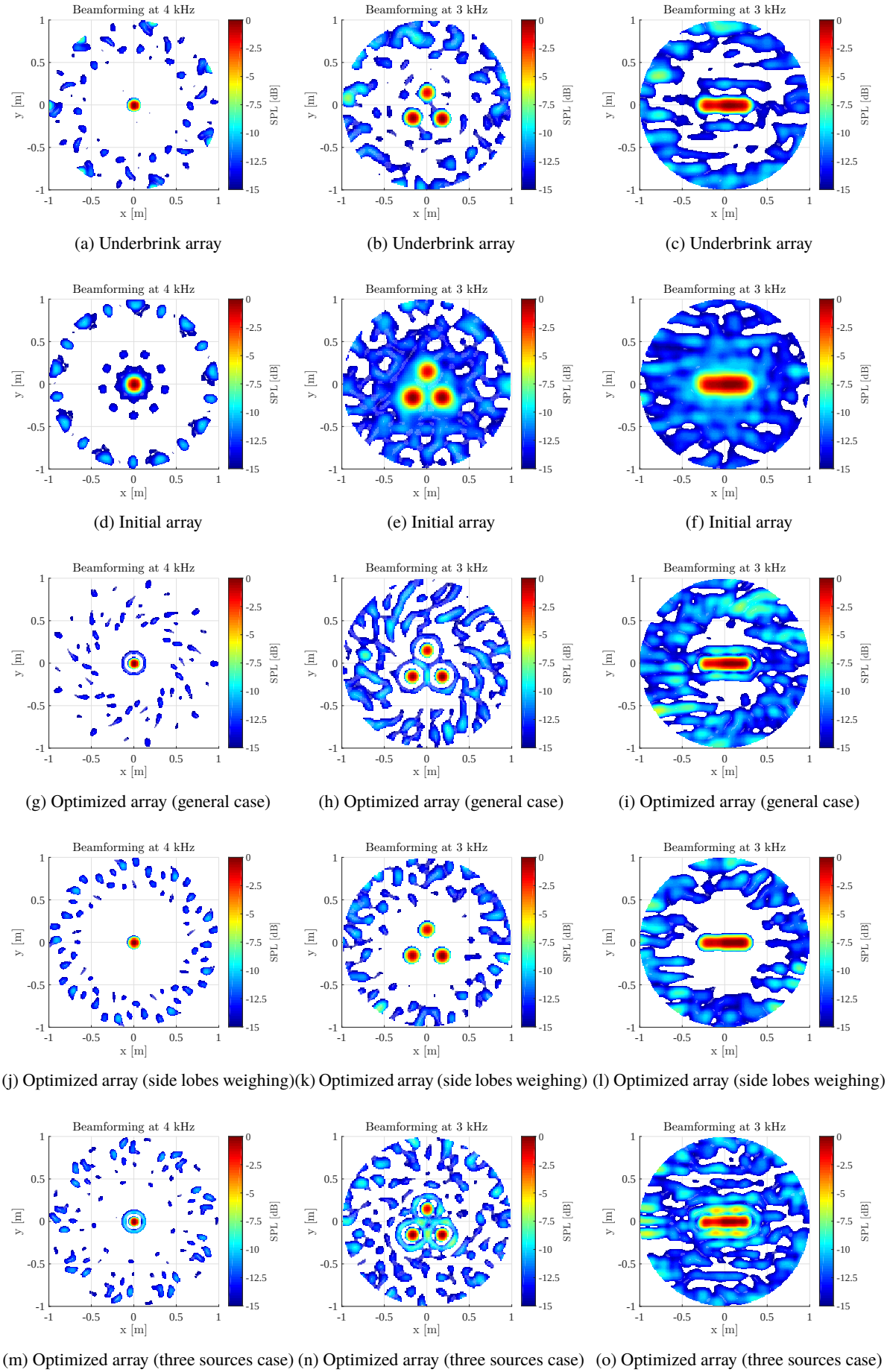

(a) Underbrink array (b) Underbrink array (c) Underbrink array

(d) Initial array (e) Initial array (f) Initial array

(g) Optimized array (general case) (h) Optimized array (general case) (i) Optimized array (general case)

(j) Optimized array (side lobes weighing) (k) Optimized array (side lobes weighing) (l) Optimized array (side lobes weighing)

(m) Optimized array (three sources case) (n) Optimized array (three sources case) (o) Optimized array (three sources case)

Figure 5.23: Source maps from beamforming simulation of one, three, and line sources using the Underbrink array, the initial array, and the optimized arrays from various optimization cases

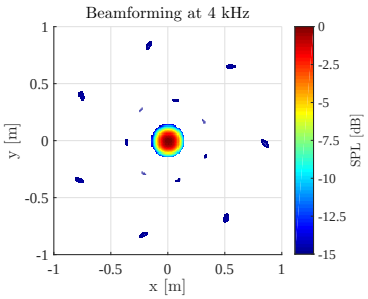

(a) Underbrink array (small scale)

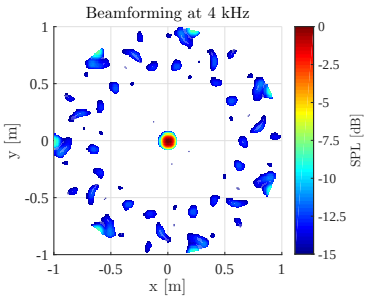

(b) Underbrink array (full scale)

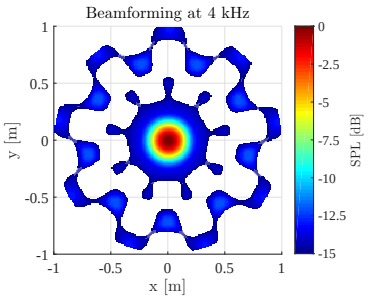

(c) Initial array (small scale)

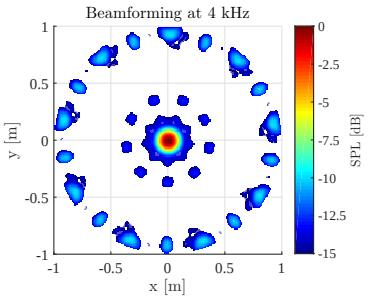

(d) Initial array (full scale)

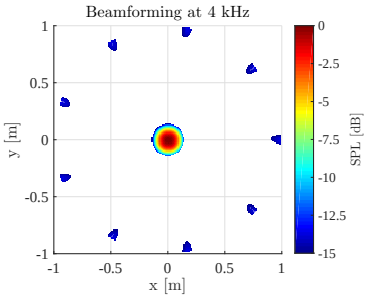

(e) Full scale optimized array (small scale)

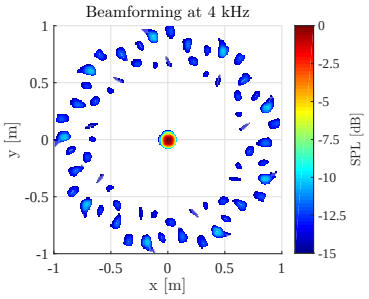

(f) Full scale optimized array (full scale)

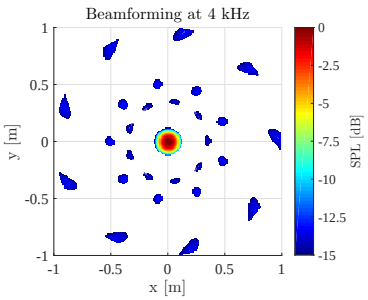

(g) Small scale optimized array (small scale)

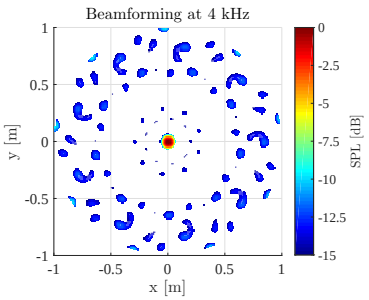

(h) Small scale optimized array (full scale)

Figure 5.24: Source maps from beamforming simulation of one source in the middle of the scan plane at 4 kHz using the Underbrink array, initial array, and the optimized arrays; Small scale means that the array's diameter is 1 m, large scale means that the array's diameter is 1.9 m

6

Experimental Validation

6.1. Objectives and Expected Outcomes

The aims of the experimental validation are to validate the performance of the optimized array, verify the optimization method, and verify the simulation used in the optimization. The validation can be done by comparing the optimal array's beamforming performance with that from the benchmarking Underbrink array to examine whether the optimal array can achieve a comparable or better performance than the benchmark. The verification can be done by comparing the beamforming performance of the optimal array with the initial array from the optimization to prove that the optimization has improved the array's beamforming performance. Finally, the known experimental conditions can be reproduced in the beamforming simulation model used in the optimization. The source map, the values of MSL, and MLW from the experiment and the simulation can be compared. It can be concluded whether the simulation can provide a close anticipation of the MSL, MLW, and the beampattern in the source map. Since it is impossible to test every array through experimentation, this information can be used when interpreting the beamforming simulation results in the future.

6.2. Experimental Set-ups

The experiments were performed in TU Delft's V-tunnel facility which is a vertical flow open-jet wind tunnel in an anechoic room. However, no air flow was operated in the experiments presented in this chapter. Three microphone configurations were used to record sound signal from various source arrangements placed at 1.5 m in front of the acoustic array. The details of the experimental set-ups are described in this section.

6.2.1. Acoustic Array

The acoustic array used in the wind tunnel is a 2×2 m plate with small holes arranged in a square lattice grid. The array holds 64 G.R.A.S. 40PH Free-field Array Microphones which can be relocated to any available holes on the array. Three following microphone configurations were installed on the array:

1. Underbrink array (shown in Figure A.1)
2. Initial array (shown in Figure A.2)
3. Optimized array from the weighted side lobes case (shown in Figure A.3)

The coordinates of every microphone on these arrays were adjusted and assigned to the coordinates of the closest square-lattice holes on the acoustic array. Further details are given in Appendix A.

6.2.2. Sound Sources

Three sound sources were used in the experiments. The sources are independently controlled and used to generate incoherent white noise. The details of the sources are as follows:

1. QindW sound source (shown in Figure 6.1a)
2. Visaton K50 SQ speaker (shown in Figure 6.1b)

(a) (b) (c)

Figure 6.1: Sound sources used in the experiments; (a) QindW sound source, (b) Visaton K50 SQ Speaker (source: `www.visaton.com`), and (c) Phillips SBT30 Wireless Speaker (source: `www.phillips.co.uk`)

3. Phillips SBT30 wireless speaker (shown in Figure 6.1c)

Two main source arrangements were tested: single source using only the QindW source and multiple sources using all three sources. The details of the source arrangements are as follows:

1. Single sound source: QindW source at 1.5 m front of the acoustic array, aligned with the array's center.
2. Multiple sound source: All sources at 1.5 m in front of the acoustic array
   (a) Triangular arrangement: Three sources placed at each corner of a triangle (shown in Figure 6.2a)
      i. Far configuration (details shown in Figure 6.2b)
      ii. Close configuration (details shown in Figure 6.2c)
   (b) Line arrangement: Three sources aligned in a horizontal linear line (shown in Figure 6.2d)
      i. Far configuration (details shown in Figure 6.2e)
      ii. Close configuration (details shown in Figure 6.2f)

6.3. Experimental Results: Single Source Case

6.3.1. Experimental Results and Comparison with Simulation

The source maps showing beamforming results at 4 kHz from the three tested arrays are shown in the first row of Figure 6.3. The source maps shown in the second row are the products of corresponding beamforming simulations which attempt to replicate the experimental conditions used in each test case with a modelled point source emitting white noise. Figure 6.4 and 6.5 show the MSL and MLW of the three tested arrays in the frequency range of 1 to 10 kHz. The solid lines show the MSL and MLW evaluated from the experiments and the dashed lines show those evaluated from the corresponding simulations. The vertical dashed line at 6.3 kHz shows the upper calibration limit of the QindW source. Beyond this point, the radiation pattern and the power emitted by the source is not guaranteed to follow the same trends as they are at lower frequencies.

The source maps show that, at 4 kHz, the initial array produces the largest main lobe while the MLW from the Underbrink and the optimized arrays are similar. This is because the initial array has lower microphone density close to the array's edge than the Underbrink and the optimized array. From the source maps, a pattern of high side lobes is seen for the Underbrink and the initial arrays. At this frequency, the side lobe levels are lower for the optimized array. The simulation results show that the MLW can be closely predicted by the simulation. The locations of side lobes can also be correctly predicted. However, the side lobe levels from the experiments are slightly higher than those from the simulations.

The plots showing MSL and MLW at the remaining frequencies in Figure 6.4 and 6.5 confirm this observation. For all arrays at all frequencies, the MSL values are underestimated by the simulation. The MSL of all arrays are comparable. There is no array which clearly performs better than the others as in Figure 5.8. This could be because the source is not positioned perfectly in the middle of the scan plane as in the simulation used in the optimization, so the side lobe pattern seen in the experiment is partially different from optimization results. In contrast, the MLW values of all arrays at all frequencies are closely predicted by the simulation with the maximum offset of less than 1 cm. The plot also shows that the optimized array is able to achieve the lowest MLW among all tested arrays. This trend agrees with the optimization results shown in Figure 5.9.

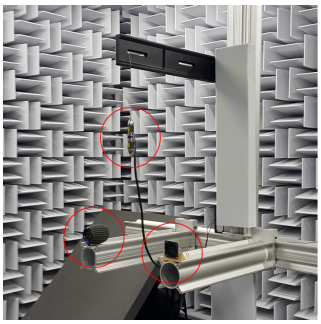

(a) Triangular arrangement

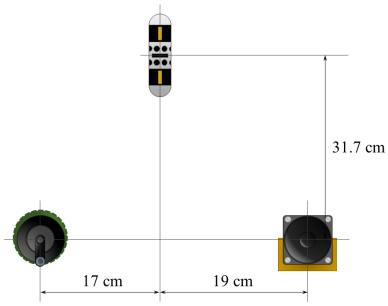

(b) Triangular arrangement, far configuration

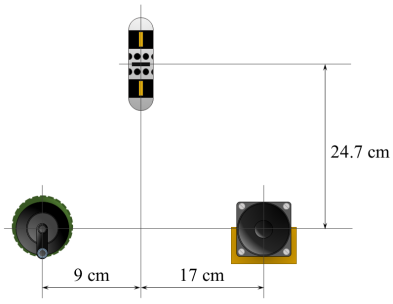

(c) Triangular arrangement, close configuration

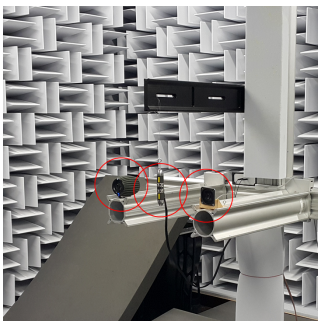

(d) Line arrangement

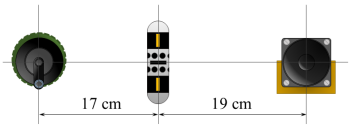

(e) Line arrangement, far configuration

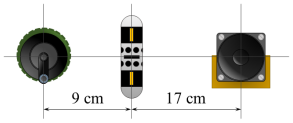

(f) Line arrangement, close configuration

Figure 6.2: Sound source arrangements in the case of multiple sources setting

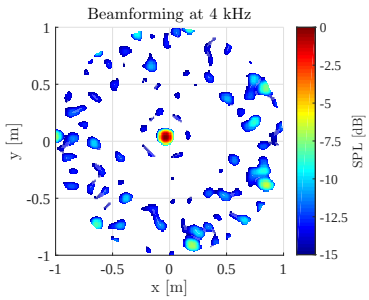

(a) Underbrink array, experiment

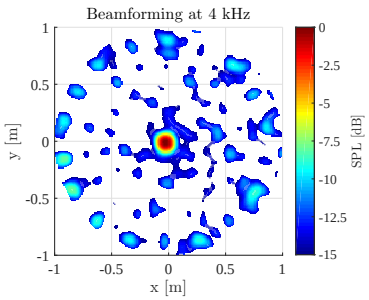

(b) Initial array, experiment

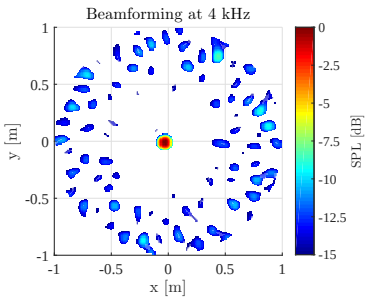

(c) Optimized array, experiment

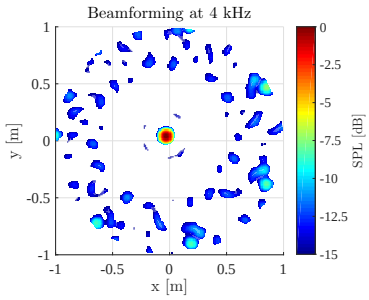

(d) Underbrink array, simulation

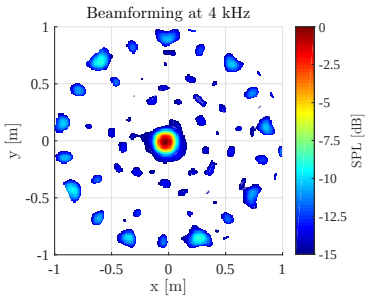

(e) Initial array, simulation

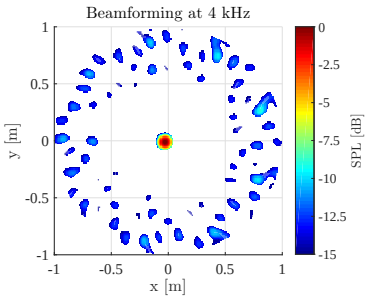

(f) Optimized array, simulation

Figure 6.3: Source maps from beamforming the single sound source from the experiment compared with those from corresponding simulations

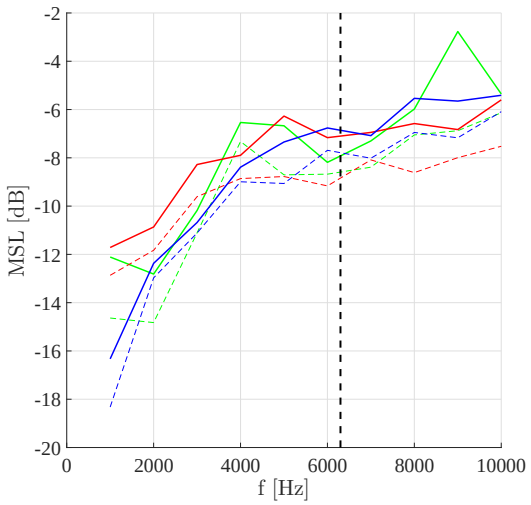

Figure 6.4: MSL of the arrays tested in the experiment compared with MSL determined by corresponding simulations at 1 to 10 kHz

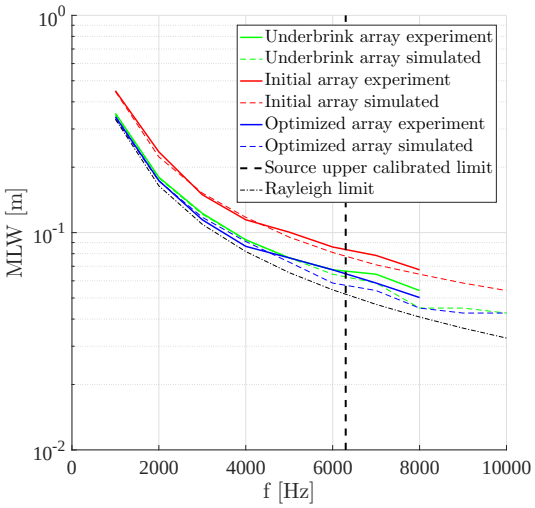

Figure 6.5: MLW of the arrays tested in the experiment compared with MLW determined by corresponding simulations at 1 to 10 kHz

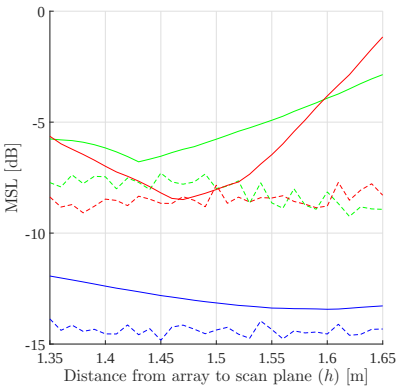

(a) Underbrink array

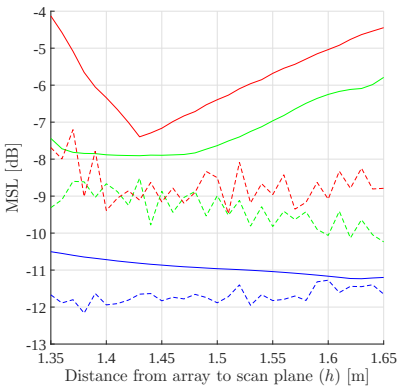

(b) Initial array

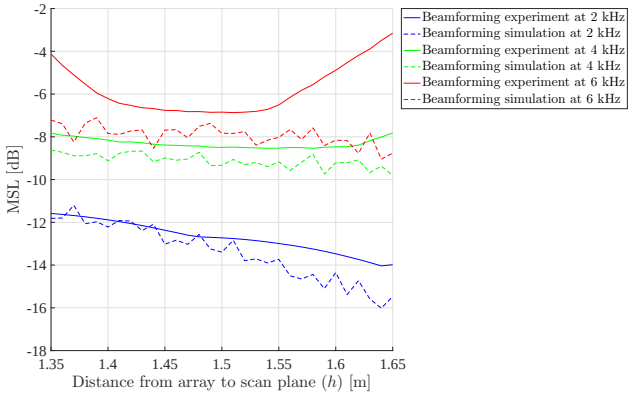

(c) Optimized array

Figure 6.6: MSL variations with distance from the acoustic array to the scan plane from the three array tested, evaluated at 2, 4, and 6 kHz; The solid lines are evaluated from the experimental results, the dash lines are evaluated from the corresponding simulation results

6.3.2. Corrections for the Simulation

As shown previously, there exists a mismatch of the MSL values between the experimental results and the beamforming simulation. The MSL values from the experiments tend to be slightly higher than the MSL predicted in the simulation.

This offset may result from the inaccuracy in defining the distance from the array to the source. The intended distance was 1.5 m. However, the microphones were protruded from the array and the source also has its dimension, i.e. not an ideal point source. Thus, the distance to the scan plane that should be used in the beamforming simulation may not exactly be as measured.

Figure 6.6 shows the plots of resulting MSL wrt. the distance to the scan plane from the three tested arrays at three different beamforming frequencies (f_k = 2, 4, and 6 kHz). The solid lines show the resulting MSL from the experiment and the dashed lines show the resulting MSL from the simulation which assumes that the scan plane and the source are at that particular distance from the array. The plots show that the MSL values of the simulation and the experiment are close when h is around 1.40 to 1.50 m for f_k = 4 and 6 kHz. This suggests that the offset due to protruding microphones needs to be accounted for. The values of MSL are higher when the inaccurate values of h are used. This is because the *relative* power of the source to the environment is not high since there is no source present at that distance in reality. The trend at 2 kHz is different from the remaining frequencies. The MSL is low when the scan plane is defined further away from the array. This can be explained by the array's resolution limit (Rayleigh limit in Equation 2.11). The array's resolution is lower when h is higher and the MLW is larger at higher h. Because of the increasing MLW, the side lobes are pushed away from the source map. Therefore, the side lobe patterns are not captured well in the case of low frequencies. As a result, the MSL values appear to be lower when h increases.

The results from this section suggest that the MSL in the source maps and the difference between the MSL from the experimental result and the simulation can be minimized by carefully selecting the distance from the array to the scan plane.

6.4. Experimental Results: Multiple Sources Case

Figure 6.7 shows the source maps produced by beamforming of sound signals received in the experiment by the three tested arrays at 3 kHz in the multiple sources case. The columns (left to right) show the results from the Underbrink, initial, and optimized array. The rows (top to bottom) show the results for the triangular arrangement (far configuration), triangular arrangement (close configuration), linear arrangement (far configuration), and linear arrangement (close configuration). The trend of the results still follows the trend from the single source case; the initial array produces the highest MLW while the MLW of the Underbrink and the optimized array are about the same. Unlike the Underbrink and the initial arrays, it can still be noticed that the optimized array can produce the area with low side lobes close to the main lobe. This agrees with the investigation presented in Figure 5.23. The last two rows in Figure 6.7 present the source maps in the case where the three sources are linearly aligned. It can be seen that the QindW source produces the lowest SPL compared with the remaining two sources at 3 kHz. When the sources are placed close together, the QindW source is not resolvable in some cases. In the far configuration case, the Underbrink and the optimized array can still distinguish the QindW source while the initial array cannot. This is due to the large MLW the initial array produces which results in lower resolution. On the other hand, the QindW source cannot be resolved by all arrays in the close configuration case. The lobe representing the QindW source appears to blend with that of the Phillips wireless speaker which is placed at 9 cm to the left of it. This distance is lower than the Rayleigh limit at 3 kHz of 11 cm at this particular beamforming frequency. Therefore, this indicates and confirms the limitation of the investigated arrays caused by the Rayleigh limit.

6.5. Conclusions and Recommendations

This section has presented the experimental validation results using three arrays; the benchmarking Underbrink array, the initial array, and the optimized array from the weighted side lobes optimization case. Each array was tested in the V-tunnel with single and multiple sound sources in various arrangements.

The beampatterns from the case with a single sound source follow the same trend as the optimization result. Comparing the measured beampattern with the results from the corresponding simulations indicates that the locations of the side lobes and the MLW can accurately be predicted. However, there exists an MSL offset of around 2 dB between the experiment and the simulation.

A hypothesis has been made that the offset may be caused by the inaccuracy in defining the distance from the array to the scan plane (h). It has been found that this inaccuracy of h plays an influential role in the MSL

compared to the main lobe. Therefore, the correct value of h should be determined before comparing the array's beamforming performance using the experimental data. This recommendation can also be extended to the data processing routine in beamforming in general. Since choosing the correct value of h can help minimize the side lobe levels in the source maps.

The results from the case with multiple sources also follow the same trend and can help confirm that the beampattern for one source can imply how the beampattern will be when there are multiple sources on the scan plane. It has also been shown that the initial array which has poor resolution, i.e. high MLW, cannot resolve the source with relatively low SPL when that source is placed close to the other sources with higher SPLs. However, when the sources are placed closer than the Rayleigh limit, none of the tested array cannot distinguish the source with a relatively low SPL value.

The results shown so far in this chapter have been post-processed only by employing conventional beamforming. However, one possible future work would be to post-process this data set using more advanced beamforming algorithms, especially the cases with multiple sources where some arrays cannot resolve all sources. With this, the contributions of the arrays' beamforming performance and the performance of advanced beamforming algorithms in improving the source maps' quality could be studied.

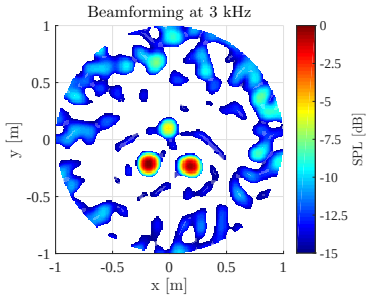

(a) Underbrink array, triangular source arrangement, far configuration

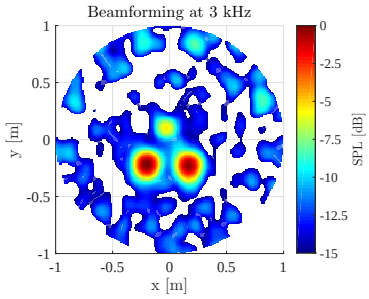

(b) Initial array, triangular source arrangement, far configuration

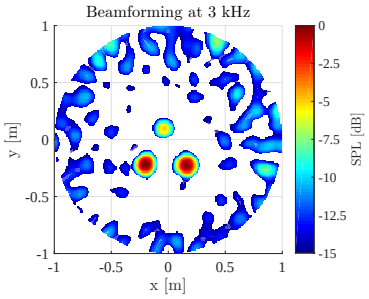

(c) Optimized array, triangular source arrangement, far configuration

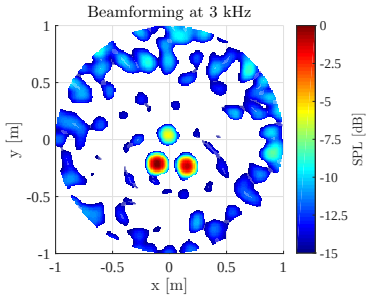

(d) Underbrink array, triangular source arrangement, close configuration

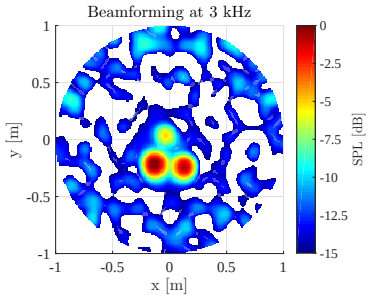

(e) Initial array, triangular source arrangement, close configuration

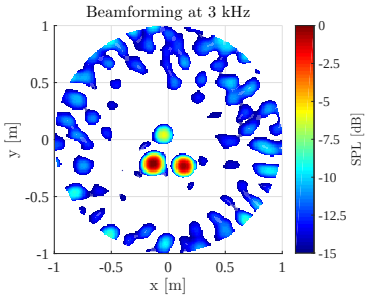

(f) Optimized array, triangular source arrangement, close configuration

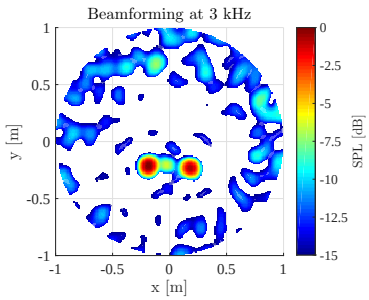

(g) Underbrink array, line source arrangement, far configuration

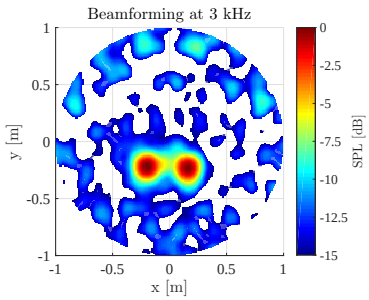

(h) Initial array, line source arrangement, far configuration

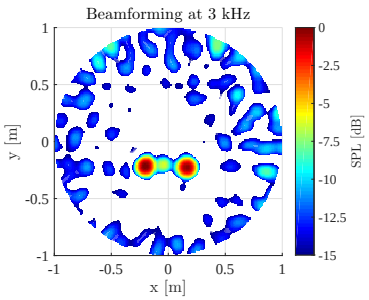

(i) Optimized array, line source arrangement, far configuration

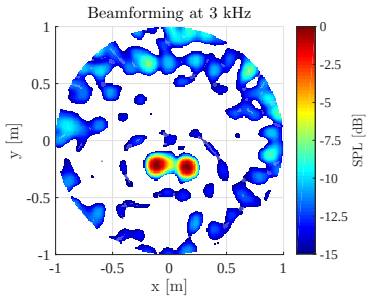

(j) Underbrink array, line source arrangement, close configuration

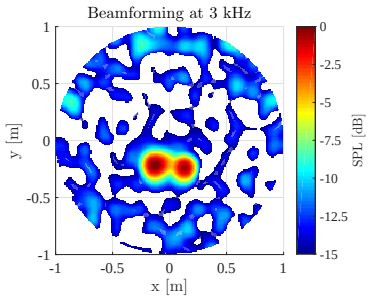

(k) Initial array, line source arrangement, close configuration

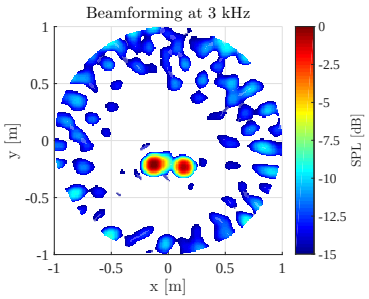

(l) Optimized array, line source arrangement, close configuration

Figure 6.7: Source map from beamforming of the multiple sources case

7

Experimental Case Study: Sound Source Subjected to Air Flow

7.1. Objectives and Expected Outcomes

In addition to the experimental validation, this case study employs the array configurations tested in Chapter 6 in measurements where the sound source is subjected to air flow. This test case is expected to represent the operating conditions of the arrays which are close to the real aero-acoustic applications. The results from the tests can indicate the array's applicability to the practical usages. The possible deviation of the arrays' beamforming performance from the test cases without the flow can be investigated. Corrections needed in the data processing steps can be suggested.

7.2. Experimental Set-up

The experimental set-up is shown in Figure 7.1. The case study was also performed in TU-Delft's V-tunnel facility. In this case study, only the QindW source was used. The source was positioned above a 40×70 cm jet opening. The air flow speed (U_∞) was varied from 0 to 20 m/s with a step of 5 m/s. For each flow speed, the source was switched on and off. When the source was on, white noise was emitted. Three array configurations; the Underbrink array, the initial array, and the optimized array (same set of arrays as in Chapter 6), were used to record the signal.

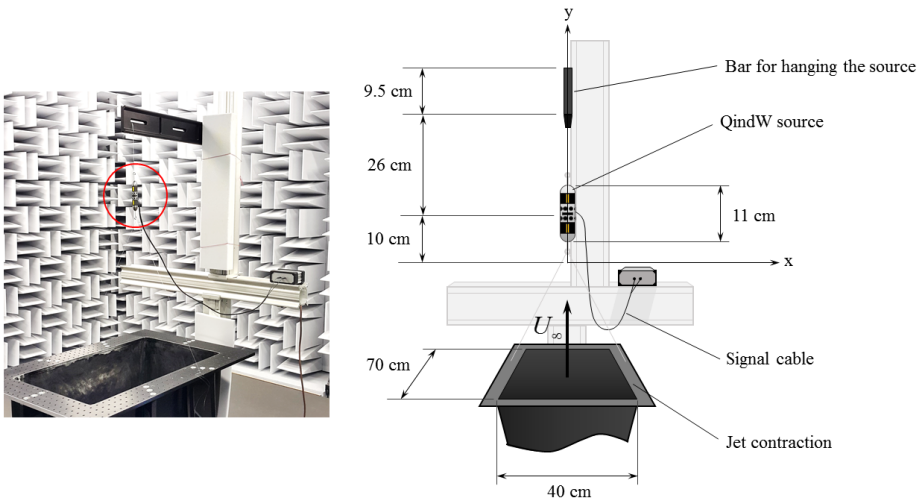

Figure 7.1: Experimental set-up in the case study

7.3. Theoretical Background

In this test case, where the source is positioned inside the air flow and the sound signal is recorded by an acoustic array placed outside the flow, the sound signal from the source has to travel in two different forms of medium. The sound signal from the source first travels through the moving air inside the flow up to the shear layer where the moving air meets air at rest. From that point, the sound signal continues propagating through still air to reach the microphones. Due to this, the propagation path from the source to the microphone is not a straight path. Therefore, the conventional steering vector in the conventional beamforming shown in Equation 2.4 needs to be corrected. There are two main methods for correcting the beamforming results by taking the air flow into account. The simple method still employs conventional beamforming but applies the correction by shifting the source map opposite to the flow direction by a certain calculated distance Padois et al. (2013). The more advanced method applies a 'ray-based' sound propagation model (Dougherty, 2002, Padois et al., 2013) which attempts to model the exact sound propagation path through the shear layer and delay the propagation time based on the exact distance the sound signal needs to travel. However, it is suggested by Padois et al. (2013) that the simplified shifting calculation is valid for the low-speed application up to $M = 0.4$. Since the V-tunnel is a low-speed wind tunnel which can reach the top flow speed of approximately $M = 0.12$, the simplified method is expected to be a sufficient correction and will be employed in this study.

The sound signal which is emitted by a source inside the flow will travel downstream until it reaches the shear layer before travelling in static air to reach the microphones. The point on the shear layer where the sound starts propagating in static air to reach the microphones is located more downstream than the actual downstream location of the source. Therefore, when applying beamforming, the determined source location will appear to shift downstream. According to Padois et al. (2013), this shift can be calculated by

$$y_{sh} = Mw_f, \tag{7.1}$$

or as schematically shown in Figure 7.2; y_{sh} denotes the approximated downstream shifting distance, M is the Mach number which can be calculated from $M = U_\infty/c$, where U_∞ is the flow speed. The distance from the source to the shear layer is denoted by w_f. Since the exact distance from the source to the shear layer is unknown, this distance needs to be approximated.

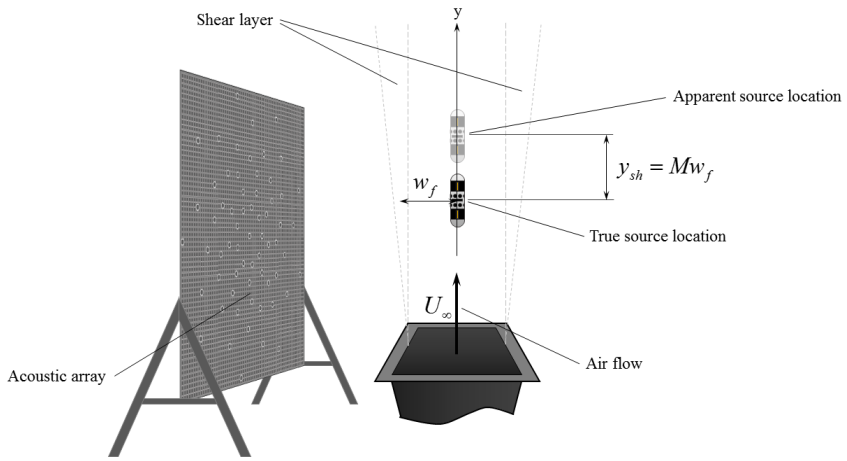

Figure 7.2: Calculation of apparent source location shift

7.4. Results

Figure 7.3 shows the source maps produced by beamforming of the source signal received by the arrays at 4 kHz. The source maps shown are the results of applying conventional beamforming without any corrections. The source maps in different columns are the results from different arrays; Underbrink, initial, and optimized from left to right. The source maps in different rows are from different flow speed (U_∞) from 0 to 20 m/s with the step of 5 m/s from top to buttom. It can be observed that, despite being subjected to the air flow, the source maps produced by the three tested arrays still follow the same pattern as the results shown in Figure 6.3. The characteristics of the beampattern produced by each array, such as the wide main lobe for the initial array and the

clean area around the main lobe by the optimized array are still preserved. Although the source shift with flow speed is hardly recognizable from the source map, the apparent source Y location actually moves downstream (upwards) with increasing U_∞ in a scale of centimetres. Figure 7.4 shows the apparent source Y location shift from the apparent source Y location with no flow (at U_∞ = 0 m/s) for the three tested arrays wrt. U_∞ together with the anticipated source shift calculated from Equation 7.1. Since the distance from the source to the shear layer (w_f) is uncertain, three different distances are used in this plot; w_f = 0.4, 0.5, and 0.6 m. It can be observed that all arrays can similarly capture the shift of the source apparent Y location. Moreover, the plot also shows that Equation 7.1 can predict the source shift quite accurately, especially when using w_f = 0.5 m.

7.5. Conclusions and Recommendations

Based on the findings from this case study, it can be concluded that the array's beamforming performance in the case of having air flow hardly deviates from the test cases without the flow. It is also confirmed that, without any corrections in the beamforming algorithm, the apparent source location in the source map will slightly shift downstream with increasing flow speed. However, the simplified correction can accurately predict the shift of the source's apparent location and can be implemented to shift the source map back upstream.

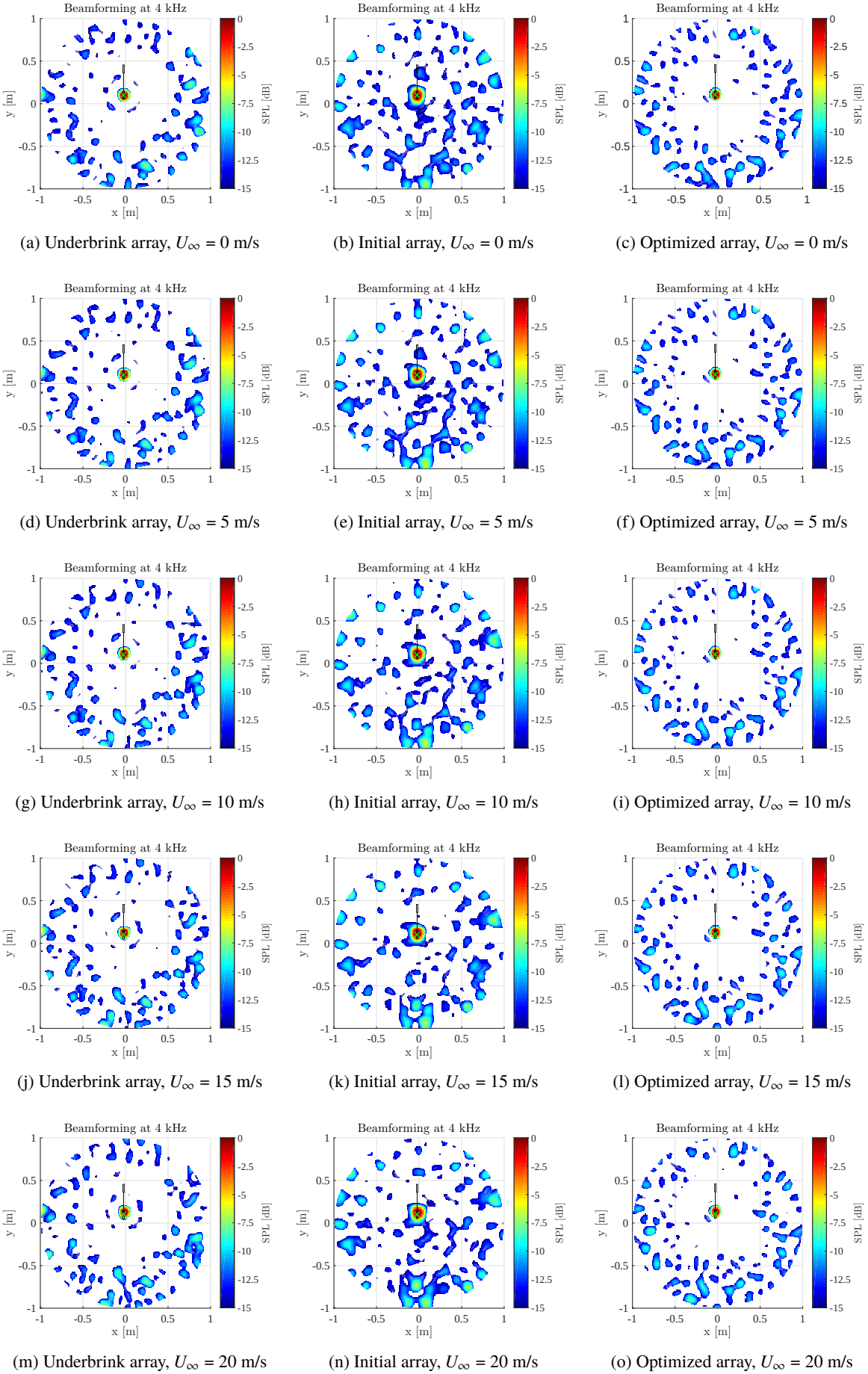

(a) Underbrink array, U_∞ = 0 m/s (b) Initial array, U_∞ = 0 m/s (c) Optimized array, U_∞ = 0 m/s

(d) Underbrink array, U_∞ = 5 m/s (e) Initial array, U_∞ = 5 m/s (f) Optimized array, U_∞ = 5 m/s

(g) Underbrink array, U_∞ = 10 m/s (h) Initial array, U_∞ = 10 m/s (i) Optimized array, U_∞ = 10 m/s

(j) Underbrink array, U_∞ = 15 m/s (k) Initial array, U_∞ = 15 m/s (l) Optimized array, U_∞ = 15 m/s

(m) Underbrink array, U_∞ = 20 m/s (n) Initial array, U_∞ = 20 m/s (o) Optimized array, U_∞ = 20 m/s

Figure 7.3: Source maps produced from beamforming at 4 kHz using the three tested arrays at varying flow speed (U_∞), The × sign shows the identified source location at U_∞ = 0 m/s

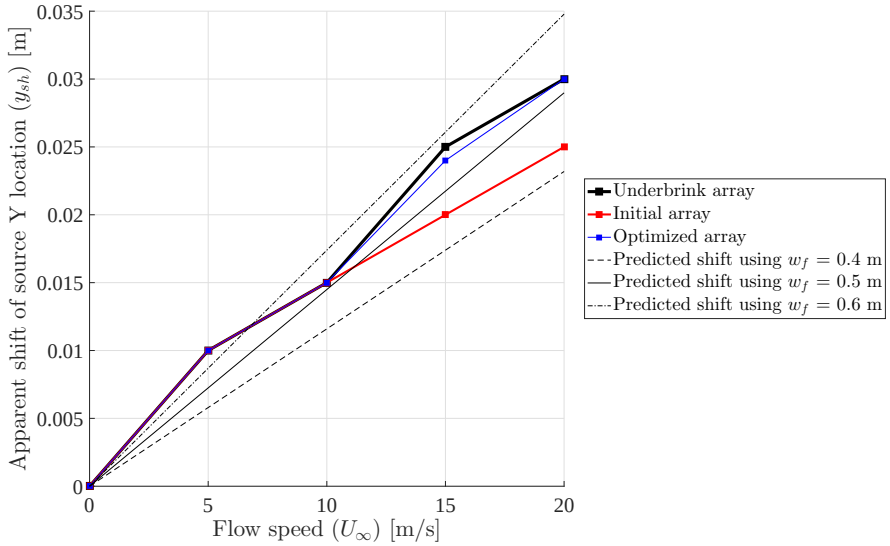

Figure 7.4: Actual shift of the source apparent Y location wrt. the flow speed (U_∞) from the three tested arrays and the anticipated shift using varying distances to the shear layer (w_f)

8

Conclusions and Recommendations

8.1. Conclusions

The objective of this thesis project was to develop an optimal acoustic array to be used in TU Delft's low speed wind tunnel, the V-tunnel, which will be used in aero-acoustic measurements. This thesis has been divided into two main phases. Firstly, the computational optimization part where the optimization method was developed and the arrays' beamforming performance was investigated by means of simulation. Second, the experimental validation phase where the beamforming performance of the selected optimal array together with additional reference arrays were tested experimentally in the V-tunnel.

The beamforming performance of an array can be measured by determining the MSL and MLW from the beampattern. It has been concluded that there are three main relationships linking the array's geometry to its performance. First, the array's aperture or dispersion of microphones on the array which relates to the trade-off between MSL and MLW when only a limited number of microphone is available. Next, the nearest neighbor microphone distance which can be linked with the existence of side lobes or grating lobes in the array's beampattern. Finally, the array's redundancy which can also be linked to the array's side lobe suppression ability and can be ensured by designing a multi-arm spiral array with even numbers of spiral arms and microphones per spiral arm.

The previous works suggested further that, in acoustic array design optimization, the optimization problem scale should be kept as minimal as possible to save the computational time, effort, and avoid impractical results.

The insights were used to develop the optimization method which consists of two optimization loops. The main optimization loop has only four design variables which are used to collectively describe microphone distribution on the array without exact specifications of every individual microphone's location. The nested optimization loop attempts to generate a set of multi-arm spiral arrays which satisfy the predefined geometry descriptions.

It has been proven that the proposed optimization method provides acoustic arrays which can achieve quantitatively lower MSL and MLW than the benchmarking Underbrink array. However, out of all variations, the optimization which attempted to minimize the side lobes which appear close to the main lobe together with the MLW can produce the most satisfactory beamforming performance. That is, the optimized array can produce a low MLW together with an area with side lobes lower than -15 dB up to the distance of approximately four times the MLW around the main lobe. This behavior is still present even in the case of multiple sources where the beampattern still follows the same trend as in the single source case.

The experimental validation part confirmed these findings and also verified that the beamforming simulation model used in the optimization can be used to closely predict the side lobe pattern and the MLW of the real array. However, the side lobe levels are still somewhat underestimated by the simulation.

The case study where the source was tested with air flow to replicate the array's operating condition also confirmed the usability of the optimized array. A simple method by shifting the source map opposite to the flow after performing beamforming has been proven to be sufficient as a correction for the post-processing step.

8.2. Recommendations

Based on the insights obtained throughout this thesis project, the recommendations can be given in two main categories; the recommendations regarding the optimization method and the recommendations regarding the experimental data processing.

1. Recommendations for the optimization method

   (a) The method for measuring the MLW can directly be used in the optimization to come up with an array that gives a low MLW. However, a more elaborated parameter which also take into account the locations of the side lobes should be used instead of the MSL. For example, the weighted side lobes according to their distances from the main lobe.

   (b) Only the distribution function of the microphone number wrt. the array's radial distance could be used in the optimization. However, various distribution curve shapes should be employed in further research works since the optimal array may not only have one radial distance where the microphone distribution density is at the maximum.

   (c) Beamforming evaluation using only one sound source can imply the array's beamforming performance and the appearance of the source maps in the case of multiple sources. Therefore, this beamforming simulation scheme is sufficient in the optimization.

   (d) When designing an acoustic array which is meant to be used in multiple sizes, the array should be designed at its maximum operating size. The array designed can directly be scaled down. In this way, the side lobe pattern and the MLW increment can certainly be anticipated.

2. Recommendations for the experimental data processing

   (a) The distance from the array to the scan plane (h) is worth checking when performing beamforming as using the correct distance can result in a lower side lobe level relative to the main lobe.

   (b) The experimental data presented in this report can be post-processed with more advanced beamforming algorithms to study the contributions of the array's geometry and the beamforming algorithms in improving the beamforming performance.

   (c) Since the maximum achievable Mach number by the V-tunnel is low, the simple source map shifting correction shown in Equation 7.1 can be done after performing beamforming to correctly localize sound sources subjected to air flow.

Bibliography

Elias JG Arcondoulis, Con J Doolan, Anthony C Zander, and Laura A Brooks. Design and calibration of a small aeroacoustic beamformer. In *20th International Congress on Acoustics, Sydney, New South Wales*, 2010.

Andreas Austeng, Sverre Holm, Peter K Weber, Niels Aakvaag, and Kambiz Iranpour. 1d and 2d algorithmically optimized sparse arrays. volume 2, pages 1683–1686. IEEE, 1997.

David Ayllón, Roberto Gil-Pita, Manuel Utrilla-Manso, and Manuel Rosa-Zurera. An evolutionary algorithm to optimize the microphone array configuration for speech acquisition in vehicles. *Engineering Applications of Artificial Intelligence*, 34:37–44, 2014.

SA Babale, DD Dajab, and K Ahmad. Synthesis of a linear antenna array for maximum side-lobe level reduction. *International Journal of Computer Applications*, 85(16), 2014.

Josh M Beal, Amit Shukla, Olga A Brezhneva, and Mark A Abramson. Optimal sensor placement for enhancing sensitivity to change in stiffness for structural health monitoring. *Optimization and Engineering*, 9(2):119–142, 2008.

Thomas F Brooks and William M Humphreys. A deconvolution approach for the mapping of acoustic sources (damas) determined from phased microphone arrays. *Journal of Sound and Vibration*, 294(4):856–879, 2006.

Kit Yan Chan, Ka Fai Cedric Yiu, and Sven Nordholm. Microphone configuration for beamformer design using the taguchi method. *Measurement*, 96:58–66, 2017.

Jacob Juhl Christensen and Jorgen Hald. Beam forming array of transducers, August 29 2006. US Patent 7,098,865.

Malcolm J Crocker. *Handbook of acoustics*. John Wiley & Sons, 1998.

Robert P Dougherty. Spiral-shaped array for broadband imaging, November 17 1998. US Patent 5,838,284.

Robert P Dougherty. Beamforming in acoustic testing. In *Aeroacoustic Measurements*, pages 62–97. Springer, 2002.

DE Dudgeon and Don H Johnson. Array signal processing: concepts and techniques. *PRT Prentice Hall, Englewood Cliffs, NJ*, 1993.

Klaus Ehrenfried, Lars Koop, Arne Henning, and Kristian Kaepernick. Effects of wind-tunnel noise on array measurements in closed test sections. 2006.

Thomas Geyer, Ennes Sarradj, and Christoph Fritzsche. Porous airfoils: noise reduction and boundary layer effects. *International journal of aeroacoustics*, 9(6):787–820, 2010.

Richard A Haubrich. Array design. *Bulletin of the Seismological Society of America*, 58(3):977–991, 1968.

Randy L Haupt. Thinned arrays using genetic algorithms. *IEEE Transactions on Antennas and Propagation*, 42 (7):993–999, 1994.

David Havelock, Sonoko Kuwano, and Michael Vorländer. *Handbook of signal processing in acoustics*. Springer Science & Business Media, 2008.

Robert Hooke and Terry A Jeeves. "direct search"solution of numerical and statistical problems. *Journal of the ACM (JACM)*, 8(2):212–229, 1961.

J Hurault, A Gupta, E Sloth, NC Nielsen, A Borgoltz, and P Ravetta. Aeroacoustic wind tunnel experiment for serration design optimisation and its application to a wind turbine rotor. 2015.

Nanbo Jin and Yahya Rahmat-Samii. Advances in particle swarm optimization for antenna designs: Real-number, binary, single-objective and multiobjective implementations. *IEEE Transactions on Antennas and Propagation*, 55(3):556–567, 2007.

Florent Le Courtois, Jean-Hugh Thomas, Franck Poisson, and Jean-Claude Pascal. Genetic optimisation of a plane array geometry for beamforming. application to source localisation in a high speed train. *Journal of Sound and Vibration*, 371:78–93, 2016.

Robert Michael Lewis and Virginia Torczon. Pattern search algorithms for bound constrained minimization. *SIAM Journal on Optimization*, 9(4):1082–1099, 1999.

Zhibao Li, Ka Fai Cedric Yiu, and Zhiguo Feng. A hybrid descent method with genetic algorithm for microphone array placement design. *Applied Soft Computing*, 13(3):1486–1490, 2013.

Anwar Malgoezar, Mirjam Snellen, Pieter Sijtsma, and Dick Simons. Improving beamforming by optimization of acoustic array microphone positions. In *6th Berlin Beamforming Conference*, pages 1–24, 2016a.

Anwar Malgoezar, Mirjam Snellen, Dick Simons, and Pieter Sijtsma. Using global optimization methods for acoustic source localization. 2016b.

Roberto Merino-Martínez, Mirjam Snellen, and Dick G Simons. Functional beamforming applied to imaging of flyover noise on landing aircraft. *Journal of Aircraft*, 53(6):1830–1843, 2016.

A Nordborg, J Wedemann, and L Willenbrink. Optimum array microphone configuration. 2000.

Stefan Oerlemans, Murray Fisher, Thierry Maeder, and Klaus Kögler. Reduction of wind turbine noise using optimized airfoils and trailing-edge serrations. *AIAA journal*, 47(6):1470–1481, 2009.

Thomas Padois, Christian Prax, and Vincent Valeau. Numerical validation of shear flow corrections for beamforming acoustic source localisation in open wind-tunnels. *Applied Acoustics*, 74(4):591–601, 2013.

Zebb Prime and Con Doolan. A comparison of popular beamforming arrays. *polar*, 1:5, 2013.

Zebb Prime, Con Doolan, and Branko Zajamsek. Beamforming array optimisation and phase averaged sound source mapping on a model wind turbine. In *Inter-Noise and Noise-Con Congress and Conference Proceedings*, volume 249, pages 1078–1086. Institute of Noise Control Engineering, 2014.

Christof Puhle and Sean Hollands. On the sunflower spiral: acoustical holography results. In *INTER-NOISE and NOISE-CON Congress and Conference Proceedings*, volume 253, pages 5715–5726. Institute of Noise Control Engineering, 2016.

Abdelmadjid Recioui. Sidelobe level reduction in linear array pattern synthesis using particle swarm optimization. *Journal of Optimization Theory and Applications*, 153(2):497–512, 2012. ISSN 1573-2878. doi: 10.1007/s10957-011-9953-9. URL `http://dx.doi.org/10.1007/s10957-011-9953-9`.

Ennes Sarradj. Three-dimensional acoustic source mapping with different beamforming steering vector formulations. *Advances in Acoustics and Vibration*, 2012, 2012.

Ennes Sarradj. Optimal planar microphone array arrangements. *Fortschritte der Akustik-DAGA*, pages 220–223, 2015.

Ennes Sarradj. A generic approach to synthesize optimal array microphone arrangements. In *Proceedings of the 6th Berlin Beamforming Conference*, 2016.

Ennes Sarradj, Christian Schulze, and Andreas Zeibig. Aspects of source separation in beamforming. In *Proceedings of the Berlin Beamforming Conference*, 2006.

Yoko Sasaki, Tomoaki Fujihara, Satoshi Kagami, Hiroshi Mizoguchi, and Kyoichi Oro. 32-channel omnidirectional microphone array design and implementation. *Journal of Robotics and Mechatronics*, 23(3): 378–385, 2011.

C Schulze, E Sarradj, and A Zeibig. Characteristics of microphone arrays. In *INTER-NOISE and NOISE-CON Congress and Conference Proceedings*, volume 2004, pages 2753–2759. Institute of Noise Control Engineering, 2004.

Ho-Chul Shin, Will Graham, Pieter Sijtsma, Christodoulos Andreou, and Andrew C Faszer. Implementation of a phased microphone array in a closed-section wind tunnel. *AIAA journal*, 45(12):2897–2909, 2007.

Pieter Sijtsma. Clean based on spatial source coherence. *International journal of aeroacoustics*, 6(4):357–374, 2007.

Pieter Sijtsma and Robert Stoker. Determination of absolute contributions of aircraft noise components using fly-over array measurements. In *10th AIAA/CEAS Aeroacoustics Conference*, page 2958, 2004.

Pieter Sijtsma, Stefan Oerlemans, and Hermann Holthusen. Location of rotating sources by phased array measurements. page 2167, 2001.

DG Simons and M Snellen. Multi-frequency matched-field inversion of benchmark data using a genetic algorithm. *Journal of Computational Acoustics*, 6(01n02):135–150, 1998.

Dick G Simons, Mirjam Snellen, Bert van Midden, M Arntzen, and DHT Bergmans. Assessment of noise level variations of aircraft flyovers using acoustic arrays. *Journal of Aircraft*, 52(5):1625–1633, 2015.

Paul T Soderman and Christopher S Allen. Microphone measurements in and out of airstream. In *Aeroacoustic Measurements*, pages 1–61. Springer, 2002.

Todd A Sriver, James W Chrissis, and Mark A Abramson. Pattern search ranking and selection algorithms for mixed variable simulation-based optimization. *European journal of operational research*, 198(3):878–890, 2009.

Rainer Storn. On the usage of differential evolution for function optimization. In *Fuzzy Information Processing Society, 1996. NAFIPS., 1996 Biennial Conference of the North American*, pages 519–523. IEEE, 1996.

Rainer Storn and Kenneth Price. Differential evolution–a simple and efficient heuristic for global optimization over continuous spaces. *Journal of global optimization*, 11(4):341–359, 1997.

Zana Sulaiman. Effect of open-jet shear layers on aero acoustic wind tunnel measurements. *For obtaining the degree of Master of Science in Aerospace Engineering at Delft University of Technology*, 2011.

Virginia Torczon. On the convergence of pattern search algorithms. *SIAM Journal on optimization*, 7(1):1–25, 1997.

James R Underbrink. Circularly symmetric, zero redundancy, planar array having broad frequency range applications, March 20 2001. US Patent 6,205,224.

James R Underbrink. Aeroacoustic phased array testing in low speed wind tunnels. pages 98–217. Springer, 2002.

Rick van der Goot, Jorg Hendriks, Kirk Scheper, Giel Hermans, Wouter van der Wal, and Dick G Simons. A low cost, high resolution acoustic camera with a flexible microphone configuration. *Paper, Delft University of Technology, Delft, Netherlands*, 2012.

Michael Wetter and Jonathan Wright. Comparison of a generalized pattern search and a genetic algorithm optimization method. In *Proceedings of the 8th International IBPSA Conference, Eindhoven, Netherlands*, pages 1401–1408, 2003.

Jingjing Yu and Kevin D Donohue. Geometry descriptors of irregular microphone arrays related to beamforming performance. *EURASIP Journal on Advances in Signal Processing*, 2012(1):249, 2012.

Jingjing Yu and Kevin D Donohue. Optimal irregular microphone distributions with enhanced beamforming performance in immersive environments. *The Journal of the Acoustical Society of America*, 134(3):2066–2077, 2013.

Jingjing Yu and Kevin D Donohue. Optimization for randomly described arrays based on geometry descriptors. In *Acoustics, Speech and Signal Processing (ICASSP), 2015 IEEE International Conference on*, pages 549–553. IEEE, 2015.

Jingjing Yu, Fashan Yu, and Yinglei Li. Optimization of microphone array geometry with evolutionary algorithm. *JCP*, 8(1):200–207, 2013.

A

Coordinates of the Tested Arrays

Table A.1: Coordinates and slot number of the Underbrink array when used in the V-tunnel

Mic. No.	Array coordinates		Slot No.		Mic. No.	Array coordinates		Slot No.	
	x [m]	y [m]	x	y		x [m]	y [m]	x	y
1	-0.155	0.18	56	78	33	0.155	0.72	75	114
2	-0.455	0.57	36	104	34	-0.02	0.81	65	120
3	-0.65	0.495	23	99	35	-0.2	0.855	53	123
4	-0.8	0.39	13	92	36	-0.365	0.87	42	124
5	-0.92	0.255	5	83	37	0.02	0.555	66	103
6	-0.425	0.36	38	90	38	-0.245	0.6	50	106
7	-0.62	0.195	25	79	39	-0.11	0.405	59	93
8	-0.38	0.18	41	78	40	0.05	0.24	68	82
9	-0.38	-0.195	41	53	41	-0.02	0	65	66
10	-0.74	0	17	66	42	0.095	0	71	66
11	-0.785	-0.195	14	53	43	0.065	0.075	69	71
12	-0.8	-0.39	13	40	44	-0.02	0.09	65	72
13	-0.77	-0.555	15	29	45	-0.08	0.045	61	69
14	-0.545	-0.105	30	59	46	-0.08	-0.045	61	63
15	-0.53	-0.36	31	42	47	-0.02	-0.09	65	60
16	-0.455	-0.585	36	27	48	0.065	-0.075	69	61
17	-0.26	-0.48	49	34	49	-0.05	-0.645	63	23
18	0.71	-0.63	112	24	50	0.17	-0.72	76	18
19	-0.245	-0.015	50	65	51	0.365	-0.72	89	18
20	-0.08	-0.42	61	38	52	0.545	-0.69	101	20
21	-0.14	-0.195	57	53	53	0.23	-0.495	80	33
22	0.275	-0.33	83	44	54	-0.335	-0.735	44	17
23	0.065	-0.24	69	50	55	-0.2	-0.855	53	9
24	0.23	-0.09	80	60	56	-0.05	-0.945	63	3
25	0.47	-0.435	96	37	57	0.665	0.33	109	88
26	0.665	-0.315	109	45	58	0.62	0.525	106	101
27	0.8	-0.165	118	55	59	0.545	0.69	101	112
28	0.89	0	124	66	60	0.455	0.84	95	122
29	0.935	0.165	127	77	61	0.44	0.33	94	88
30	0.53	-0.135	100	57	62	0.32	0.555	86	103
31	0.635	0.105	107	73	63	0.26	0.345	82	89
32	0.425	0.015	93	67	64	0.215	0.12	79	74

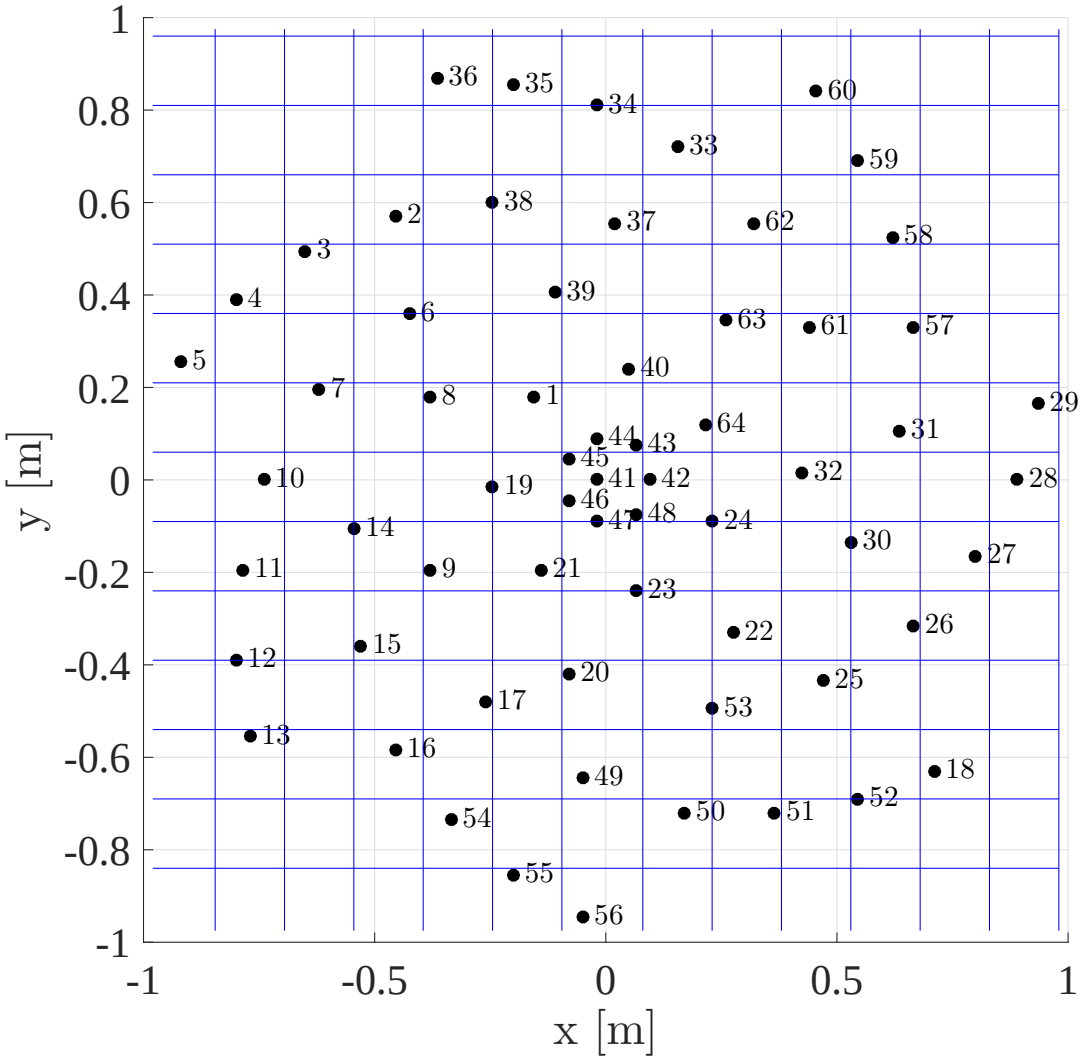

Figure A.1: Underbrink array when installed in the V-tunnel with the corresponding microphone numbers

Table A.2: Coordinates and slot number of the initial array when used in the V-tunnel

Mic. No.	Array coordinates		Slot No.		Mic. No.	Array coordinates		Slot No.	
	x [m]	y [m]	x	y		x [m]	y [m]	x	y
1	0.11	-0.105	72	59	33	-0.29	-0.045	47	63
2	0.155	-0.015	75	65	34	-0.2	-0.225	53	51
3	0.185	-0.24	77	50	35	-0.35	-0.195	43	53
4	0.29	-0.06	84	62	36	-0.515	-0.09	32	60
5	0.35	-0.21	88	52	37	-0.335	-0.405	44	39
6	0.515	-0.09	99	60	38	-0.62	-0.345	25	43
7	0.335	-0.405	87	39	39	-0.935	-0.15	4	56
8	0.62	-0.36	106	42	40	-0.62	-0.72	25	18
9	0.05	0	68	66	41	-0.02	0	65	66
10	0.035	0.03	67	68	42	0.02	0.045	66	69
11	0.035	-0.03	67	64	43	-0.02	0.045	65	69
12	0.125	0.09	73	72	44	-0.05	0.015	63	67
13	-0.065	0.135	62	75	45	-0.05	-0.015	63	65
14	-0.14	0.06	57	70	46	-0.02	-0.045	65	63
15	-0.08	-0.12	61	58	47	0.02	-0.045	66	63
16	0.26	0.135	82	75	48	-0.14	-0.045	57	63
17	-0.245	0.165	50	77	49	0.035	0.15	67	76
18	-0.26	0.315	49	87	50	0.11	0.27	72	84
19	-0.395	0.075	40	71	51	-0.095	0.285	60	85
20	-0.455	0.27	36	84	52	0.02	0.405	66	93
21	-0.455	0.555	36	103	53	0.185	0.495	77	99
22	-0.695	0.135	20	75	54	-0.17	0.495	55	99
23	-0.32	0.9	45	126	55	0.02	0.705	66	113
24	-0.815	0.48	12	98	56	0.335	0.885	87	125
25	0.395	0.06	91	70	57	0.02	-0.15	66	56
26	0.26	0.315	82	87	58	-0.02	-0.3	65	46
27	0.455	0.255	95	83	59	-0.14	-0.375	57	41
28	0.695	0.12	111	74	60	0.14	-0.39	74	40
29	0.47	0.54	96	102	61	-0.02	-0.525	65	31
30	0.605	-0.735	105	17	62	-0.245	-0.66	50	22
31	0.935	-0.18	127	54	63	0.23	-0.675	80	21
32	0.83	0.465	120	97	64	-0.02	-0.945	65	3

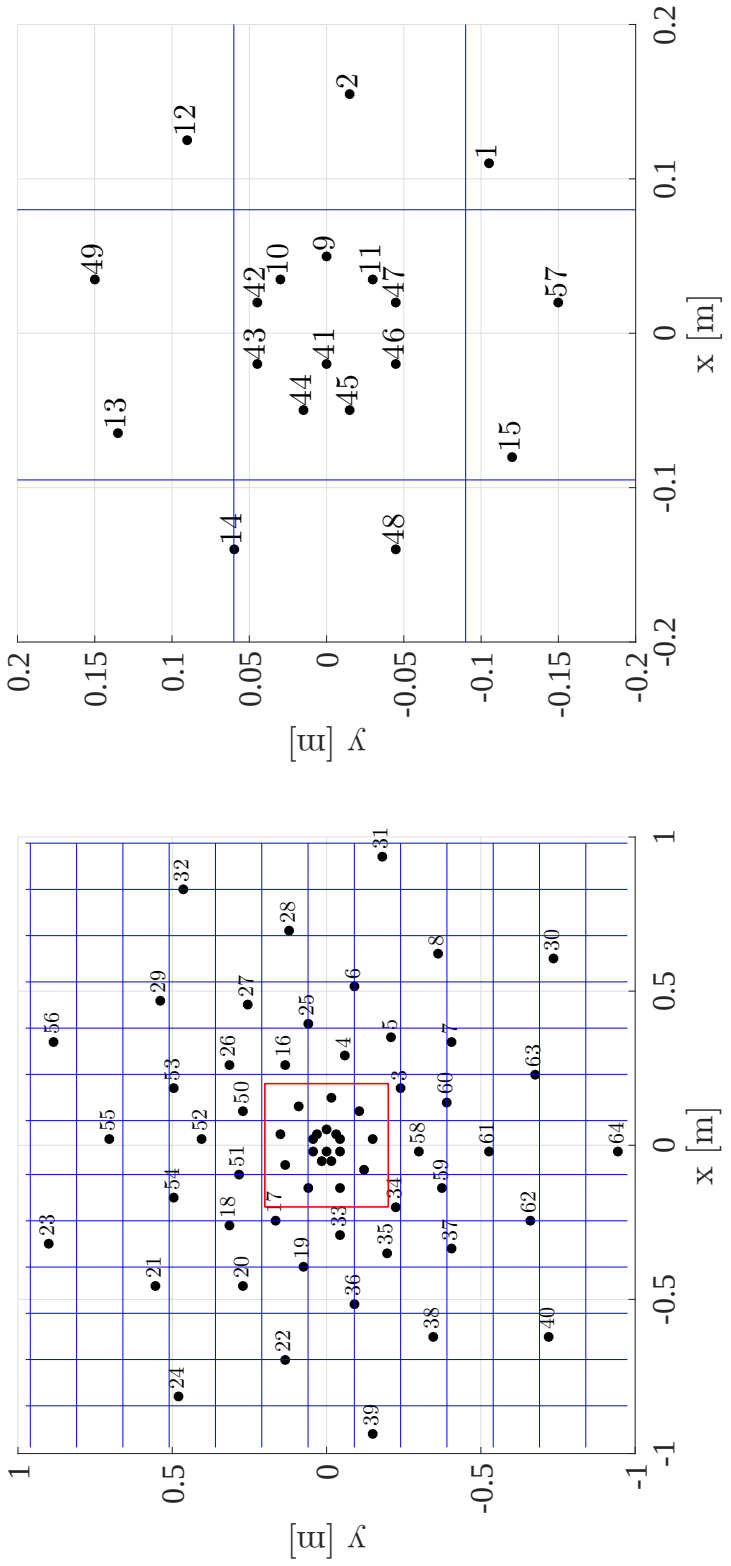

Figure A.2: Initial array when installed in the V-tunnel with the corresponding microphone numbers

Table A.3: Coordinates and slot number of the optimized array when used in the V-tunnel

Mic. No.	Array coordinates		Slot No.		Mic. No.	Array coordinates		Slot No.	
	x [m]	y [m]	x	y		x [m]	y [m]	x	y
1	-0.095	-0.525	60	31	33	-0.275	-0.24	48	50
2	0.02	-0.66	66	22	34	-0.425	-0.345	38	43
3	-0.275	-0.72	48	18	35	-0.65	-0.135	23	57
4	0.245	-0.72	81	18	36	-0.41	-0.525	39	31
5	-0.875	-0.075	8	61	37	-0.68	-0.36	21	42
6	-0.08	-0.87	61	8	38	-0.62	-0.615	25	25
7	-0.5	-0.81	33	12	39	-0.89	0.345	7	89
8	0.14	-0.945	74	3	40	-0.905	-0.3	6	46
9	-0.275	0.24	48	82	41	-0.02	0	65	66
10	-0.365	0	42	66	42	0.245	0	81	66
11	-0.41	0.36	39	90	43	-0.23	-0.075	51	61
12	-0.545	0.015	30	67	44	-0.125	-0.21	58	52
13	-0.59	0.315	27	87	45	0.035	-0.24	67	50
14	-0.485	0.6	34	106	46	0.185	-0.15	77	56
15	-0.755	0.15	16	76	47	-0.065	-0.36	62	42
16	-0.71	0.51	19	100	48	0.185	-0.315	77	45
17	-0.08	0.525	61	101	49	0.335	-0.12	87	58
18	0.215	0.63	79	108	50	0.5	-0.195	98	53
19	-0.245	0.615	50	107	51	0.26	-0.465	82	35
20	0.02	0.765	66	117	52	0.44	-0.495	94	33
21	0.38	0.795	90	119	53	0.65	-0.405	108	39
22	-0.23	0.855	51	123	54	0.5	-0.72	98	18
23	0.185	0.93	77	128	55	0.845	-0.225	121	51
24	-0.455	0.84	36	122	56	0.71	-0.63	112	24
25	0.185	0.15	77	76	57	0.515	0.18	99	78
26	0.035	0.24	67	82	58	0.65	-0.09	108	60
27	-0.125	0.21	58	80	59	0.56	0.345	102	89
28	-0.23	0.075	51	71	60	0.755	0.12	115	74
29	0.335	0.12	87	74	61	0.515	0.57	99	104
30	0.185	0.315	77	87	62	0.8	0.375	118	91
31	-0.065	0.36	62	90	63	0.74	0.6	114	106
32	0.275	0.465	83	97	64	0.95	-0.015	128	65

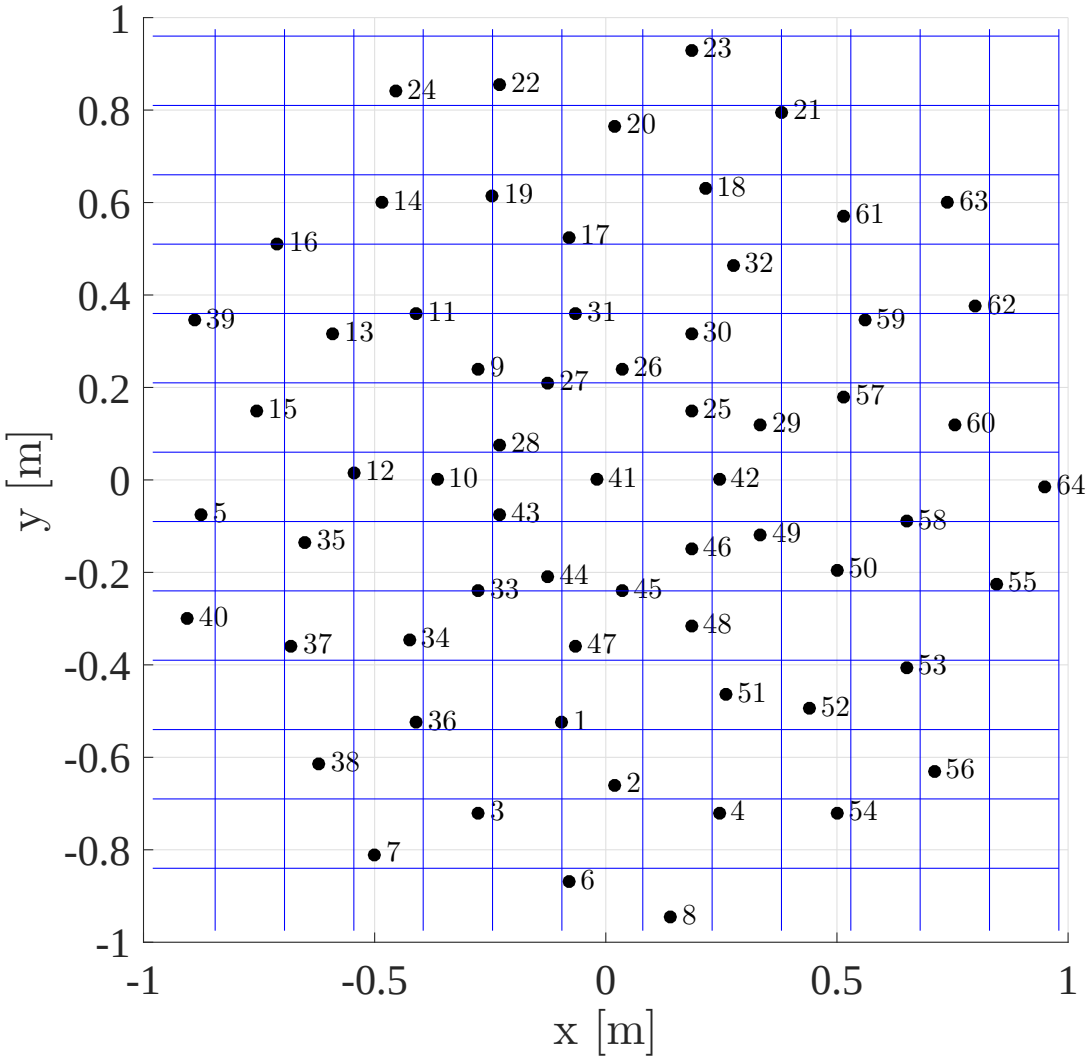

Figure A.3: Optimized array when installed in the V-tunnel with the corresponding microphone numbers